Time-resolved infrared spectroscopy of non-equilibrium dynamics in protein complexes and mid-infrared quantum dots

Dissertation
zur Erlangung des Doktorgrades
an der Fakultät für Mathematik, Informatik und Naturwissenschaften
Fachbereich Physik
der Universität Hamburg

vorgelegt von
Matthias Nikolaus Ruppert
geboren am 8.April 1990
in Reutlingen

Hamburg
2022

Abstract

In this thesis, infrared spectroscopy was used to address non-equilibrium processes in semiconductor nanostructures and proteins on femto- to nanosecond timescales. Special attention was paid to the couplings between low frequency excitations and other (low-frequency) degrees of freedom. Despite the apparent differences in between the investigated material systems, low frequency modes determine the functionality in both, semiconductor nanostructures and proteins. A good example to illustrate this are enzymes, which act as bio-catalysts. Here, conformational changes of the protein lead to a reduction of the activation barrier of bio-chemical reactions, thus enhancing their yield and turn-over rate at room temperature [1]. While the coupling of low frequency excitations and modes that lead to conformational changes is essential for the functionality of these proteins, the coupling between electronic excitations and vibrational lattice excitations leads to rapid carrier thermalization and thereby limits the efficiency of conventional photo-voltaic devices based on semiconductors and semiconductor nanoparticles [2].

As a bulk solid, mercury telluride (HgTe) exhibits a negative band-gap [3]. This allows to tune the band-gap of HgTe nanoparticles across the entire infrared range by varying the localization energy through the particle size [4, 5], which makes them a very promising substitute for epitaxially grown alloys for infrared devices and applications. The coupling between electronic excitations, vibrational excitations of the crystal lattice and the passivating dodecane thiol ligands and their role in carrier relaxation have been of special interest for the experiments presented here. First, energy dissipation from the electronic system upon photo-excitation was investigated. Special attention was paid to the dependency of carrier cooling on the energy of the absorbed photons, which have been varied from the band-gap up to the work function of the HgTE particles. In addition, structure, dynamics and the coupling between states near the band-gap were investigated using two-dimensional infrared spectroscopy. Carrier relaxation to the band-gap was found to be completed within several picoseconds, even for excitation close to the work function. The mean energy dissipation during this process appeared to be largely independent from the initial energy of the hot exciton and the density of states. This suggested that intraband relaxation of electrons is mostly mediated by Auger coupling to holes, while holes relax through coupling to phonon and ligand excitations.

Opposed to directly probing low frequency electronic excitations in HgTe quantum dots, the unnatural amino acid p-azido phenylalanine (AzF) was used as a spectroscopic handle to studying low frequency dynamics in proteins. Here, the azido stretching vibration in AzF was used as a vibrational label with a distinct position in the protein, which allowed correlation of the spectral response of the azido stretching vibration and its immediate surroundings. This way, the local protein structure and its dynamics can be observed through temporal changes in the interaction between the vibrational label and its direct vicinity [6]. It had been previously shown that the spectral signature of the label AzF also reflects conformational changes of the protein [7, 8]. The aim of studying AzF incorporated into the protein Calmodulin (CaM) was to obtain better understanding of the interactions between the azido group and its local environment within the protein. To

this end, the nonlinear vibrational relaxation and the induced absorption feature of the azido group were investigated as a function of protein conformation. These measurements indicated that the Fermi resonance within the azido stretching vibration in AzF mainly contributes towards the distinct spectral signatures in different protein conformations.

Zusammenfassung

Diese Arbeit befasst sich mit Nicht-Gleichgewichtsprozessen in Halbleiternanostrukturen und Proteinen auf der Femto- bis Nanosekunden Zeitskala, die mittels Infrarotspektroskopie untersucht wurden. Dabei standen besonders die niederfrequenten Anregungen und deren Kopplung zu anderen (niederfrequenten) Freiheitsgraden im Fokus. Auch wenn die untersuchten Materialsysteme auf den ersten Blick sehr verschieden sind, wird die Funktion beider entscheidend durch niederfrequente Moden beeinflusst. Beispielsweise können enzymatische Proteine die Aktivierungsenergie biochemischer Reaktionen durch gezielte Konformationsänderungen absenken, so dass diese auch bei Raumtemperatur effizient ablaufen können [1]. Während diese niederfrequenten Moden in Form von Konformationsänderung essentiell für die Funktionsweise von Proteinen sind, so stellt die schnelle Energiedissipation von elektronischen Anregungen durch die Kopplung an Gitterschwingungen eine entscheidende Hürde für die Entwicklung von effizienteren Solarzellen auf Basis von Halbleitern und Halbleiternanopartikeln dar [2].

Das Volumenmaterial Quecksilbertellurid (HgTe) hat eine negative Bandlücke [3]. Deshalb kann durch Variation der Lokalisierungsenergie die Bandlücke von HgTe Nanopartikeln durch den gesamten infraroten Spektralbereich gestimmt werden [4, 5]. Sie stellen damit einen möglichen Ersatz für epitaktische Materialien für infrarot Anwendungen dar. Der Fokus der hier durchgeführten Untersuchungen an den nanoskopischen kolloidalen HgTe Quantenpunkten lag dabei auf der Kopplung zwischen elektronischen Anregungen und Schwingungsanregungen des Kristallgitters und der stabilisierenden Dodecanthiol Liganden. Dazu wurde zunächst die Energiedissipation aus dem elektronischen System nach Photoanregung untersucht. Das Spektrum der zur Anregung genutzten Photonenenergien reichte dabei von der Bandlücke bis hin zur Austrittsarbeit von HgTe. Zusätzlich wurde die Struktur, Kopplung und Dynamik der Zustände nahe der energetisch niedrigsten Anregung mittels zweidimensionaler Infrarotspektroskopie vermessen. Es zeigte sich, dass die Relaxation von Ladungsträgern an die Bandlücke selbst für Anregungen nahe der Austrittsarbeit innerhalb weniger Pikosekunden abgeschlossen ist. Die mittlere Kühlrate ist dabei unabhängig von der Ausgangsenergie des Exzitons und der Zustandsdichte. Dies deutet darauf hin, dass die intraband Relaxation der Elektronen wesentlich durch sehr effiziente Auger Kopplung an Löcher beeinflusst wird, während Löcher durch Kopplung an Liganden- und Phononanregungen relaxieren.

Anstelle der direkten Abtastung der niederfrequenten elektronischen Freiheitsgrade in HgTe Quantenpunkten, wurde die Aminosäure p-Azidophenylalanin als spektroskopischer Zugang zur Untersuchung der niederfrequenten Dynamiken in Proteinen genutzt. Die Azido-Streckschwingung von AzF diente dabei als lokalisierbare Schwingungssonde, die eine eindeutige räumliche und spektrale Zuordnung der Azidostreckschwingung ermöglichte. Durch die zeitliche Veränderung der Wechselwirkung zwischen Schwingungssonde und ihrer unmittelbaren Umgebung, kann so die lokale Struktur und deren Dynamik des Proteins beobachtet werden [6]. So wurde bereits gezeigt, dass sich auf diese Weise Änderungen der Proteinkonformation in der spektralen Signatur dieser Sonde wiederspiegeln [7, 8]. Das Ziel der Experimente des mit AzF präparierten Proteins Calmodulin

(CaM) war ein besseres Verständnis der Wechselwirkung zwischen der Azidogruppe und ihrer unmittelbaren Umgebung. Dazu wurd die nichtlineare Schwingungsrelaxation, sowie die induzierte Absorption der Azidogruppe in Abhängigkeit des Konformationszustands des Proteins untersucht. Diese Messungen ließen vermuten, dass sich die Änderung der spektralen Signatur von AzF in verschiedenen Proteinkonformationen wesentlich auf die Fermiresonanz der Azidogruppe zurückführen lässt.

List of publications and author contributions

- **Intraband dynamics of mid-infrared HgTe quantum dots**
  Matthias Ruppert, Hanh Bui, Laxmi Kishore Sagar, Pieter Geiregat, Zeger Hens, Gabriel Bester and Nils Huse *Nanoscale*, 2022, 14, 4123-4130
  The author performed the pump-probe experiments, data analysis, interpretation and visualization and wrote the manuscript.

- **Population dynamics of stretching excitations of aqueous and incorporated p-azido-phenylalanine in Calmodulin-Peptide complexes**
  Matthias Ruppert, Anne Creon, Henning Tidow and Nils Huse
  J. Phys. Chem. B, 2022, 126, 368-375
  MR and AC contributed equally. The author performed the pump-probe experiments, data analysis, interpretation and visualization and contributed to the manuscript.

Contents

1 Introduction

The macroscopic properties and functionality of each material and molecule are defined by its elemental excitations, which underlie its atomic structure. This spatial arrangement can be described by the attractive potentials between the individual atoms. Infrared spectroscopy provides an excellent handle to probe sub-eV excitations and to access these nuclear potentials through their respective Eigenstates, the electronic and vibrational excitations of the system. Due to its sensitivity to changes in frequency and population of these Eigenstates, interactions in materials and molecules can be unraveled by time-resolved infrared spectroscopy. Local electric fields, structure (e.g. isomerization) and chemical environment as well as energy redistribution between modes can be obtained. In this thesis, two material systems in which the coupling between vibrational and energetically higher excitations are decisive for their functionality are investigated using femtosecond pump-probe and two-dimensional infrared spectroscopy.

The first part of this thesis investigates the coupling between electronic and low frequency excitations in semiconducting mid-infrared quantum dots, which has significant impact on carrier thermalization in these systems. As the ability to influence intraband relaxation enables the development of next generation materials and devices understanding the underlying coupling mechanisms is of tremendous technological relevance. For example, the efficiency of silicon based photovoltaics is restrained by the well known Shockley-Queisser limit [2]. The dilemma being that photons in the solar spectrum with energy below the silicon band gap are not absorbed and therefore inaccessible for energy conversion thus favoring low band-gap materials. On the other hand, photons with energies larger than the band-gap of the device lose this additional energy as heat due to rapid carrier thermalization, favoring large gap materials. Consequently, a trade-off between the two loss-mechanism needs be made, which results in a theoretical maximum efficiency of around 30% for silicon solar cells [2]. A possible approach to more efficient next generation solar cells is the exploitation of mechanisms that effectively suppress carrier cooling, thus enabling the extraction of hot carriers [9, 10, 11] thus harnessing a larger fraction of the solar spectrum. Another technological application where intraband relaxation has direct impact on the efficiency of the device are solid state lasers. Here, the opposite limit for carrier relaxation is desired. Rapid depopulation of the pumped state and the lower level of the lasing transition increases the population inversion and hence the gain of the laser.

Intraband relaxation in bulk solids is governed by the coupling between electronic excitations and vibrational modes and could be characterized as stochastic thermalization processes. Upon (photo-) excitation electrons rapidly form a hot equilibrium through

inelastic electron-electron scattering on a sub 100 femtosecond time scale. The electronic system then dissipates energy through much slower electron-phonon scattering processes, typically over the course of several picoseconds. Here, the low-frequency vibrational excitations act as a bath [12]. This coupling between electronic and vibrational degrees of freedom is depicted in figure 1.1. From this cartoon it can also be deducted, why electrons couple predominantly to optical phonons and acoustic phonons are mainly populated through subsequent phonon-phonon scattering until the system is fully thermalized. Through this, even phonon-phonon interactions may have an effect on carrier relaxation in solids, like in Halide Perovskite nanocrystals. Here, a bottleneck in phonon-phonon scattering is known to slow down carrier cooling [11]. In order to obtain the carrier re-
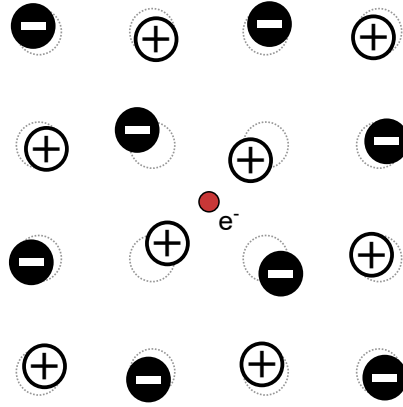

Figure 1.1: Lattice distortions as induced by an additional electron or charge defect in materials with ion cores of opposite charge or polar semiconductors. Coulomb interaction leads to an attractive or repulsive force between electron and positive and negative ion cores, respectively. This reorganization of the lattice can be described in terms of (optical) phonons and therefore illustrates the coupling between electronic degrees of freedom and phonons, the vibrational modes of the crystal lattice. This coupling also leads to new Eigenstates of the system which comprise electronic and vibrational excitations, so called polarons.

laxation characteristics that are desired for novel devices, the suitable choice of materials with advantageous parameters such as phonon energies and electron-phonon scattering efficiency, the Fröhlich coupling constant, provide a good basis. Yet, more control over the interaction between vibrational and electronic excitations becomes accessible through nanostructuring materials. Considering an initial electronic state, $\psi_i(\vec{k})$, with momentum $\vec{k}$ and energy E_i that is scattered into another electronic state, $\psi_f(\vec{k} - \vec{q})$, with momentum $\vec{k} - \vec{q}$ and energy E_f, while emitting an phonon, $\phi_{\text{phonon}}(\vec{q})$, with momentum $\vec{q}$.

$$\psi_i(\vec{k}) \longleftrightarrow \psi_f(\vec{k} - \vec{q}) + \phi_{\text{phonon}}(\vec{q}) \tag{1.1}$$

$$E_i = E_f + \hbar\omega(\vec{q}) \tag{1.2}$$

Here, $\omega(\vec{q})$ denotes the frequency of the phonon. An effective way to reduce the likelihood such electron-phonon scattering events is to reduce the amount of final states $\psi_f(\vec{k} - \vec{q})$ that fulfill energy and momentum conservation for phonon scattering processes. (equations 1.1

and 1.2). This can be achieved through nanostructuring the material, by reducing the size of a material down to the order of its Bohr radius in one or several dimensions. The resulting quantization leads to a discrete level structure along the quantized directions, effectively reducing the density of states (DOS) compared to bulk materials, where the periodic structure leads to a quasi continuous spectrum for both, electronic and vibrational states as indicated in figure 1.2.

Common approaches for the production of such low dimensional materials include the
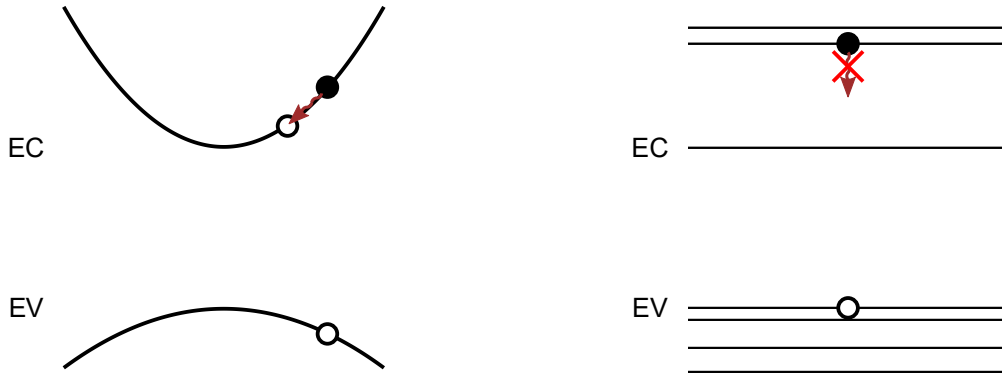

Figure 1.2: Phonon-assisted electron (solid dot) cooling in a band-like level structure (left) and a discrete level structure (right). EC and EV denote the energies of the conduction and valence band, respectively. In the continuous density of states (DOS), phonons (red arrow) can effectively couple states within the same band and allow for rapid thermalization, while phonon assisted cooling is inhibited for a discrete DOS with energy spacings much larger than the phonon energy. The hole is depicted as an empty dot.

growth of interfacial layers or self-assembled quantum dots using molecular beam epitaxy and lithographic techniques which offer excellent control but are hard to scale and therefore expensive. This work focuses on intraband relaxation in colloidal semiconductor quantum dots instead, which are promising due to the relative simplicity, cost-efficiency and potential scale-ability of their production. In short, crystalites are grown from a supersaturated precursor solution, where the particle size can be determined through growth time, which is controlled by temperature [13]. Afterwards, ligands can be added for surface passivation. The quantization along all directions leads to a fully discrete level structure for the electronic states, where the band-gap and intra band level spacings increase with decreasing particle size is decreased [14].

However, the electronic density of states is not the only physical property that is altered in point-like particles like colloidal quantum dots, which makes these systems also very interesting from a fundamental perspective. Firstly, the large surface to volume ratio also enhances the influence of surface effects and ligands. The close vicinity due to localization and the wavepacket nature of carriers leads to exciton formation and greatly enhances the likelihood of Auger processes [15]. The resulting consequences for intraband relaxation are very apparent in the well studied CdSe quantum dot system. Here, phonon-mediated

intraband relaxation is in fact several orders of magnitude slower [16, 17] than the rates typically found in bulk materials [12], as had been predicted for materials with energy gaps on the order of ten LO phonon energies [18, 19]. Yet, the timescales found for intraband relaxation of electrons found in these systems still occurs on time-scales as fast as 100 femtoseconds [20, 21]. Obviously, (multi-) phonon-mediated processes cannot be the dominant decay channel for electron cooling in these systems. Instead, Auger scattering between electrons and holes was found to allow for rapid electron thermalization through energy transfer from the conduction band to the valence band [22, 23]. In order to obtain a system featuring slow intraband relaxation, not only phonon mediated processes, but also this Auger channel needs to be suppressed. This can be done by either using n-doped particles, removing the hole [17], or spatially separating electrons and holes thus eliminating spatial overlap. This can be achieved by using type II hetero-structured core-shell quantum dots [16], as illustrated in figure 1.2.

In addition to Auger coupling, the wavepacket nature of the carriers affects intraband

Figure 1.3: Illustration of heterostructures in core shell quantum dots. $CB_{core/shell}$ and $VB_{core/shell}$ denote the energetically lowest state in the conduction band and the energetically highest state in the valence band of the bulk material of the core, or shell, respectively. These structures can be regarded as a regular colloidal quantum dot, the core, which is surrounded by an additional semiconductor layer with different energies for highest occupied state and the lowest unoccupied state. The resulting box-like potential can be used to localize charge carriers in the core, or shell to enhance or reduce surface effects and even spatially separate electrons and holes. In type I heterostructures both, the electron and hole wavefunctions are localized in the core, while the holes are localized in the shell in type II configuration. Exemplary material combinations for type I are CdSe (core) CdS (shell) and CdSe (core) CdTe (shell) for type II [24].

relaxation by enabling non-adiabatic coupling to phonons and / or ligands [25, 26]. However, the mechanisms which underlie intraband cooling are not universal for all quantum dot systems. In contrast to CdSe, where effective Auger coupling between electrons and holes dominate intraband relaxation, electrons and holes seem to relax largely independent in PbSe quantum dots [27, 28]. Consequently, the relevant mechanisms need to be characterized for each quantum dot system in order to allow for control over carrier cooling.

In this work, carrier relaxation in colloidal mercury telluride (HgTe) nanoparticles is in-

vestigated. These particles are of special interest as they can span the entire infrared range [4, 5] by varying the particle size, thus being a potential more readily available replacement for conventional infrared alloys, which need to be produced through molecular beam epitaxy. Despite rapid progresses in the development on devices based on HgTe quantum dots [29, 30, 31, 32], only the time-scales for carrier recombination are reported in the literature [33, 34]. First, the much faster intraband dynamics in HgTe MIR quantum dots are investigated in different excitation regimes using two color, optical/infrared pump infrared probe spectroscopy. Additionally, the band-edge dynamics in these particles are studied using 2D infrared spectroscopy. This method allows to ignore the spectral inhomogeneity in size distribution which is intrinsic to the growth method of colloidal quantum dots as described above. This paves the way towards access of fine structure and couplings between states even in an inhomogenous quantum dot ensemble on femtosecond timescales as opposed to single dot spectroscopy using high numerical aperture lenses, which usually does not allow for ultrafast pump-probe experiments due to low photon counts.

The second part of this thesis addresses the low frequency modes of unnatural aminoacids when incorporated into proteins and their interplay with conformational changes of the latter. In contrast to nanoparticles, where the coupling between high energy electronic excitations to vibrational modes accounts for an undesired stochastic loss of energy for photovoltaic applications, a proteins function can often be attributed to the coupling between coordinated collective motions and energetically higher states. This coupling works in both directions, from high to low energy, like conformational change following an electronic excitation upon absorption of a visible photon of the retinal protein rhodopsin [35], which enables human eyesight. The other direction of energy redistribution from low to high frequency excitations can be observed in enzymatic reactions [1].
Each protein consists of a subset 20 unique amino acids which are linked together into a polypeptide chain, also called the primary structure. In aqueous solution this peptide chain folds into $\alpha-$helices and $\beta-$ sheets the so-called secondary structure and uniquely defines three dimensional arrangement of the protein, the tertiary structure. This means, that already this sequence of amino-acids contains the complete information on the functionality of a protein. Recent breakthroughs even allow the estimation of tertiary structures from primary structures with reasonable accuracy using artificial intelligence [36]. Still, the functionality of proteins in the sense of macromolecular machines is usually tied to non-equilibrium processes [37, 38], which can only be obtained from time-resolved experiments so far. Performing such experiments is not only challenging due to the fragile nature of proteins compared to other samples, i.e. solids or smaller molecules and typically scarce amounts of sample, but also due to the requirements regarding the experiment itself. Spatially resolved dynamics need to be captured on sub-picosecond timescales, ideally in aqueous solution phase, which is the natural environment of proteins. X-ray crystallography has been extensively used to study protein structures but requires crystallization of the protein, which is not possible for all proteins. Additionally, the proteins tertiary structure and its dynamics may be inhibited or altered in crystalline form. Nuclear magnetic resonance spectroscopy (NMR) on the other hand can provide structural information in

solution, but is not fast enough to capture solvent fluctuations or quick backbone motions. Another very powerful method is Multidimensional infrared spectroscopy, which can provide the required time-scales and can also be used on proteins in aqueous solution. However, it cannot provide structural information, as the assignment of vibrational bands is completely ambiguous in proteins [39], a consequence of the identical 20 building blocks and the reoccurring peptide bond. To overcome this problem, an amino acid at a position of interest within a protein, such as an active site, can be exchanged by an unnatural amino acid (UAA) featuring a distinct vibrational mode outside the vibrational bands of the protein and solvent used. This way, the introduced vibrational mode then acts as an observer of the local electric field, protein structure or solvent exposure [40, 41]. There are several factors that need to be considered for the choice of a suitable UAA. Of course, it needs to perturb the protein structure as little as possible from its native form. At the same time, a strong dipole transition moment is desired to allow for non-linear experiments at concentrations in the few mMol range. Additional requirements are a long vibrational lifetime in order to observe slow protein motions and a line-shape that can be easily understood.

In this thesis, the protein Calmodulin (CaM), a Ca^{2+} sensitive second messenger protein, labeled with p-azidophenylaline (AzF) was used as a model system for mid-infrared pump-probe spectroscopy. AzF has a comparatively large dipole moment, facilitating spectroscopic measurements. AzF incorporated into CaM had also previously been demonstrated to be able to distinguish different protein conformations through FTIR spectroscopy [7], which motivates these experiments further. As a downside, a Fermi resonance within the azido group complicates the linear spectrum [42] and is expected to drastically decrease the lifetime of the vibrational excitation of the azido stretching vibration.

Here, the goal is to explore the capabilities of AzF as a vibrational label beyond the linear response of the azido stretching vibration in different protein conformations. This is further motivated by potential insight into dynamics of the molecular couplings involved in the Fermi resonance, thus gaining more insight into the composition of the linear spectrum and how it reacts to conformational changes.
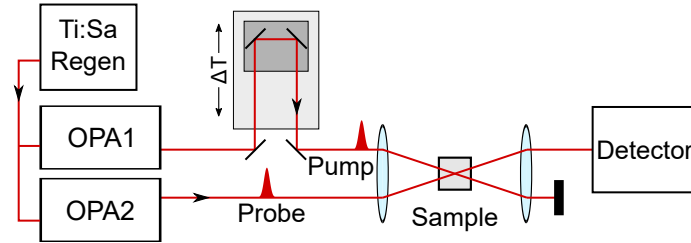
2 Multidimensional infrared spectroscopy

Figure 2.1: Schematic view of an infrared pump probe experiment. A Ti:Sa regenerative amplifier (Ti:Sa regen) drives two optical parametric amplifiers (OPAs), for the generation of pump and probe, respectively. This allows to use different frequencies for excitation and probing of the sample. The time delay between pump and probe, ΔT, is controlled by a mirror pair mounted on a motorized translation stage in the beam path of the pump pulse. Pump and probe are then overlapped in the sample. The transmitted probe pulse is sent onto a detector, often a combination of an imaging monochromator and a liquid nitrogen cooled detector array.

The response time of photo sensors limits the temporal resolution of real time detection to several hundreds of picoseconds. In order to observe dynamics on shorter time-scales, so-called pump probe experiments are necessary. Here, the sample is first excited by a an optical excitation pulse, called the pump. After a well defined time-delay, the absorption spectrum is captured by another optical pulse, the so-called probe, this is schematically shown in figure 2.1. The full dynamics are then unraveled by scanning through the time-interval between excitation and detection pulse. In in such a scheme, the temporal resolution is no longer governed by the detector read-out time, but the duration of the pump- and probe-pulses, enabling access to dynamics on the order of tens of femtoseconds using commercially available Ti:Sa laser sources, which are the bread and butter of non-linear optical spectroscopy. Such regenerative amplifier laser-systems are based on chirped pulse amplification (CPA) [43], which was awarded the physics Nobel prize in 2018. CPA allows for femtosecond pulses with pulse energies in the millijoule range, sufficient to efficiently drive parametric amplification. Which, in turn, allows for a virtually gap free spectral tunability of femtosecond pulses covering the visible [44] to mid-infrared [45] spectral range, using only a single laser source. This thesis employs this technology to study ultra-fast dynamics in the mid-infrared spectral range, the principles and theory of which is explained in the following section.

2.1 Theoretical description

The theoretical foundation of ultrafast spectroscopy is the perturbative expansion of the density matrix, which is well described in the textbook by Shaul Mukamel [46]. This section gives a brief summary of this approach.

First, the macroscopic polarization, $P(t)$, is described using the density matrix, $\hat{\rho}(t)$, and the dipole operator, $\hat{V}$,

$$P(t) = \langle \hat{\rho}(t) \cdot \hat{V} \rangle. \tag{2.1}$$

Here, $\langle ... \rangle := \sum_n \langle n | ... | n \rangle$, denotes the trace for any basis set of the Hilbert space of the system $\{|n\rangle\}$. This way, the temporal evolution of the polarization can be described in terms of the Liouville equation [46]:

$$\partial_t \rho = -\frac{i}{\hbar} \left[\hat{H}, \hat{\rho} \right] \tag{2.2}$$

$$\equiv -\frac{i}{\hbar} \hat{\mathcal{L}} \hat{\rho}. \tag{2.3}$$

$\hat{H}$ denotes the Hamiltonian, $\hat{\mathcal{L}}$ is the Liouville (super-) operator, which acts on operators $\hat{O}$ defined on the Hilbert space of the system. It is defined as $\hat{\mathcal{L}} := [\hat{H}, \hat{O}]$. The light matter interaction is treated in dipole approximation as a time dependent perturbation:

$$\hat{H} = \hat{H}_0 - E(t) \cdot \hat{V} \tag{2.4}$$

Here, $\hat{H}$ denotes the Hamiltonian, $\hat{H}_0$ the unperturbed Hamiltonian, $E(t)$ is the electric field and $\hat{V}$ is the dipole operator. This splitting of time-dependent and time-independent contributions allows the use of the interaction picture and a series expansion of the density matrix in orders of the electric field. After a lengthy derivation, the polarization can be expressed as:

$$P(t) = \langle \hat{V} \hat{\rho}(-\infty) \rangle + \sum_{n=1}^{\infty} P^{(n)}(t) \tag{2.5}$$

$$P^{(n)}(t) = \left(\frac{i}{\hbar} \right)^n \cdot \int_0^\infty dt_n ... \int_0^\infty dt_1 \, E(t - t_n) ... E(t - t_n - ... - t_1) \cdot R^{(n)}(t_n, ..., t_1) \tag{2.6}$$

$$R^{(n)}(t_n, ..., t_1) = \langle \hat{V} \hat{\mathcal{G}}(t_n) \hat{\mathcal{V}} \hat{\mathcal{G}}(t_{n-1}) \hat{\mathcal{V}} ... \hat{\mathcal{G}}(t_1) \hat{\mathcal{V}} \rho(-\infty) \rangle \tag{2.7}$$

Here, $\hat{\mathcal{V}}$ is the Liouville dipole operator. It is defined as $\mathcal{V} \hat{O} := [\hat{V}, \hat{O}]$, for operators defined on the Hilbert space of the system, $\hat{O}$. $R^{(n)}(t_n, ..., t_1)$ is the nth order non-linear response function and $\hat{\mathcal{G}}(t)$ denotes the Liouville (forward) time-propagator:

$$\hat{\mathcal{G}}(t) = \Theta(t) \cdot \exp[-\frac{i}{\hbar} \hat{\mathcal{L}}_0(t))]. \tag{2.8}$$

$\hat{\mathcal{L}}_0\hat{O} := [\hat{H}_0, \hat{O}]$ is the Liouville operator of the unperturbed system, $\Theta(t)$ is the Heaviside step function.

In equation 2.5 The zero-order term, $\langle V\hat{\rho}(-\infty)\rangle$, denotes the static polarization of the sample, the first order term describes linear propagation and absorption. As the second order term vanishes in centro symmetric materials, the third order term, $P^{(3)}(t)$, usually gives rise to the largest contribution in non-linear spectroscopies:

$$P^{(3)}(t) = \left(\frac{i}{\hbar}\right)^3 \cdot \int_0^\infty \mathrm{d}t_3 \int_0^\infty \mathrm{d}t_2 \int_0^\infty \mathrm{d}t_1\, E(t-t_3) \cdot E(t-t_3-t_2) \cdot E(t-t_3-t_2-t_1) \times$$
$$\times \mathrm{R}^{(3)}(t_3, t_2, t_1) \tag{2.9}$$

$$\mathrm{R}^{(3)}(t_3, t_2, t_1) = \langle \hat{V}\hat{\mathcal{G}}(t_3)\hat{\mathcal{V}}\hat{\mathcal{G}}(t_2)\hat{\mathcal{V}}\hat{\mathcal{G}}(t_1)\hat{\mathcal{V}}\rho(-\infty)\rangle \tag{2.10}$$

The integrals can be understood as the superposition of the response function for all possible combinations of the interaction times, t_i, weighted with their respective field strength. The third-order response function, $\mathrm{R}^{(3)}(t_3, t_2, t_1)$, can be understood in the following way: Starting from the right-hand side, the system is first in the unperturbed state, $\hat{\rho}(-\infty)$. The first light interaction creates a dipole excitation, via the Liouville dipole operator $\hat{\mathcal{V}}$. The time propagator $\hat{\mathcal{G}}(t_1)$ then evolves the system for the time-interval t_1, the time between the first two light interactions, when the second dipole excitation occurs, the system is then again propagated by $\hat{\mathcal{G}}(t_2)$ and so forth. At last, a photon is emitted via the the Hilbert space dipole operator, $\hat{V}$, which is then observed by the detector.

2.1.1 Double sided Feynman diagrams

Figure 2.2: Pulse sequence used for the discussion of the third order non-linear response function. τ_1 (τ_2) is the time interval between pulse 1 and 2 (2 and 3).

The general expression for the third order non-linear polarization (equation 2.1) can often be simplified, by making several reasonable approximations. First, a pulse sequence of three pulses as shown in figure 2.2 is examined. Only the case for non-overlapping pulses is considered, allowing a clear ordering of the interactions connected to the individual pulses. For time-delays where pulses do overlap ($\tau_i = 0$), this approximation breaks

down, leading to additional contributions in the response function. This is the so-called coherent artifact, which cannot be easily interpreted. It is also assumed that each pulse interacts exactly once, a scenario which can be enforced by considering photon momentum in the experimental design.

For laser pulses that are a lot shorter than the dynamics in the sample, the pulse envelopes can be approximated as delta distribution, thus trivializing the integrals. This is also called the semi-impulsive limit. Equation 2.1 then simplifies to:

$$P^{(3)}(t) = \left(\frac{i}{\hbar}\right)^3 \cdot \langle \hat{V}\hat{\mathcal{G}}(t)\hat{\mathcal{V}}\hat{\mathcal{G}}(\tau_2)\hat{\mathcal{V}}\hat{\mathcal{G}}(\tau_1)\hat{\mathcal{V}}\rho(-\infty)\rangle \tag{2.11}$$

Also taking into account that the electric field irradiated by this polarization is interfering with the probe-pulse, also referred to as self heterodyned detection, it can be shown that the spectrally resolved absorption change, $\Delta A(\omega)$, in the sample is proportional to the Fourier transform of third-order response function [47]:

$$\Delta A(\omega) \propto (-1) \cdot \mathcal{FT}\left\{\langle \hat{V}\hat{\mathcal{G}}(t)\hat{\mathcal{V}}\hat{\mathcal{G}}(\tau_2)\hat{\mathcal{V}}\hat{\mathcal{G}}(\tau_1)\hat{\mathcal{V}}\rho(-\infty)\rangle\right\} \tag{2.12}$$

Herein, an expression for the measured quantity, $\Delta A(\omega)$, depending on the experimental parameters τ_1 and τ_2 is found. While this expression is much simpler than equation 2.1, the commutator, which is hidden in the Liouville dipole operator, $\hat{\mathcal{V}}$ makes the evaluation tedious. Conveniently, these nested commutators can be decomposed using graphic representations of different quantum pathways for elements of the dipole matrix, so-called double sided Feynman diagrams. Exemplary, the response function for the Feynman diagram shown in figure 2.3 is constructed.

In these diagrams, time runs from bottom to top. Initially, the system is in the ground
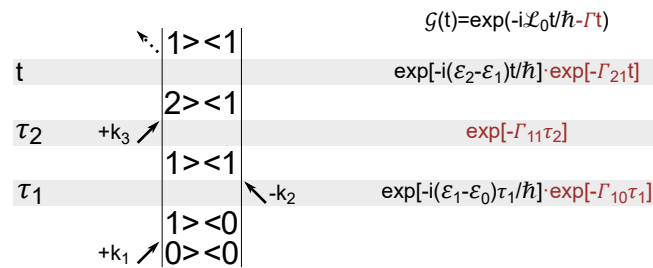

Figure 2.3: Construction of the third order response function using double sided Feynman diagrams. Time intervals, in which the time propagator $\hat{\mathcal{G}}(t_i)$ has to be evaluated are highlighted in gray. The eigenvalues of the time propagator are displayed on the right hand side. The contributions marked as red only appear after dephasing has been introduced.

state, $|0\rangle\langle 0|$. Following equation 2.12, the interaction with the first pulse immediately creates a coherence $|1\rangle\langle 0|$, indicated by an arrow. The system is then propagated for τ_1, creating a phase of $\exp[-\frac{i}{\hbar}(\epsilon_1 - \epsilon_0)\tau_1]$ according to equation 2.8. Now, the second dipole interaction excites the system into the population state $|1\rangle\langle 1|$ this state is propagated for τ_2, which in this picture does not evolve in time. Finally, the interaction with the third pulse creates the coherence $|2\rangle\langle 1|$. The last propagator creates the phase $\exp[-\frac{i}{\hbar}(\epsilon_2-\epsilon_1)t]$.

There are several 'rules' for the evaluation of double sided Feynman diagrams:

- As a result of the commutator in $\hat{\mathcal{V}}$, the overall sign of the response function is $(-1)^n$, where n is the number of dipole interactions on the right hand side of the diagram.

- For all non-zero contributions to the response function, the last state always has to be a population state due to the trace in equation 2.12.

- For resonant conditions, an arrow pointing towards the diagram corresponds to absorption, pointing away from it stands for emission of a photon. This is called the rotating wave approximation.

- Arrows pointing to the right (left) carry the momentum $+\vec{k}_{1,2,3}$ $(-\vec{k}_{1,2,3})$ of the respective electric field. The momentum of the emitted field, $\vec{k}_s$, is $\vec{k}_s = \pm\vec{k}_1\pm\vec{k}_2\pm\vec{k}_3$ with the signs corresponding to the diagram. This property can be used to isolate specific quantum paths: In configurations, where pump and probe are not parallel, only diagrams where the pump wave-vectors have opposite signs will contribute to the detected response and the emitted third order polarization co-propagates the probe pulse, which is then heterodyning the signal.

To construct the entire response of a system, all possible quantum pathways have to be taken into account and added. Figure 2.4 shows all contributing Feynman diagrams for a two-level system within the rotating wave approximation. Also shown are the more intuitive level-scheme representations for the isolated pathways.
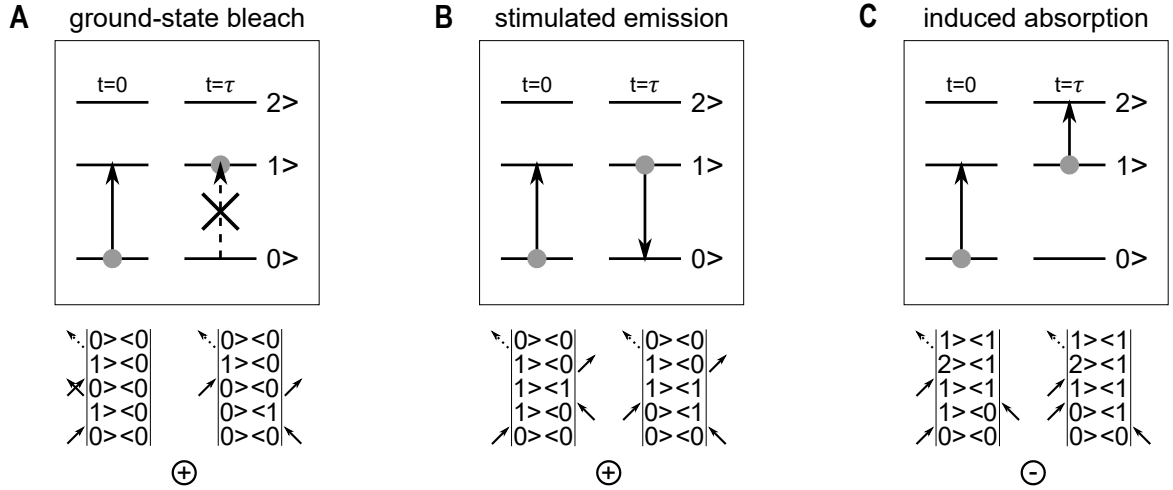
Figure 2.4: Feynman diagrams in the rotating wave approximation and level schemes for a two level system. **A**: Ground-state bleach. The depletion of ground state population creates a negative transient absorption feature. **B**: Stimulated emission is often spectrally indistinguishable from ground state bleach, but is a distinct process. **C**: The population of state $|1\rangle$ allows for absorption at the $|1\rangle$ to $|2\rangle$ transition, which does not absorb in the ground state, thus creating a net positive absorption feature at $\omega = \frac{\epsilon_2 - \epsilon_1}{\hbar}$. This is referred to as induced absorption.

Dephasing

So far, the time propagator introduced in equation 2.8 only creates a phase term for coherent superpositions and consequently, neither coherences nor population states decay. Which, in turn, causes infinitely long transient signals and infinitely sharp absorption lines. To obtain more reasonable results, dephasing can be added in an ad hoc fashion by using a damped time propagator, $\hat{\mathcal{G}}_{damped}(t)$:

$$\hat{\mathcal{G}}_{damped}(t) = \Theta(t) \cdot \exp\left[-\frac{i}{\hbar}\hat{\mathcal{L}}_0(t) - \Gamma(t)\right]. \tag{2.13}$$

The response function for the diagram shown in figure 2.3 then reads:

$$\begin{aligned} R^{(3)}(t) = (-1) \cdot |\mu_{10}|^2|\mu_{21}|^2 &\times \exp\left[-i/\hbar \cdot (\epsilon_1 - \epsilon_0) \cdot \tau_1 - \Gamma_{|1\rangle\langle0|} \cdot \tau_1\right] \\ &\times \exp\left[-\Gamma_{|1\rangle\langle1|} \cdot \tau_2\right] \\ &\times \exp\left[-i/\hbar \cdot (\epsilon_2 - \epsilon_1) \cdot t - \Gamma_{|2\rangle\langle1|} \cdot t\right] \end{aligned} \tag{2.14}$$

In a pump-probe experiment, the first two interactions originate from the same pump pulse, $\tau_1 = 0$. According to equation 2.12 this quantum pathway then creates an positive absorbance change with a Lorentzian line-shape, which corresponds to the life-time of the $|2\rangle\langle1|$ coherence. The signal decays with the life-time of the $|1\rangle\langle1|$ population state, which often allows the interpretation of pump-probe signatures as population dynamics.

$$\Delta A(\omega, \tau_2) \propto (-1) \cdot |\mu_{10}|^2|\mu_{21}|^2 \frac{\Gamma_{|2\rangle\langle1|}}{(\omega - \omega_{|2\rangle\langle1|})^2 + \Gamma_{|2\rangle\langle1|}^2} \cdot e^{-\frac{\tau_2}{\Gamma_{|1\rangle\langle1|}}} \tag{2.15}$$

It should be noted, that the simplistic treatment of dephasing does not conserve population, i.e. $\langle\hat{\rho}\rangle \neq 1$. This especially manifests in the ground state bleach diagrams, where a decay of the signal has to be introduced by force, as the ground state cannot be repopulated. More realistic simulation strategies for the time propagator $\hat{\mathcal{G}}(t)$ can be found in the textbook by Peter Hamm and Martin Zanni [47].

2.2 2-dimensional optical spectroscopy

In pump-probe spectroscopy, only a single pump pulse is used which, in turn, interacts twice with the sample. This means, all phase information during the time between the first and second field interaction, τ_1, is lost in the third order non-linear response (equation 2.12). In 2-dimensional optical spectroscopy, this quantity is explored using the more sophisticated pulse pattern shown in figure 2.2. Inspired by NMR pulse sequences, 2d spectroscopy was first demonstrated on the Amide I band in peptides [48] in the near-infrared. Since then, the field evolved rapidly. Concepts to allow phase- stability for optical frequencies in the visible [49, 50] and advanced pulse sequences have been established [51, 52]. Even advances towards 3-dimensional spectroscopy, a 5th order technique
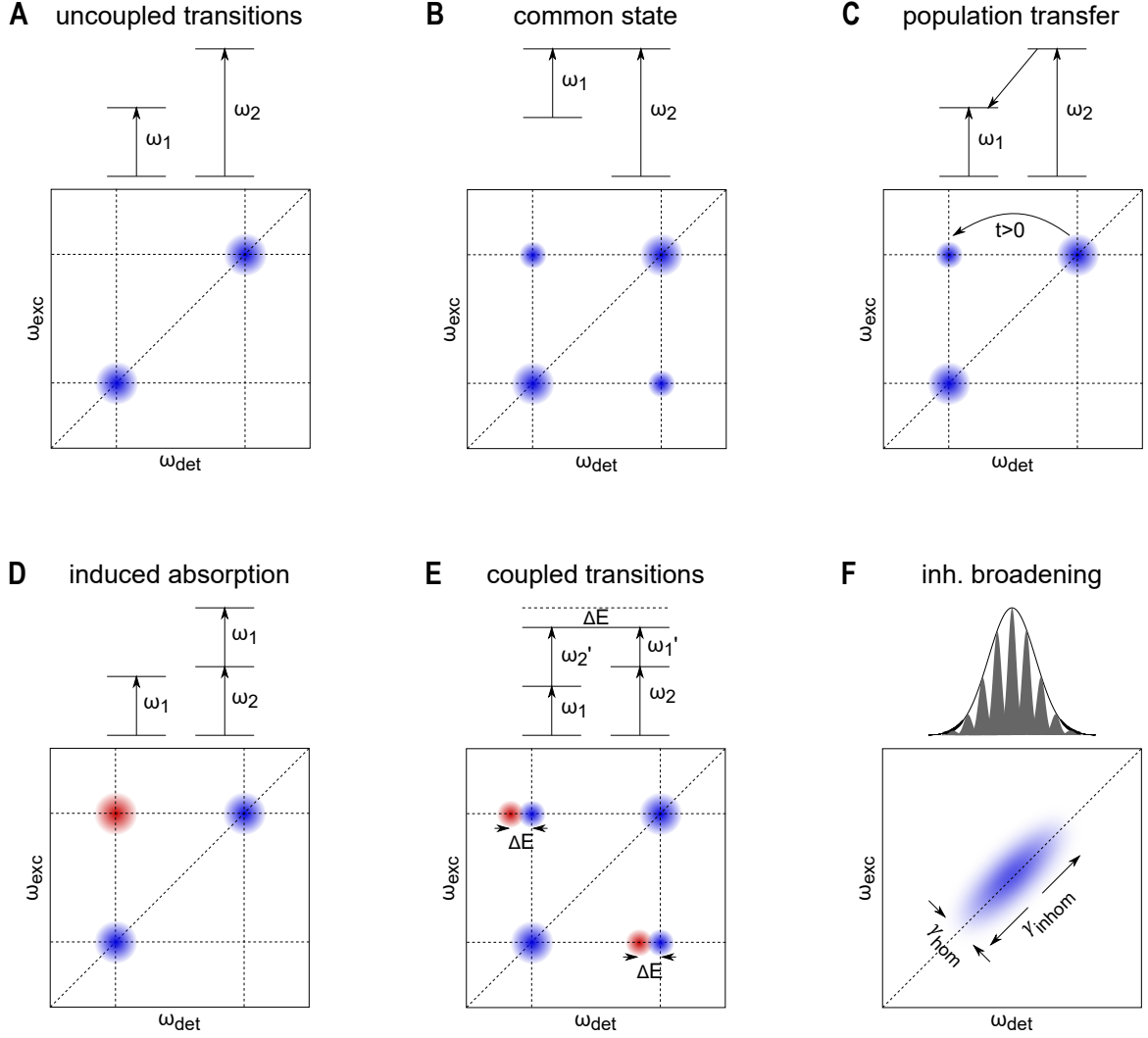
Figure 2.5: 2d correlation maps for the illustration of different phenomena in optical 2d spectroscopy. Horizontal and vertical dashed lines correspond to ω_1 and ω_2, respectively. Blue depicts negative transient absorption, red denotes an increase in absorption.

correlating 3 frequencies at different times, have been made [53, 54].

The underlying principle of 2 dimensional spectroscopy is best explored using Feynman diagrams. The response for the Feynman diagram shown in figure 2.3 has already been presented in equation 2.14. By performing a Fourier transform along τ_1, a second frequency axis added, corresponding to the excitation frequency ω_{exc}. According to equation 2.12, the transient absorption connected to this quantum pathway then reads:

$$\Delta A(\omega_{exc}, \omega_{det}, \tau_2) \propto -\frac{\Gamma_{|1\rangle\langle 0|}}{(\omega_{exc} - \omega_{|1\rangle\langle 0|})^2 + \Gamma_{|1\rangle\langle 0|}^2} \cdot \frac{\Gamma_{|2\rangle\langle 1|}}{(\omega_{det} - \omega_{|2\rangle\langle 1|})^2 + \Gamma_{|2\rangle\langle 1|}^2} \cdot e^{-\frac{\tau_2}{\Gamma_{|1\rangle\langle 1|}}} \quad (2.16)$$

This spectral representation of the optical response allows to directly correlate the excitation frequency and the absorption frequency ω_{det}, which is experimentally resolved using a spectrometer. The delay between pulse 2 and 3, τ_2, is called the population-, or

waiting-time.

The additional frequency axis, where the frequency resolution is governed by the natural linewidth of the system, allows to follow the response of specific transitions, as if they were selectively excited using a narrow-band pump pulse. Thus, 2d spectroscopy can achieve high spectral selectivity, without compromising temporal resolution by using narrow-band pulses, as is the case with pump probe spectroscopy. This makes 2d spectroscopy exceptionally useful for samples exhibiting large inhomogeneous broadening [55], interconverting species [56] or rapidly fluctuating (solvent) environments [57].

To illustrate how different effects manifest in 2d-spectroscopy, several exemplary correlation maps are displayed in figure 2.5. Usually none of the effects shown appear solitarily and different overlapping contributions may complicate the interpretation of 2d spectra. **A**: In the absence of induced absorption, uncoupled transitions result in an entirely diagonal 2d correlation map (excitation frequency, ω_{exc}, = detection frequency, ω_{det}). These diagonal negative absorption features are caused by ground-state bleach (GSB) and stimulated emission (SE). In the panels B-E, only the effects additional to the diagonal GSB and SE features are discussed. **B**: If electronic transitions share a state, off-diagonal bleach features are observed. In the case of a shared upper level, this is caused by state filling of the upper level (only for Fermions) and stimulated emission. For shared lower levels, this results from ground state bleach due to de-population of the lower level. **C**: Decay channels, where population from the upper level gets de-populated into another state, the diagonal peak will shift to the transition frequency of the relaxed state, as waiting time increases. **D**: Induced absorption features appear as positive, off-diagonal absorption features. In contrast to regular pump-probe spectroscopy, they can also be observed, if they overlap with the ground state absorption of another transition, as shown in this example. **E**: Coupled transitions, where the excitation of one transition alters the frequency of another transition, as is the case with excitonic excitations in semiconductor quantum dots [58], cause these characteristic off-diagonal features. As the frequency of the second transition gets shifted, the absorbance at its initial frequency will decrease, while a new absorbing feature will arise at the new frequency. Here, $\Delta E = E_1 + E_2 - E_{1,2}$ denotes the energy difference between individually exciting states 1 and 2 and simultaneously exciting them. **F**: 2d spectroscopy is a powerful tool to study inhomogeneous broadening. As the bleach signal of each system is located on the diagonal, the line-shape along the diagonal represents the inhomogeneous distribution. The cut perpendicular to it allows to access to homogeneous linewidth , thus being able to resolve spectral features that would be inaccessible by pump probe spectroscopy [59]. It should be noted, that if the inhomogeneity of the sample is not static, as for solvent effects in molecules, the depicted line-shape is only valid for a vanishing waiting time, τ_2, [60]. Line-shape theory for inhomogeneously broadened systems at non-zero waiting time can be found in the textbook by Peter Hamm and Martin Zanni [47].
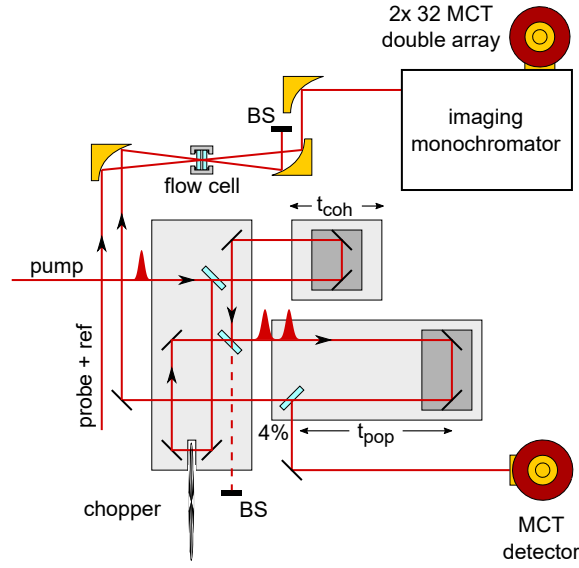
Figure 2.6: Simplified layout of the experimental setup. Abbreviations used: BS - beam stop, MCT - mercury cadmium telluride, ref - reference beam, t_{coh} - coherence time, t_{pop} - population time.

2.3 Experimental setup

The setup is conceptually the same as a regular pump-probe setup with an additional Mach-Zehnder interferometer with one movable arm in the pump beam. This allows the creation of a pulse pair with variable delay, *tcoh*, at the cost of 50 % of the intensity. The layout of the 2d setup is shown in figure 2.6. It is based on the pump-probe geometry design originally published by Helbing and Hamm [61]. A commercial Ti:Sa regenerative amplifier[1] provides $150 \, \mu J$ pulses to two home-built optical parametric amplifiers [45]. These provide close to transform limited pulses tunable from $1.2 \, \mu m$ to $10.0 \, \mu m$ with a spectral width[2] of $300 \, cm^{-1}$ and pulse energies larger than $1.5 \, \mu J$ by either directly using signal or idler, or the difference frequency of the latter. The reflexes from both surfaces of a BaF_2 wedge are used as probe and reference beam. This reference beam co-propagates the probe beam at a vertical offset and its spectrum is recorded on a separate pixel array behind the monochromator. This allows the use of normalized spectra that are independent from shot-to-shot intensity fluctuations for data processing. The pump pulse is split into a pulse pair using the output of one arm of a Mach-Zehnder interferometer, consisting of two broadband 50:50 beamsplitters, where a motorized stage controls the coherence time, τ_1. A chopper in the other arm of the interferometer allows the subtraction the interference term between the two pump pulses from the correlation map. Note, that in contrast to regular pump probe spectroscopy neither the ground state absorption, nor signal contributions where both of the first two dipole interactions arise from a single pulse need subtraction using a chopper. In fact, all static contributions will be removed by the Fourier transform along τ_1, which acts as a spectral filter removing all terms which

---

[1]Spectra Physics Spitfire Ace: $90 \, fs$, $3 \, kHz$, $1.4 \, mJ$, $800 \pm 5 \, nm$

[2]Full width at half maximum

are constant with respect to τ_1. The pulse pair is then sent onto another delay line that controls the population time, τ_2. The reflex from a CaF$_2$ wedge is sent to a MCT detector to track the interferometric auto correlation of the pump pair. This deviates from Helbing's design [61], where the coherence time is binned using a co-propagating HeNe laser in the Mach-Zehnder interferometer. This is also an improvement over the use of a pyroelectric detector in the unused arm of the Mach-Zehnder interferometer, as suggested by Helbing [61], as this approach picks up a phase shift due to slight deviations in the used beam-splitters, making data analysis more complicated. The majority is then sent into a telescope consisting of off-axis parabolic mirrors focusing pump and probe into a single spot within the liquid sample cell. The transmitted pump is then blocked, while the probe is focused into the entrance slit of an imaging monochromator. In addition to the IR pulse pair, the sample can be pumped using the 800 nm pulses and its second and third harmonic, not shown in figure 2.6, which also allows for transient 2d experiments.

3 Semiconductor Nano-crystals

3.1 Introduction

Colloidal semiconductor nano-crystals (NCs), or more generally, semiconductor quantum-dots (QDs) are structures that are on the order of or smaller than the Bohr radius of the respective material in all dimensions. An effective synthesis route for stable colloidal clusters was first achieved for CdSe and other Cadmium compound ligand-capped colloidal NCs via liquid phase crystal growth [62]. The relative simplicity of this approach and its prospect of industrial scale production drove the further development of NCs for applications like solar energy beyond the Shockley-Queisser limit [63, 64], bio-imaging [65, 66] and lasing [67, 68]. State of the art NC solar cell concepts are based on beating the Shockley-Queisser limit [2] by minimizing heat losses by either extracting hot carriers [10, 11], or creating multiple electron hole pairs upon single photon absorption [69, 70]. The spatial confinement in three dimensions leads to a particle in a box like potential for electrons and holes in colloidal quantum dots. This manifests in discrete level structure for both, valence and conduction band. Additionally, the energy of the lowest excitation increases compared to the bulk material. Moreover, the close vicinity of the confined electron and hole states leads to increased Coulomb interaction. This leads to the formation of hydrogen-like bound electron hole states, so-called excitons. For spherical particles with radius, R, the resulting energy increment for the band-gap state, ΔE_{gap} can be estimated as [14]:

$$\Delta E_{gap} \approx \frac{\hbar^2 \pi^2}{2R^2} \cdot \left(\frac{1}{m_e} + \frac{1}{m_h} \right) - \frac{\alpha e^2}{R}. \tag{3.1}$$

The first term denotes the kinetic contribution, also called localization energy, scaling as R^{-2}. m_e and m_h denote the effective masses of electron and hole, respectively. The second term denotes the attractive Coulomb interaction between electron and hole. It depends on the materials dielectric properties, which are summarized as a material parameter α here. This term is also called the exciton binding energy. According to equation 3.1, the band-gap and by that, absorption and luminescence wavelength can be controlled via the macroscopic particle radius. By this, the distribution of particle sizes is leads to inhomogeneous line-broadening. Another important effect in quantum dots is the formation of multi-excitons, which can form a bound state leading to an reduction in

energy compared to two individual excitons due to correlation effects and screening [58, 71]

$$E_{XX} = 2 \cdot E_X - \Delta E_{XX} \qquad (3.2)$$

Here, E_{XX} denotes the bi-exciton energy, E_X the energy of a single exciton and ΔE_{XX} is the bi-exciton binding energy.

Figure 3.1 A illustrates to level structure in zero dimensional semiconductors using the known results for particles in a infinite box potential of length L. This approximation neglects the effects of multiple nearly degenerate valence bands commonly found near the band-gap as also shown in Figure 3.1 B. These additional valence bands lead to additional quantized states in the valence band, especially the degeneracy of light and heavy hole band will be lifted by the effective mass contribution in the localization energy. The resulting higher density of states in the conduction band of QDs will become important later, when dynamics are discussed. It should be noted, that the schematic band structure shown in figure 3.1 B is derived assuming only rotation symmetry of the material [72] and is often an oversimplification, as for several materials including HgTe, the material system studied in this thesis, the ordering of bands is inverted, leading to a negative bulk band-gap of -0.3 eV [3].

3.2 Carrier dynamics

Intra-band relaxation

Auger processes are inelastic electron-electron scattering processes and are well known from x-ray photo-emission. Here, one electron-hole pair recombines, transferring its energy and momentum to a second electron, or hole. In bulk semiconductors, this process is generally very inefficient due to momentum conservation, resulting in Auger recombination times in the micro- to nanosecond regime [74, 75].

With Auger processes playing only a minor role in semiconductors, phonon emission was initially assumed to be the dominant relaxation pathway for excited electrons in semiconductor nanoparticles. Phonon-assisted carrier relaxation had been predicted to be less efficient in low dimensional structures in general [18] and being slowed down even further by inefficient high-order multi-phonon processes required to bridge the gaps in the discrete electron level structures [19]. This led to the assumption of strongly increased lifetimes for intraband relaxation, the so-called phonon bottleneck. Experimental results showing sub-picosecond relaxation rates for an energy gap larger than 14 LO phonons in the conduction band of CdSe nanoparticles [20], then challenged this prediction, suggesting dominant relaxation channels other than phonon emission. Colloidal quantum dots often extend for less than 10 unit cells per dimension, resulting in a lack of translational invariance. The resulting relaxed momentum conservation and the enhanced Coulomb interaction due to the close vicinity of confined electrons and holes suggested that the ef-
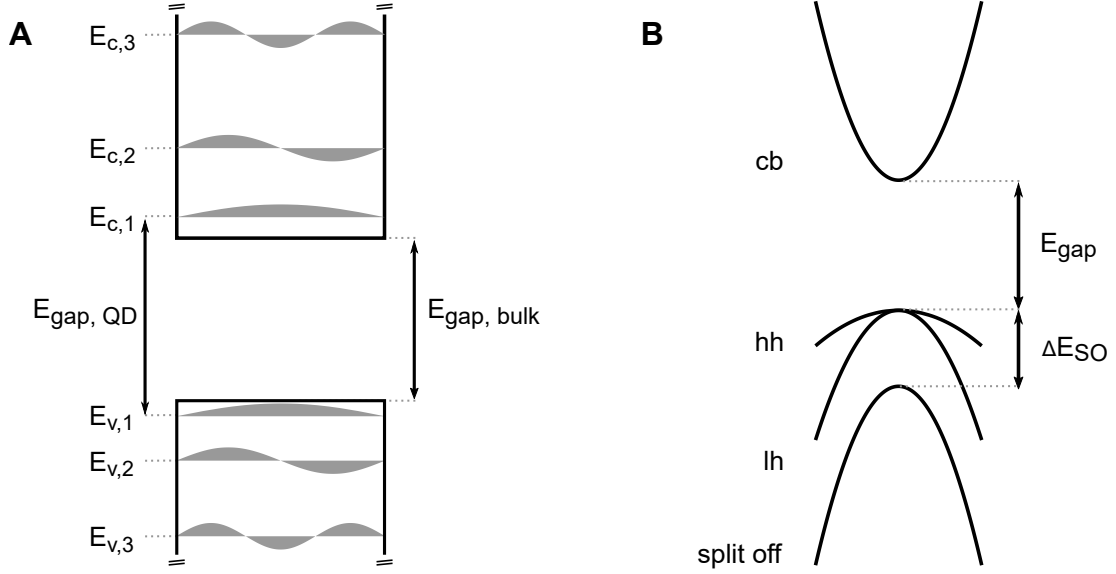
Figure 3.1: A: Wave functions for electrons and holes for infinitely steep confinement considering only a single band conduction band (c) and a single valence band (v). The energy levels are $E_{i,n} = n^2 \cdot \frac{\pi^2 \hbar^2}{L^2 \cdot m_i^*}$, with the effective mass m_i^* of the respective band. As the effective mass of holes is higher than the effective mass of electrons in most materials [72], the level spacing in the valence band is usually tighter than the level spacing in the conduction band in colloidal quantum dots. If a more realistic band-structure including spin-orbit coupling as depicted in B is considered, each band will result in a set of confined states as shown above, leading to a much more complicated level structure. Additionally, the degeneracy between light and heavy holes will be lifted by the confinement. While this description is instructive, it completely neglects the exciton binding energy introduced in equation 3.1. By this, the ordering of states may change for different particle sizes in the same material system [73], making theoretical predictions compulsory for the assignment of (optical) transitions.

B: Simplified band structure of a bulk semiconductor. *cb* denotes the conduction band, *lh* and *hh* are the light and heavy hole band, respectively. *split off* denotes is the split-off band separated by the spin orbit coupling energy ΔE_{SO}. Considering spin-orbit coupling, neither spin $\vec{S}$, nor angular momentum $\vec{L}$ are good quantum numbers, only the combined angular momentum $\vec{J} = \vec{S} + \vec{L}$ is conserved. The split off band carries a combined angular momentum $|J| = \frac{1}{2}$ with possible projections $m_j = \pm \frac{1}{2}$. It is thus split by the spin orbit coupling energy, ΔE_{SO}, from the light and heavy hole band which carry a angular momentum of $|J| = \pm \frac{3}{2}$ ($m_j = \pm \frac{1}{2}$ for light holes, $m_j = \pm \frac{3}{2}$ for heavy holes) [72]. The projections, m_j can be useful to determine optically active transitions via selection rules, as photons carry an angular momentum of 1, allowing only for transitions with $\Delta m_j \in [-1, 1]$, depending on the polarization. These selection rules can also be applied to excitonic states using their total angular momentum as quantum number.
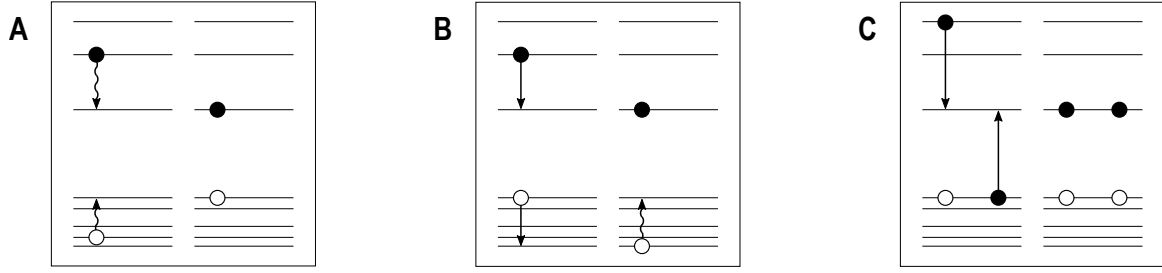
Figure 3.2: Intraband relaxation pathways for excitons in quantum dots. Phonon assisted relaxation is depicted as wave arrows, relaxation via Coulomb interaction as straight arrows. **A:** Phonon assisted relaxation. Typically, this process is much faster for holes compared to electrons, due to a much higher density of states in the valence band. **B:** Auger cooling (electron) and heating (hole). The electron transfers energy to the hole, which then rapidly decays to the band-gap. **C:** Multiexciton generation. A highly excited exciton relaxes to the band gap, transferring its energy to an electron in the valence band, creating another exciton. Due to energy conservation, this effect can only occur if the initial exciton has an energy of at least twice the band-gap.

ficiency Auger-processes may be strongly enhanced in quantum dots. This was supported by subsequent investigations in CdSe NCs, where faster transition rates were observed with decreasing particle size [21]. These experimentally observed Auger-rates were then confirmed by calculations later [76], showing intraband Auger lifetimes as short as only 100 fs, several orders of magnitude faster than in bulk semiconductors. The importance of Auger processes in nanocrystals is further emphasized as they were also found to govern the recombination times for multi particle excitations [76, 77, 78] as depicted in figure 3.3. It should be noted, that shorter lifetimes with decreasing particle size are not universally tied to Auger processes. In a more complex wavepacket model for phonons an increasing electron energy loss rate due phonon emission was also found for decreasing radii [25]. However, this is much less efficient than Auger processes [25]. In fact, great efforts, such as the spatial separation of electron and hole wave functions [16] need to be made to suppress Auger processes, in order to observe other intraband relaxation channels. The role of ligands in intraband relaxation is still under debate, there is experimental evidence for energy transfer from the electronic system into ligand modes [79, 80] but the exact mechanism is still under debate [81, 26].

Figure 3.2 shows fundamental intraband cooling processes. A shows the individual phonon or ligand assisted cooling of electron and hole. As discussed above, this process is very inefficient for electrons. For holes however, this effect is more efficient, due to the decreased separation of energy levels in the valence band. B shows the Auger cooling of the electron, transferring its energy to the hole, which then relaxes to the band gap via energy dissipation through phonons or ligands. This appears to be the dominant relaxation channel for electron in CdSe nanoparticles [20, 76, 23]. C shows the so-called multi exciton generation (MEG). Here, a highly excited electron relaxes to the band-gap state, while transferring its excess energy to an electron in the valence band, promoting it to the conduction band. This effect happens on sub 100 fs timescales and was first observed upon non-resonant photo-excitation of PbSe Qds [69] and described theoretically soon

after [82]. Of course, this effect has to comply energy conservation, meaning the photon has to carry at least twice the band-gap energy. However, an MEG is usually only observed experimentally for photon energies at least three times the band gap. This means, it is inherent to any quantum dot system, with the exception that the band gap might exceed a third of the materials work function in some cases. It is thus most accessible for particles with a band-gap in the infrared, and also was observed using photo-current measurements in HgTe quantum dots[34].

This effect has drawn a lot of attention, as the photon energy beyond the gap is not lost in heat, as in conventional silicon solar cells, but is converted into additional harnessable electron hole pairs. Thus allowing for the construction of solar cells beyond the Shockley Queisser limit [2]. The quantum yield for this process and its energy onset is usually discussed as a matter of competing energy relaxation channels and their respective probability [83, 84, 85] leading to concepts of increasing the MEG quantum yield by exploiting a bottleneck in phonon cooling in perovskite nanocrystals [70].

Interband relaxation

The band-edge dynamics in colloidal QDs are well understood and can be described by a multi-exponential model, each time constant representing a distinct multi-exciton species [77]. In this model, multi-excitons recombine via Auger scattering. This recombination happens on much faster time-scales than the recombination time of a single exciton, which is on the order of, or slower than, several hundred of picoseconds. It was also shown, that the multiparticle lifetime should decrease with each additional electron hole pair that is excited [78]. Exemplary interband dynamics for HgTe quantum dots at different fluences and a schematic view of the recombination processes are shown in figure 3.3. In the low fluence regime (black curve), the dynamics are well described by a single exponential with a time constant larger than 500 ps for the systems studied here. This single-exciton lifetime is governed by direct recombination via photon emission, depicted in **B** and the coupling to (surface-) trap states. With increasing fluence, multi-photon absorption processes become more likely. This manifests in the formation of multi-excitons. For multi-excitons, not only direct recombination but also Auger processes have to be taken into account. These processes are schematically shown in **C**. Here, one electron hole pair recombines, transferring its energy and momentum to the remaining hole, which then relaxes back to the band gap via phonon emission, effectively reducing the bi-exciton to a single exciton, which then undergoes direct recombination (**B**). Due to the relaxed momentum conservation and high density of states in the valence band, these processes occur with timescales of tens of picoseconds and thus are the dominant recombination channel for multi-excitons as opposed to radiative recombination of electron hole pairs.
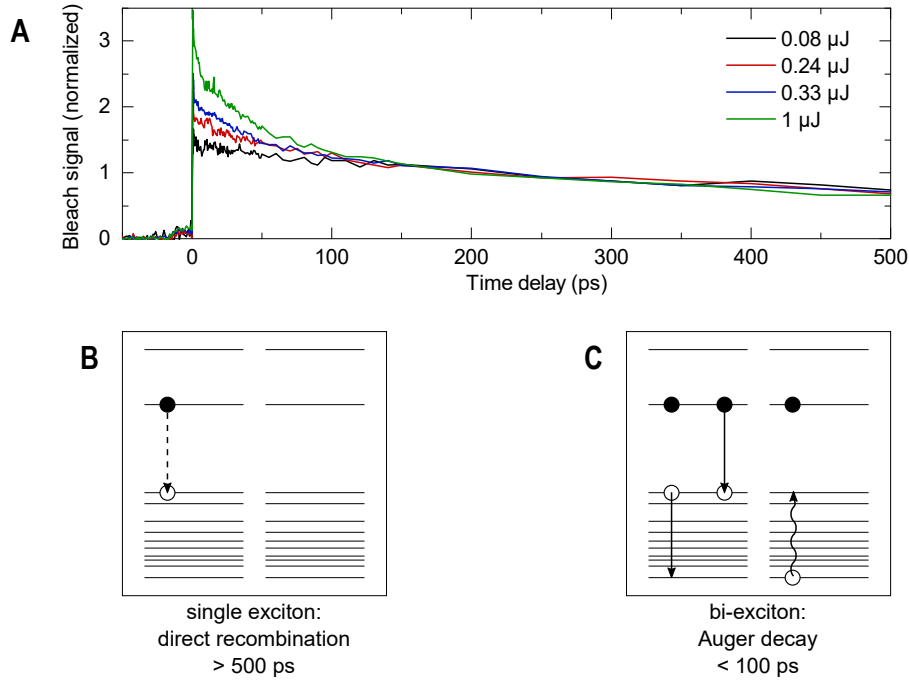
Figure 3.3: Band-gap (2.5 µm) bleach signal of thiol capped HgTe nanocrystals for different pump pulse energies for resonant excitation (**A**) and dominant decay channels for excitons (**B**) and bi-excitons (**C**). To emphasize the differences in early dynamics, the time traces have been re-normalized to have matching long-lived exponential tails after 150 ps.

3.3 HgTe Quantum dots

For high performance infrared photo-detectors, the band-gap of the alloy must be chosen wisely, as small band-gaps translate to higher thermal occupation translating to larger dark currents. Larger band-gap materials on the other hand, insensitive to longer wavelengths. Most detectors are therefore based on Indium Gallium Arsenide ($In_xGa_{1-x}As$) for short wavelength infrared or Mercury Cadmium Tellurium ($Hg_{1-x}Cd_xTe$) alloys for longer wavelengths, as the band-gap can be tuned by attenuation of the Cadmium, or Gallium fraction, respectively. [86, 87].

However, these alloys need to be grown epitaxially, a method that is difficult to scale and, therefore, very expensive. Colloidal quantum dots, which can be spectrally tuned by controlling their size and the promise of possible large scale production via crystal growth in the liquid phase are therefore suitable candidates for next generation infrared materials [88]. As they do not restrict the spectrum towards long wavelengths, especially materials with a negative bulk band-gap, such as HgTe [3], are of great interest for this application. Following equation (3.1), the spectral frontier towards the far infrared is only limited by the largest particle size that can be reliably synthesized in such materials. First thiol-capped HgTe nanoparticles exhibited absorption and fluorescence in the near infrared [89]. During the last decade, advanced synthesis methods continuously extended the accessible spectral range [90, 4], spanning the entire infrared range with particles more than a 100 nm in diameter featuring band-gaps as low as 5 THz [5]. Simultaneously, prototypes

for MIR photo-sensors based on HgTe QDs were developed [91]. Using HgTe QD based detectors, benchmarks comparable to commercially available conventional photo-sensors were reported for the near and mid infrared spectral region [92, 31], showing the potential of these devices. Still, improvements in sensitivity [93, 29], response time [94], read-out time [95], stability at ambient conditions [96] and field of view [97] are constantly made. Apart from applications in photo-sensors, HgTe particles exhibit a surprisingly low lasing threshold for mid-gap transitions [98] and multi-exciton generation for excitation in the visible range was observed [34], suggesting possible applications in novel solar cells.

Driven by these technological advances, the fundamental physical properties of HgTe Qds were studied. Likely, the most important are the scaling of particle band gap and fluorescence with diameter [99, 4] and the corresponding level structure [100, 4, 101]. Also, the band-gap dynamics in HgTe particles have been studied extensively. These include exciton and bi-exciton lifetimes [102] as well as their size dependence and the effect of particle aggregation [33] as well as the photo-current response in the MEG regime [34]

3.4 Results: carrier relaxation in HgTe MIR nano-crystals

Aside fundamental scientific interest, intra-band relaxation dynamics in quantum dots are of major technological relevance including the yield of advanced solar cells based on processes like multi-exciton generation [84, 103], hot carrier extraction [11, 104] as well as the de-population of the pumped transition in lasing applications [105, 67]. Despite the technological advances involving HgTe QDs mentioned in section 3.3, all time-resolved studies on MIR HgTe quantum dots have been aimed at multi-exciton dynamics at the band-gap [102, 34, 33], leaving the intra-band relaxation mechanism, which occurs during the first ten picoseconds completely concealed. Here, carrier relaxation in HgTe quantum dots was studied using ultrafast MIR spectroscopy at a temporal resolution of 150 fs in different excitation regimes for both photon energy and excitation density. The results of which are concluded in the following manuscript. These measurements reveal an extremely uniform intraband relaxation behavior, where the dissipation of energy from the electronic system occurs at a rate independent of the initially excited state and number of excited electron hole pairs. As these results precede their computational counterpart, a rigorous interpretation of the underlying mechanism is largely impossible. The timescales provided here lay the foundation to gauge future computational models for the intraband relaxation in HgTe QDs . However, comparison to other quantum dot systems allows for mechanistic insight regarding intraband relaxation in MIR HgTe quantum dots. In brief, the observed ultrafast cooling times contradict coupling to vibrational modes as main relaxation pathway for electrons in the conduction band and suggest Auger cooling instead, which had been introduced in section 3.2, while the uniform hole cooling might be explained by non-adiabatic coupling to ligand modes [26, 106]. In addition these observa-

tions regarding intraband dynamics, sub-picosecond time-scales for carrier multiplication in these particles are found.

Nanoscale

PAPER

Check for updates

Intraband dynamics of mid-infrared HgTe quantum dots†

Matthias Ruppert, [ID] [a] Hanh Bui,‡[b,c] Laxmi Kishore Sagar,§[d,e] Pieter Geiregat,[d,e] Zeger Hens, [ID] [d,e] Gabriel Bester[b,c] and Nils Huse [ID] *[a,c]

Femtosecond pump–probe spectroscopy reveals ultrafast carrier dynamics in mid-infrared (MIR) colloidal HgTe nanoparticles with a bandgap of 2.5 μm. We observe intraband relaxation processes after photo-excitation ranging from resonant excitation up to the multi-exciton generation (MEG) regime by identifying initially excited states from atomic effective pseudopotential calculations. Our study elucidates the earliest dynamics below 10 ps in this technologically relevant material. With increasing photon energy, we find carrier relaxation times as long as 2.1 ps in the MEG regime close to the ionization threshold of the particles. For all photon energies, we extract a constant mean carrier energy dissipation rate of 0.36 eV ps^{-1} from which we infer negligible impact of the density of states on carrier cooling.

Introduction

Intraband cooling is of fundamental interest for technological applications of semiconductors, a process that is most important for light harvesting as well as light-amplification and sensing applications. For instance, slow intraband relaxation may allow the realization of highly efficient solar cells through harnessing of hot carriers[1,2] or the utilization of carrier multiplication.[3–5] The opposite limit is desirable for lasing applications, *i.e.* for optimal pumping efficiencies. Compared to bulk materials, the dominant carrier relaxation channels and relaxation rates are heavily altered in colloidal quantum dots for several reasons. First, a discrete level structure with spacings of several LO phonon energies makes phonon-mediated relaxation processes significantly less efficient.[6] At the same time, the wave packet nature and close vicinity of car-

riers enhance Auger scattering, a good overview of which can be found in a recent review.[7] A larger surface to volume ratio also enhances surface effects and the influence of ligands.[8–11] Yet, the resulting relaxation pathways are by no means universal for all quantum dot systems. This observation becomes very clear when comparing the well described quantum dot systems CdSe and PbSe. In CdSe quantum dots, electrons in the conduction band transfer their energy almost instantaneously (sub 100 fs) to hole states in the valence band. This is known as Auger cooling (of the electron) or Auger heating (of the hole).[12,13] Hole states then relax through phonon and/or ligand mediated processes. In PbSe quantum dots on the other hand, both, electrons and holes, seem to independently relax in a ladder hopping manner through ligand or phonon assisted processes.[14–16]

In contrast to these well described quantum dot systems, the dynamics during the first 10 picoseconds after photo-excitation are largely unknown in MIR HgTe quantum dots, while the slower band edge dynamics are well understood.[17,18] The possibility of tuning their band-gap through the entire infrared down to the Terahertz spectral range by varying the size of the crystallites[19–21] makes these particles very promising for technological applications such as infrared sensing[22–27] and emission.[27–29] MEG has been demonstrated in these particles as well,[18] meaning that a photon of sufficient energy may efficiently excite several electron hole pairs upon being absorbed, as also observed in other quantum dot systems.[3,5,30]

Here, we report the early dynamics in MIR HgTe quantum dots with a band-gap of 2.5 μm using ultrafast visible/infrared pump–probe spectroscopy. We observe the early state filling dynamics of the energetically lowest exciton state upon non-

[a]Institute for Nanostructure and Solid-State Physics, Department of Physics, University of Hamburg and Center for Free-Electron Laser Science, Luruper Chaussee 149, 22761 Hamburg, Germany. E-mail: nils.huse@uni-hamburg.de
[b]Physical Chemistry and Physics departments, University of Hamburg, Luruper Chaussee 149, 22761 Hamburg, Germany
[c]The Hamburg Centre for Ultrafast Imaging, University of Hamburg, Luruper Chaussee, 149, 22761 Hamburg, Germany
[d]Physics and Chemistry of Nanostructures, Department of Chemistry, Ghent University, Krijgslaan 281 - S3, B-9000 Gent, Belgium
[e]Center for Nano and Biophotonics, Ghent University, Technologiepark Zwijnaarde 15, B-9052 Gent, Belgium
†Electronic supplementary information (ESI) available. See DOI: 10.1039/d1nr07007j
‡Current address: Faculty of Fundamental Science, Phenikaa University, Yen Nghia, Ha-Dong District, Hanoi, 10000, Viet Nam.
§Current address: Department of Electrical and Computer Engineering, University of Toronto, 10 King's College Road, Toronto, Ontario M5S 3G4, Canada.

resonant excitation, which allow assigning timescales for intra-band carrier relaxation mechanisms in different excitation regimes. By varying pump wavelengths from 2.4 μm up to 400 nm, we gain insight into the exciton cooling process from the lowest optical excitation up to the highly non-resonant MEG regime, where a single photon may excite up to four electron hole pairs in HgTe quantum dots.[18]

Experimental

Our infrared pump–probe setup consists of two independently tunable optical parametric amplifiers[31] (OPAs) for pump and probe pulses. Additionally, the 800 nm radiation of the Ti : Sa regenerative amplifier (Spitfire Ace, Spectra Physics, 800 nm, 90 fs, 1.7 mJ, 3 kHz) and its second harmonic (400 nm) were used to excite the sample at these wavelengths. For all measurements, the probe at 2.5 μm was generated using the idler of one OPA, which is in resonance with the optical bandgap of the nanoparticles. Depending on the excitation wavelength the idler (2 μm, 2.4 μm) or signal (1.2 μm) of the second OPA were used to excite the sample at infrared wavelengths. The power of all beams was controlled by a combination of polarizers and waveplates. To keep the fluence low, while still achieving reasonable photon counts on the detector, the sample was mounted outside the focal plane, where the spot size is approximately 1 mm in diameter (FWHM). A peristaltic pump (Cole Parmer Masterflex) and a flow-cell (Harrick Scientific, 1 mm thick CaF_2 windows, 2 mm sample thickness) was used to provide fresh sample for each consecutive shot. Spectra were resolved using an imaging monochromator (Triax 180, Horiba) in combination with a nitrogen cooled 2× 32 MCT pixel array (Infrared Associates).

Synthesis

The dodecanethiol-capped particles were synthesized following Keuleyan *et al.*[20] and dispersed in toluene. Additional details can be found in a more recent publication[29] with a deviating temperature of 90° instead of 60° and a growth time of 3 minutes.

Theoretical description

The single-particle Schrödinger equation is solved using the atomistic effective pseudopotential approach[32–34] which allows us to study structures with several thousand atoms, so that we can model experimentally relevant system sizes. The approach is based on density functional theory in the local density approximation (LDA) but includes an empirical correction applied to the non-local part of the pseudopotential,[35] and which corrects the failure of the LDA to obtain accurate quasi-particle bandgap states including the effective masses. In the next step, the excitonic states are obtained using the screened configuration interaction (CI) approach[35,36] where a microscopic screening model has been used in the calculation of the Coulomb and exchange matrix elements. The structure used in

our calculation is spherical with a diameter of 5.25 nm. It includes 1253 Hg atoms and 1328 Te atoms using a so-called aspherical pseudo-hydrogen passivation[33] which accurately represent the case of a fully passivated and defect free surface.

Results and discussion

Fig. 1 (panel A) shows an exemplary time trace of the band edge bleach signal for excitation at 800 nm. The band-edge dynamics show an initial build-up during the first few picoseconds, followed by a fast decay component on the order of several tens of picoseconds and a slower component decaying on the order of 100 s of picoseconds. The long-lived components of HgTe quantum dots are well known and can be attributed to exciton recombination in the 100 s of picoseconds to nanoseconds and Auger decay auf bi-excitons on the order of tens of picoseconds.[17] The signal grows in much more slowly than our temporal resolution of ≲150 fs and can therefore attributed to a delayed arrival of carriers at the bandgap as a consequence of the non-resonant excitation. To obtain a quantitative description of this data, we employ a rate-equation model as depicted in Fig. 1 (panel B, see ESI† for details). Only a single cooling time for the carrier relaxation to the bandgap is considered here, as the bandgap dynamics do not allow for distinction between electron and hole intra-band cooling. The bandgap relaxation is modelled using the commonly employed bi-exponential approach[37,38] to account for the above mentioned Auger decay of multi-excitons. The number of electron hole-pairs at the band-gap, $N_0(t)$, can then be described by:

$$N_0(t) = \frac{1}{2}\left(1 + \mathrm{erf}\left(\frac{2\sqrt{\ln(2)} \cdot t}{\mathrm{IRF}}\right)\right)\left[\frac{N_{i,\mathrm{e}}(0)\tau_\mathrm{e}}{\tau_\mathrm{c} - \tau_\mathrm{e}}\left(e^{-\frac{t}{\tau_\mathrm{c}}} - e^{-\frac{t}{\tau_\mathrm{e}}}\right) + \frac{N_{i,\mathrm{b}}(0)\tau_\mathrm{b}}{\tau_\mathrm{c} - \tau_\mathrm{b}}\left(e^{-\frac{t}{\tau_\mathrm{c}}} - e^{-\frac{t}{\tau_\mathrm{b}}}\right)\right]. \tag{1}$$

Here, $N_{i,\mathrm{e}}(0)$ and $N_{i,\mathrm{b}}(0)$ denote the number of initially excited electron hole pairs in particles with a single exciton only and particles with two excitons, respectively. τ_e, τ_b and τ_c, denote the exciton recombination time, the bi-exciton recombination time and the intraband cooling time. The first term in Eqn (1) accounts for the finite width of the instrument response where erf denotes the Gaussian error function and IRF denotes the full width at half maximum (FWHM) of the instrument response function. All pump and probe pulses are close to transform limited with a pulse duration of 100 fs (FWHM), which results in a signal rise time (10%-to-90%) of ≤150 fs. IRF was therefore fixed to 150 fs so as not to overparameterize the fit.

Eqn (1) was used to simultaneously fit data for different excitation densities and wavelengths. For this global fit, the exciton and bi-exciton lifetime parameters, τ_e and τ_b, were shared across this large data set and only the amplitudes, $N_{i,\mathrm{e}}(0)$ and $N_{i,\mathrm{b}}(0)$, and the intraband cooling time, τ_c, vary between different time traces. An exemplary fitted time trace is
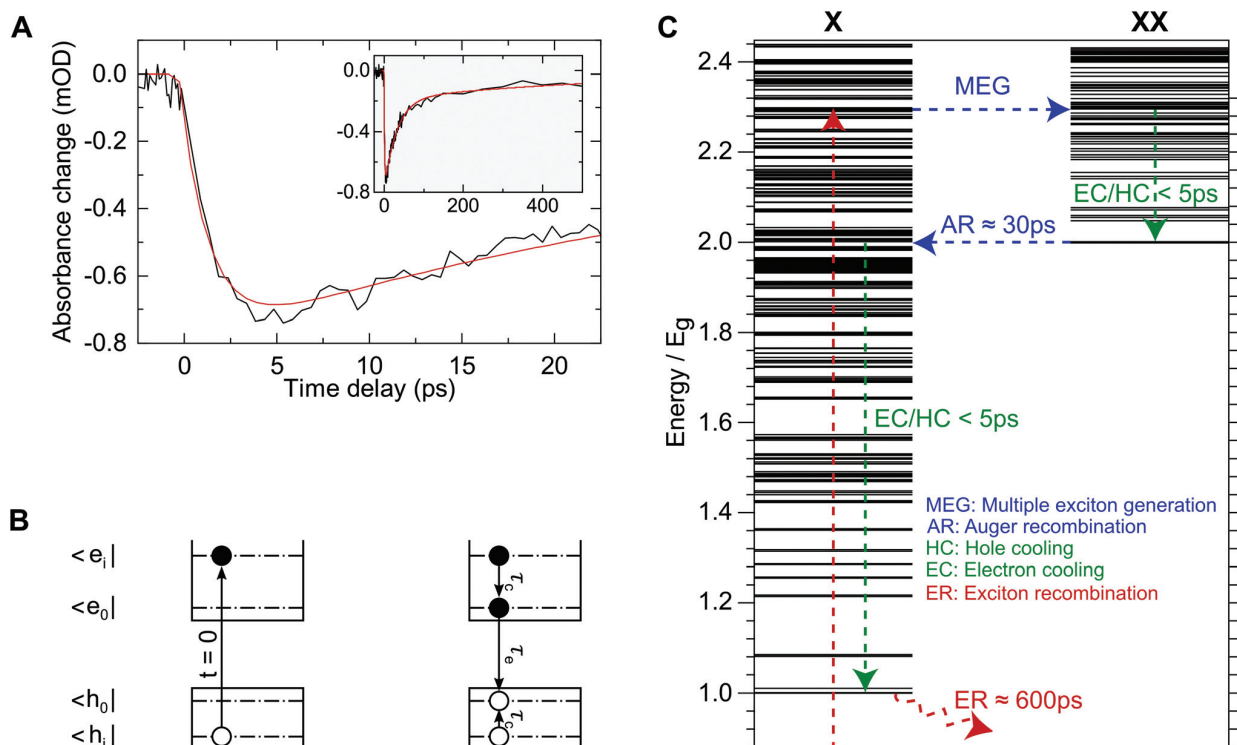
26

Fig. 1 (A) Exemplary band-gap bleach signal at a probe wavelength of 2.5 μm for excitation at 800 nm with 50 nJ pulse energy (black) along with a fit of the two-step model (red) as depicted in (B). Early, sub-10 picosecond dynamics can be mainly attributed to filling of the lowest excitonic state. (B) Illustration of the two-step decay model used for data analysis. At $t = 0$ an electron–hole-pair, $|e_i,h_i\rangle$ is created by laser excitation. This state then relaxes to the optical bandgap $|e_0,h_0\rangle$ with the exciton cooling time, τ_c. The exciton recombination time is denoted by τ_e. This model does not treat electron and hole cooling times individually, as only the population of $|e_0,h_0\rangle$ is accessible using our experimental method. (C) Calculated exciton (X) and bi-exciton (XX) spectra and schematic carrier dynamics in the MEG regime and associated experimentally obtained time-scales. Energy is displayed in units of the band-gap, E_g. After photo-excitation a bi-exciton is created through MEG. This hot bi-exciton then relaxes to the energetically lowest bi-exciton state through intraband cooling, which can be observed as the rising edge in (A). This bi-excitonic state then undergoes inverse Auger-recombination on a 30 picosecond time-scale. The lifetime of the remaining exciton is roughly 600 ps.

also shown in Fig. 1 (panel A, red curve), demonstrating that the data can be adequately modelled using only 3 time-constants covering both, the initial rise and the long-lived interband recombination. We obtain $\tau_E = 623 \pm 150$ ps and $\tau_B = 31 \pm 10$ ps for the exciton recombination and biexciton Auger relaxation times. These lifetimes have already been reported for HgTe NCs with a similar bandgap.[17] Our findings for the bi-exciton lifetime are identical within the margins of error. However, we find 5 times shorter exciton lifetimes, which may be caused by differences in synthesis and ligands used.

We now discuss the influence of the excitation wavelength on the band edge dynamics. Fig. 2 shows time traces for excitations at 2.4 μm, 2.0 μm, 1.2 μm, 800 nm and 400 nm. The excitation densities for the data shown correspond to less than 0.2 photons absorbed per quantum dot on average, meaning these measurements are not distorted by multi-photon processes (details of the excitation density analysis can be found in the ESI†). All time traces have been normalized to their peak signal for easier comparability.
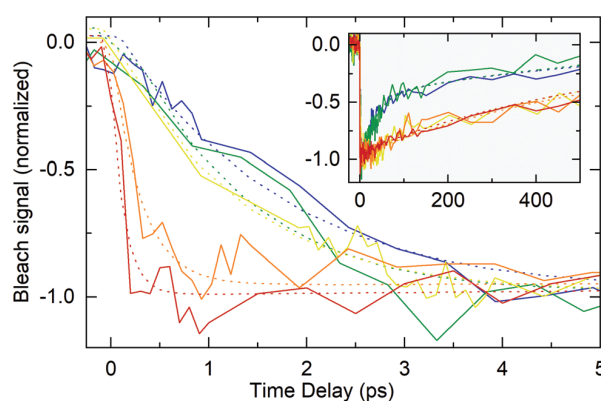

Fig. 2 Exemplary bleach signal at the band-gap of 0.5 eV (2.5 μm) for low excitation density (solid lines) and fits according to eqn (1) (dotted lines) for different pump wavelengths: 2.4 μm (red), 2.0 μm (orange), 1.2 μm (yellow), 800 nm (green) and 400 nm (blue). For 400 nm and 800 nm excitation, the long-lived dynamics are governed by multi-excitons generated through MEG.

27

For 2.4 μm, 2.0 μm and 1.2 μm the long-lived dynamics are well described by a single exponential decay with a lifetime of 623 ± 150 ps, shown as dotted lines. For 800 nm and 400 nm excitation, the photon energy exceeds the MEG threshold.[18] Consequently, the long-lived dynamics are governed by multi-excitons. These are no longer well described by a single exponential decay due to Auger recombination of multi-excitons as can be clearly seen in the inset. Apart from carrier multiplication, the excitation wavelength does not affect carrier dynamics past 5 ps after excitation in our data. This means that all intraband relaxation occurs within this time window. By comparing the early dynamics, a trend of longer rise times with higher photon energy can be observed. This trend can be expected because the carriers need to bridge increasingly larger energy differences between photon energy and particle band-gap. We also note that the nearly instantaneous rise of the bleach signal for resonant excitation at 2.4 μm within 111 ± 43 fs is faster than the instrument response function and therefore confirms a temporal resolution of ≲150 fs.

Fig. 3 shows the cooling time as a function of excitation density for all excitation wavelengths. For better comparison we normalize the fluence with respect to signal saturation (see ESI† for details). Below the MEG onset (for 2.4 μm, 2.0 μm and 1.2 μm excitation wavelength), Poissionian statistics can be employed to calculate the mean exciton number per quantum dot, $\langle N \rangle$, for which a direct correspondence to the normalized fluence, F/F_0, is found in the linear regime as detailed in the ESI.† We do not observe a dependence of intraband cooling time on excitation density. *I.e.* a ratio of F/F_0 = 0.5 corresponds to 25% of excited particles being doubly excited. Yet, no significant change in the cooling time is apparent within our experimental precision. Consequently, multi-particle scattering appears to play only a minor role in intraband relaxation in these quantum dots as also reported for much larger THz-gap HgTe crystallites.[39]

In the following discussion, the mean value of the cooling times for each excitation wavelength in Fig. 3 is used as a more precise value. Here, the inverse uncertainty of the fit results (error bars in Fig. 3) has been used to calculate the weighted average. The uncertainties correspond to the standard deviation of the fit results for the cooling time. These values are summarized in Table 1. The top left panel of Fig. 4 shows the relation between photon energy and cooling time. This representation also reflects the increase of cooling time with higher photon energy as already apparent in the time traces in Fig. 2. Moreover, the increment of cooling time compared to photon energy appears to stagnate past 1200 nm excitation wavelength, suggesting much higher energy dissipation rates for 800 nm and 400 nm excitation. However, these wavelengths lie in the MEG regime, resulting in the generation of more than a single exciton from a single photon. The initial intraband cooling process is complete within less than 5 ps regardless of excitation wavelength (*cf.* Fig. 2) while Auger recombination of multi-excitons requires several tens of picoseconds. This means that the electronic configuration after intraband cooling consists of several excitons in the MEG regime.

Given these different band-gap states for the different excitation regimes, we subtract the energy of the corresponding lowest (multi-) exciton energy from the photon energy in order to obtain a meaningful comparison for the energy dissipation during intraband cooling. Following results from photoconductivity measurements of HgTe quantum dots,[18] we subtract the lowest bi-exciton energy, E_{XX}, for 800 nm excitation and the energy of the lowest quadruple exciton, E_{XXXX}, for 400 nm excitation. Our approach is illustrated in the top left panel of Fig. 4 by arrows that correspond to the energy of the respective (multi-)excitons. The grey data points then correspond to the excess of absorbed photon energy that is dissipated during intraband cooling. This representation of our data reveals an essentially linear relationship between dissipated energy and cooling time with a mean energy dissipation rate 0.36 eV ps^{-1}. Individual cooling times and energy dissipation rates for all excitation wavelengths are summarized in Table 1.

Also shown in Fig. 4 is the single particle energy spectrum obtained from the pseudopotential calculations and the corresponding absorption spectrum. These calculations allow assigning the most probable electron and hole states after photo-excitation with 2.4 μm, 2.0 μm and 1.2 μm, shown as arrows in the level scheme. Most importantly, excitation at
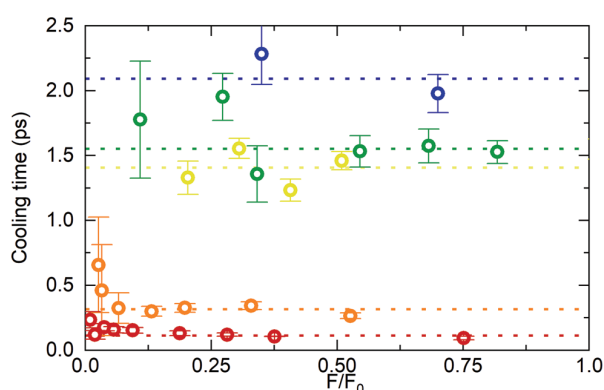

Fig. 3 Exciton cooling time as a function of excitation fluence for different wavelengths: 2.4 μm (red), 2.0 μm (orange), 1.2 μm (yellow), 800 nm (green) and 400 nm (blue). The dotted lines correspond to the weighted average for each excitation wavelength (also see Table 1).

Table 1 Cooling times, t_{cool}, and energy dissipation rates, k_{diss}

λ_{exc} (nm)	t_{cool} (fs)	k_{diss} (eV ps^{-1})
2400	(111) (±43)	—
2000	314 ± 136	0.39 ± 0.17
1200	1438 ± 141	0.37 ± 0.04
800	1552 ± 212	0.36 ± 0.05
400	2092 ± 152	0.34 ± 0.02

For 800 nm and 400 nm carrier multiplication was considered in the calculation of the excess energy. The rates for the resonant excitation at 2.4 μm are governed by the instrument response function.
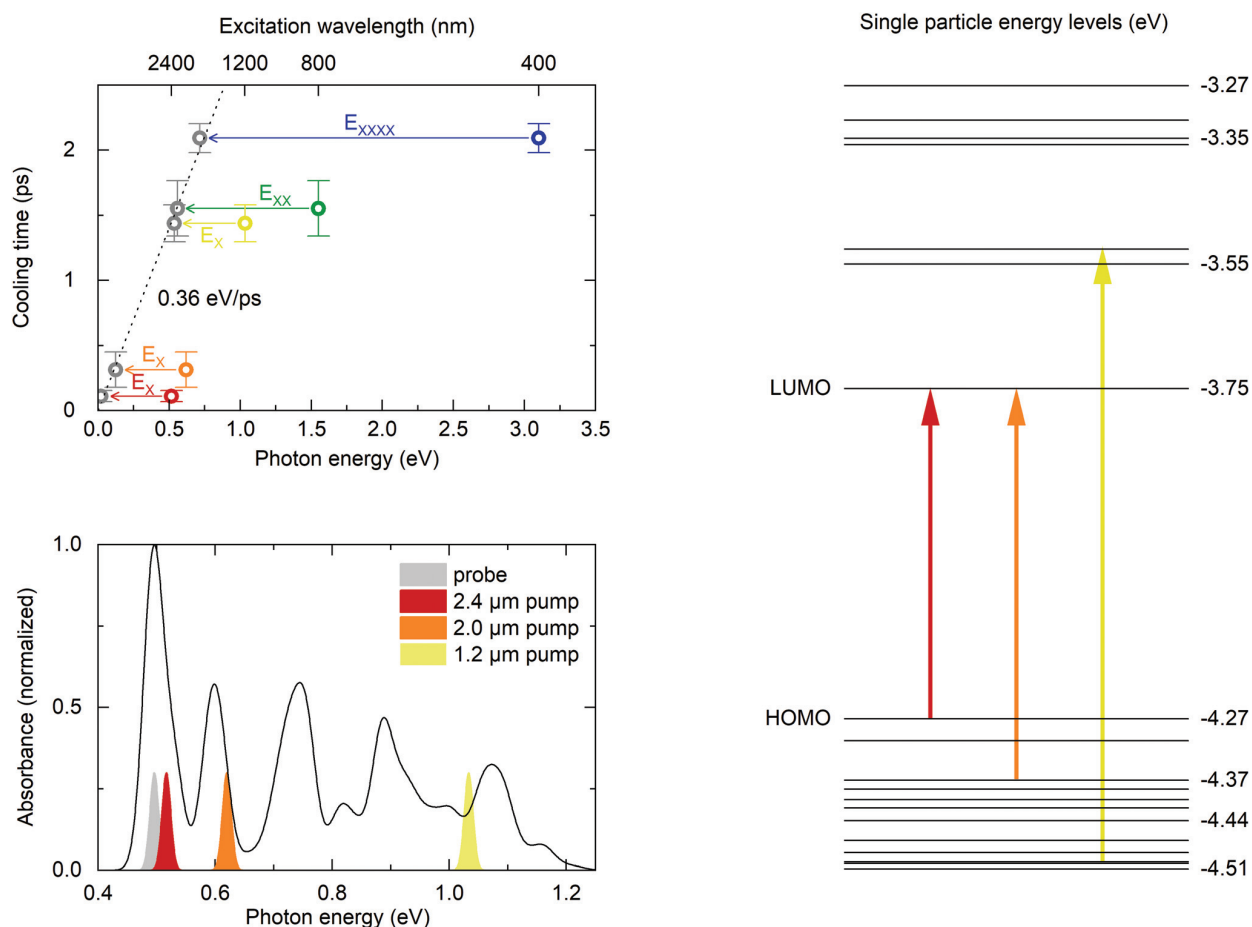
Fig. 4 Top left. Exciton cooling times as a function of photon energy. Colored data points represent mean values for the respective excitation wavelength, error bars correspond to the standard deviation of all measured cooling times in the linear regime. Arrows indicate the energy corresponding to the energetically lowest exciton (E_X), bi-exciton (E_{XX}) and quad-exciton (E_{XXXX}). This assignment of exciton multiplicity to photon energies is based recent results on MEG in HgTe NCs.[18] Subtracting the (multi-) exciton energies from the photon energies accordingly (grey symbols), reveals a linear relation between cooling time and energy to be dissipated from the electronic system at a rate of 0.36 eV ps^{-1}, independent of excitation wavelength or density of states. Bottom left. Calculated absorption spectrum and experimental spectra for pump and probe pulses. The calculated spectrum has been shifted by +33 meV to match the experimental bandgap. Right. Calculated level scheme and optical transitions.

2.0 μm creates only hot holes, allowing quantification of the $2S_h$-to-$1S_h$ relaxation time of 314 ± 136 fs, which is comparable to the rates found in CdSe NCs with similar $2s_h–1s_h$ energy spacings[40] and roughly one order of magnitude faster than in PbSe quantum dots with comparable hole energy spacing.[41] Excitation at 1.2 μm excites both, hot electrons and holes. Yet, the energy dissipation rates are identical within the margin of error for both excitations. We would like to note that our measurements are blind to the cooling rate associated to any states outside the band-gap, such as long-lived (surface)trap states as we do not measure depopulation of the hot state but population of the cold state. This means that these energy dissipation rates represent lower limits.

Several conclusions can be drawn from these observations. Most striking is the almost universal energy dissipation rate

independent of the initially excited state and hence, the density of states. By comparing the theoretically assigned initial states for excitation at 2.0 μm and 1.2 μm (as indicated in the right-hand side of Fig. 4), the presence of an excitation in the conduction band does not seem to influence the cooling rate of the system. This suggests mainly two options for intraband carrier relaxation. Firstly, the cooling rate in the conduction band could be identical to the cooling rate in the valence band. This seems unlikely given the large difference of level spacings in the conduction and valence bands, and much slower electron intraband relaxation times reported for doped MIR HgSe quantum dots in the range of tens to hundreds of picoseconds[9] and intraband lifetimes of more than 4 picoseconds reported for self-doped Terahertz-gap HgTe nanoparticles with roughly ten-fold smaller intraband gaps.[39]

Instead, these findings strongly point to Auger cooling as the dominant decay channel for conduction band relaxation in HgTe quantum dots, similar to CdSe quantum dots[12,13] where the process is well understood: electrons rapidly transfer energy to holes in the valence band through Auger coupling. The hole subsequently relaxes back to the band-gap by dissipating energy to phonons and/or ligands. Assuming Auger cooling to be much quicker than the relaxation of the hole, the overall energy dissipation rate would be equal to the dissipation rate of holes alone, which would explain the observation of similar energy dissipation rates for 2.0 μm and 1.2 μm excitation. In this scenario, electron intraband cooling *via* an Auger mechanism in HgTe quantum dots might be substantially slowed down by spatial separation of electrons and holes in heterostructured core–shell quantum dots.[8]

This still leaves the question of a universal hole cooling rate unanswered, as the higher density of states for hole excitations larger than 0.1 eV (see Fig. 4, right hand side) should lead to more efficient energy dissipation through coupling to phonons and, consequently, larger cooling rates for higher photon energies. This is clearly not what we observe, not even in the MEG regime close to the ionization threshold of the particles. A possible explanation could be nonadiabatic coupling of states as already discussed in carrier relaxation for CdSe and PbSe quantum dots[11,41] where it was argued that the transition rate for two states is scaling with the inverse of their energy spacing.[11,40] Such a scaling law would explain the observed constant energy loss rate independent of excitation energy.

Confirmation of this proposed mechanism requires further experiments. These could include similar experiments on MIR HgTe quantum dots of various sizes which will give insight into the influence of intraband energy level spacings and localization effects on carrier cooling. The Auger cooling processes could be addressed by using type II heterostructured quantum dots. Here, spatial separation of electrons and holes should slow down carrier cooling in the picture that we propose.[8] Further information on the role of ligands in carrier cooling can be accessed by ligand exchange studies or the use of type I core shell particles.

The cooling time found for 800 nm excitation also imposes an upper limit for the MEG process in MIR HgTe quantum dots which is at most 1.5 ps. Taking intraband-cooling into account as well, the process is likely much quicker than our temporal resolution of $\lesssim$150 fs. By estimating a mean carrier cooling time on the order of 1.4 ps after inverse Auger-recombination at an excess energy of one band-gap (see Fig. 4, excitation at 1.2 μm), a time-scale for electron–electron scattering during inverse Auger-recombination of 30 ps is retrieved in these particles. The time-scales obtained for the electron–electron interactions match theoretical calculations for inverse Auger-recombination and MEG in PbSe quantum dots[42] where the mismatch between the ultrafast sub-100 fs Auger process during MEG and inverse Auger recombination was attributed to the differences in the density of final states. If this reasoning also holds for HgTe quantum dots will have to be addressed in future theoretical studies.

Conclusion

We investigated the intraband relaxation in thiol-capped mid-infrared HgTe QDs by ultrafast infrared spectroscopy. This relaxation occurs with time constants of less than 2.1 ps independent of excitation wavelength and excitation density (within the linear regime) and without an apparent bottleneck process for carrier cooling. We identify the decay constant for the $2S_h$-to-$1S_h$ transition as 314 ± 136 fs. During intraband relaxation, the energy dissipation from the electronic system in MIR HgTe quantum dots is constant up to excitation energies close to the work function of HgTe which includes the MEG regime. A mean energy dissipation rate of 0.36 eV ps^{-1} indicates only a minor influence of the density of states on intraband cooling. These observations imply either identical cooling rates for electrons and holes or rapid energy transfer from electrons to holes through Auger cooling/heating as found in CdSe quantum dots. The latter cooling mechanism seems more likely given the much slower intraband cooling times reported for electrons in HgSe[9] and THz HgTe[39] quantum dots. While these findings can be brought to agreement with already existing concepts reminiscent of the carrier relaxation mechanisms found in CdSe quantum dots, further experiments are required to identify the underlying processes. Such mechanistic insight will ultimately allow for tailoring intraband dynamics in MIR quantum dots by either enhancing or suppressing relaxation pathways through *e.g.* heterostructuring[8] and/or choice of ligands and particle size. Furthermore, negligible fluence dependence on the cooling rates suggests that multiparticle scattering processes play only a minor role in carrier cooling which is consistent with a very recent report of intraband dynamics in THz HgTe quantum dots.[39] This conclusion is further supported by the unaltered cooling rate found for excitations in the MEG regime.

Data availability statement

The data that support the findings of this study are available from the corresponding author upon reasonable request.

Conflicts of interest

There are no conflicts to declare.

Acknowledgements

30

References

1 M. Li, *et al.*, Slow cooling and highly efficient extraction of hot carriers in colloidal perovskite nanocrystals, *Nat. Commun.*, 2017, **8**, 3–12.

2 M. Li, J. Fu, Q. Xu and T. C. Sum, Slow Hot-Carrier Cooling in Halide Perovskites: Prospects for Hot-Carrier Solar Cells, *Adv. Mater.*, 2019, **31**, 1–17.

3 R. D. Schaller and V. I. Klimov, High efficiency carrier multiplication in PbSe nanocrystals: Implications for solar energy conversion, *Phys. Rev. Lett.*, 2004, **92**, 1–4.

4 J. T. Stewart, *et al.*, Carrier multiplication in quantum dots within the framework of two competing energy relaxation mechanisms, *J. Phys. Chem. Lett.*, 2013, **4**, 2061–2068.

5 M. Li, *et al.*, Low threshold and efficient multiple exciton generation in halide perovskite nanocrystals, *Nat. Commun.*, 2018, **9**, 3–9.

6 U. Bockelmann and G. Bastard, Phonon scattering and energy relaxation in two-, one-, and zero-dimensional electron gases, *Phys. Rev. B: Condens. Matter Mater. Phys.*, 1990, **42**, 8947–8951.

7 C. Melnychuk and P. Guyot-Sionnest, Multicarrier dynamics in quantum dots, *Chem. Rev.*, 2021, **121**, 2325–2372.

8 A. Pandey and P. Guyot-Sionnest, Slow Electron Cooling in Colloidal, *Science*, 2008, **322**, 929–932.

9 C. Melnychuk and P. Guyot-Sionnest, Auger Suppression in n-Type HgSe Colloidal Quantum Dots, *ACS Nano*, 2019, **13**, 10512–10519.

10 P. Guyot-Sionnest, B. Wehrenberg and D. Yu, Intraband relaxation in CdSe nanocrystals and the strong influence of the surface ligands, *J. Chem. Phys.*, 2005, **123**, 074709.

11 R. R. Cooney, S. L. Sewall, K. E. H. Anderson, E. A. Dias and P. Kambhampati, Breaking the phonon bottleneck for holes in semiconductor Quantum dots, *Phys. Rev. Lett.*, 2007, **98**, 1–4.

12 P. Kambhampati, Hot exciton relaxation dynamics in semiconductor quantum dots: Radiationless transitions on the nanoscale, *J. Phys. Chem. C*, 2011, **115**, 22089–22109.

13 E. Hendry, *et al.*, Direct observation of electron-to-hole energy transfer in CdSe quantum dots, *Phys. Rev. Lett.*, 2006, **96**, 1–4.

14 F. C. M. Spoor, *et al.*, Hole cooling is much faster than electron cooling in pbse quantum dots, *ACS Nano*, 2016, **10**, 695–703.

15 F. C. M. Spoor, S. Tomić, A. J. Houtepen and L. D. A. Siebbeles, Broadband Cooling Spectra of Hot Electrons and Holes in PbSe Quantum Dots, *ACS Nano*, 2017, **11**, 6286–6294.

16 P. Geiregat, *et al.*, A phonon scattering bottleneck for carrier cooling in lead-chalcogenide nanocrystals, *Mater. Res. Soc. Symp. Proc.*, 2015, **1787**, 1–5.

17 C. Melnychuk and P. Guyot-Sionnest, Slow Auger Relaxation in HgTe Colloidal Quantum Dots, *J. Phys. Chem. Lett.*, 2018, **9**, 2208–2211.

18 C. Livache, *et al.*, Band Edge Dynamics and Multiexciton Generation in Narrow Band Gap HgTe Nanocrystals, *ACS Appl. Mater. Interfaces*, 2018, **10**, 11880–11887.

19 E. Lhuillier, S. Keuleyan, H. Liu and P. Guyot-Sionnest, Mid-IR colloidal nanocrystals, *Chem. Mater.*, 2013, **25**, 1272–1282.

20 S. E. Keuleyan, P. Guyot-Sionnest, C. Delerue and G. Allan, Mercury telluride colloidal quantum dots: Electronic structure, size-dependent spectra, and photocurrent detection up to 12 μm, *ACS Nano*, 2014, **8**, 8676–8682.

21 N. Goubet, *et al.*, Terahertz HgTe Nanocrystals: Beyond Confinement, *J. Am. Chem. Soc.*, 2018, **140**, 5033–5036.

22 A. Chu, *et al.*, HgTe Nanocrystals for SWIR Detection and Their Integration up to the Focal Plane Array, *ACS Appl. Mater. Interfaces*, 2019, **11**, 33116–33123.

23 X. Tang, M. M. Ackerman, M. Chen and P. Guyot-Sionnest, Dual-band infrared imaging using stacked colloidal quantum dot photodiodes, *Nat. Photonics*, 2019, **13**, 277–282.

24 P. Guyot-Sionnest, M. M. Ackerman and X. Tang, Colloidal quantum dots for infrared detection beyond silicon, *J. Chem. Phys.*, 2019, **151**, 06090.

25 M. M. Ackerman, M. Chen and P. Guyot-Sionnest, HgTe colloidal quantum dot photodiodes for extended short-wave infrared detection, *Appl. Phys. Lett.*, 2020, **116**, 083502.

26 S. S. Chee, *et al.*, Correlating Structure and Detection Properties in HgTe Nanocrystal Films, *Nano Lett.*, 2021, **21**, 4145–4151.

27 C. Gréboval, *et al.*, Mercury Chalcogenide Quantum Dots: Material Perspective for Device Integration, *Chem. Rev.*, 2021, **121**, 3627–3700.

28 J. Qu, *et al.*, Electroluminescence from HgTe Nanocrystals and Its Use for Active Imaging, *Nano Lett.*, 2020, **20**, 6185–6190.

29 P. Geiregat, *et al.*, Continuous-wave infrared optical gain and amplified spontaneous emission at ultralow threshold by colloidal HgTe quantum dots, *Nat. Mater.*, 2018, **17**, 35–41.

30 H. Goodwin, T. C. Jellicoe, N. J. L. K. Davis and M. L. Böhm, Multiple exciton generation in quantum dot-based solar cells, *Nanophotonics*, 2018, **7**, 111–126.

31 R. A. Kaindl, *et al.*, Generation, shaping, and characterization of intense femtosecond pulses tunable from 3 to 20 μm, *J. Opt. Soc. Am. B*, 2000, **17**, 2086.

32 J. R. Cárdenas and G. Bester, Atomic effective pseudopotentials for semiconductors, *Phys. Rev. B: Condens. Matter Mater. Phys.*, 2012, **86**, 30–37.

33 A. Karpulevich, H. Bui, D. Antonov, P. Han and G. Bester, Nonspherical atomic effective pseudopotentials for surface passivation, *Phys. Rev. B*, 2016, **94**, 1–10.

34 F. Zirkelbach, P. Y. Prodhomme, P. Han, R. Cherian and G. Bester, Large-scale atomic effective pseudopotential program including an efficient spin-orbit coupling treatment in real space, *Phys. Rev. B: Condens. Matter Mater. Phys.*, 2015, **91**, 1–16.

35 H. Bui, A. Karpulevich and G. Bester, Excitonic fine structure of zinc-blende and wurtzite colloidal CdSe nanocrys-

tals and comparison to effective mass results, *Phys. Rev. B*, 2020, **101**, 1–9.

36 G. Bester, Electronic excitations in nanostructures: An empirical pseudopotential based approach, *J. Phys.: Condens. Matter*, 2009, **21**, 023202.

37 V. I. Klimov, A. A. Mikhailovsky, D. W. McBranch, C. A. Leatherdale and M. G. Bawendi, Quantization of multiparticle Auger rates in semiconductor quantum dots, *Science*, 2000, **287**, 1011–1014.

38 V. I. Klimov, J. A. McGuire, R. D. Schaller and V. I. Rupasov, Scaling of multiexciton lifetimes in semiconductor nanocrystals, *Phys. Rev. B: Condens. Matter Mater. Phys.*, 2008, **77**, 1–12.

39 T. Apretna, *et al.*, Few picosecond dynamics of intraband transitions in THz HgTe nanocrystals, *Nanophotonics*, 2021, **10**, 2753–2763.

40 R. R. Cooney, *et al.*, Unified picture of electron and hole relaxation pathways in semiconductor quantum dots, *Phys. Rev. B: Condens. Matter Mater. Phys.*, 2007, **75**, 1–14.

41 R. D. Schaller, *et al.*, Breaking the phonon bottleneck in semiconductor nanocrystals via multiphonon emission induced by intrinsic nonadiabatic interactions, *Phys. Rev. Lett.*, 2005, **95**, 1–4.

42 A. Franceschetti, J. M. An and A. Zunger, Impact ionization can explain carrier multiplication in PbSe quantum dots, *Nano Lett.*, 2006, **6**, 2191–2195.

32

3.5 Results and perspective: 2D spectroscopy of MIR QDs

The localization energy in quantum dots inherently ties the size distribution of a quantum dot ensemble to an inhomogeneous line broadening (see equation 3.1). The ability to largely ignore static inhomogeneous broadening [59] thus makes two-dimensional spectroscopy an incredibly valuable tool to examine quantum dot systems on a fine-structure level otherwise concealed by size inhomogeneity [107]. In the following section, first 2D spectra of HgTe QDs, which have been recorded during this thesis, are presented and discussed.

Figure 3.4 shows 2D spectra for thiol capped HgTe nanoparticles dissolved in tetrachloroethylene at population times of 5 ps, 25 ps and 100 ps. In the bottom left panel, the 2D correlation maps for the population times of 5 ps, 100 ps and -100 ps were integrated along the excitation axis to obtain the corresponding pump probe spectra. Also shown is the static FTIR absorption spectrum and the spectrum of the fs IR pulse.

As there are no comparable spectra or theory available in the literature, the plausibility of these spectra needs discussion. As an initial check, the noise, also shown in figure 3.5 in these spectra is evaluated. Its main component is the interference between the two pump pulses, which gives rise to a purely diagonal signal that can be removed by employing a different chopping scheme in future experiments. By comparison of the integrated signals in the bottom left panel of figure 3.4, it is evident, that the signals at positive waiting times are larger than the noise level and decay as the population time increases, confirming the observation of a transient decay. To also exclude systematic errors such as contributions from windows or the solvent, the pump probe spectrum is constructed from the FTIR spectrum. In the absence of induced absorption features, only ground state bleach and induced absorption need be considered. Since they resemble the negative ground state absorption the FTIR spectrum can be scaled with the square of the pulse spectrum as a reasonable approximation. This is also shown in grey in the bottom left panel. The integrated spectra for both 5 ps and 100 ps waiting time clearly resemble this feature, assuring the spectra can be attributed to the HgTe particles.

At first glance, it can be seen that the homogeneous linewidth is smaller than the ensemble linewidth. Consequently, there is significant line broadening due to size distribution cloaking fine structure features, which, in an ensemble, can only be observed using 2d spectroscopy or micro photo luminescence (micro PL). However, micro PL only reveals the inhomogenous broadening of the fluorescent states and requires an additional dedicated setup involving expensive infrared confocal microscopes.
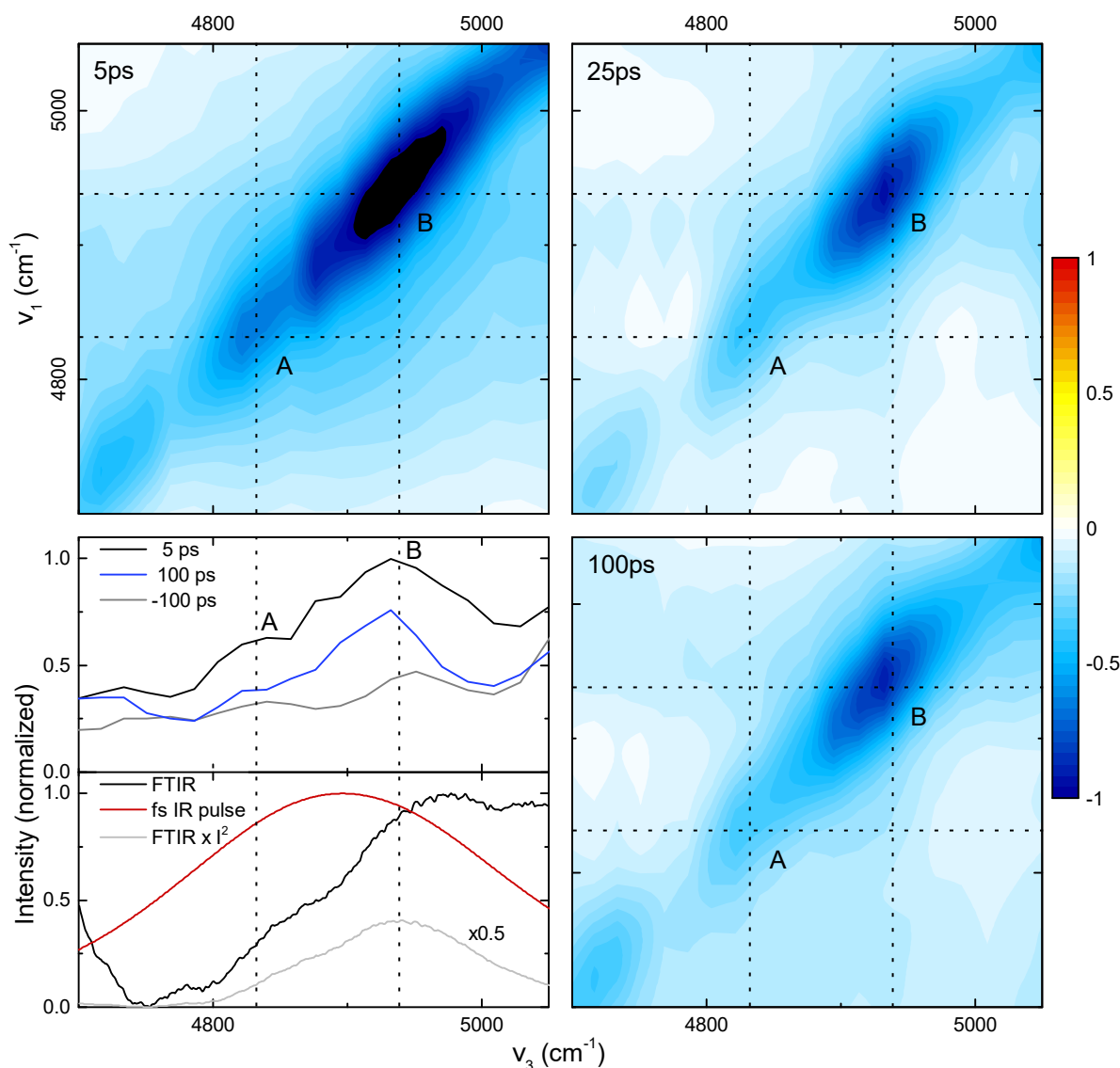
Figure 3.4: 2D spectra of HgTe QDs with a band-gap of 4900 cm^{-1} at population times of 5 ps 25 ps and 100 ps. The bottom left panel shows the 2D signal integrated along the excitation axis for population times of 5 ps 100 ps and -100 ps, where the signal for -100 ps resembles an estimate for the noise level (top). On the bottom half of the bottom left panel, the FTIR spectrum of the nanoparticles along with the pulse spectrum used in the 2D experiment is shown. Also shown is the FTIR spectrum after multiplying it with the squared pulse intensity, giving a measure for the expected 2D signal. A (4830 cm^{-1}) and B (4940 cm^{-1}) denote the two most distinct spectral features in the integrated signal.

For all waiting times, two prominent spectral features, labeled A (4830 cm^{-1}) and B (4940 cm^{-1}) are observed on the diagonal of the spectra. These coincide with the two pronounced features in the FTIR spectrum, which is in agreement with reports of negligible photo-luminescence shifts in HgTe QDs [90, 108]. Their respective off-diagonal features are symmetric, indicating a shared state (see figure 2.5), which is most appar-

ent at a waiting time of 25 ps. They have common a homogeneous linewidth of $70\,\mathrm{cm}^{-1}$ (FWHM)[1] and a inhomogeneous linewidth of $100\,\mathrm{cm}^{-1}$ (FWHM)[2], revealing significant inhomogenous broadening due to size distribution. Their separation is only $110\,\mathrm{cm}^{-1}$, or $13.6\,\mathrm{meV}$, respectively. Thus, a shared state in the conduction band is more likely for these excitations, as the conduction band level spacings for similar systems are typically several $100\,\mathrm{meV}$ with a twofold degenerate state at the band gap [100, 101]. The observed energy difference is in reasonable agreement with the predicted energy difference between the two lowest valence states in similar systems [100]. However, intra band relaxation, as discussed in sections 3.4 and 3.2, should lead to a sub $100\,\mathrm{fs}$ relaxation from state B should state A in that case, resulting in a strong off-diagonal feature, which is absent in these spectra. Thus, the assignment of state B being the lowest excitonic state and A being a mid gap state involving the sulfur atom from the thiol group of the ligand, which can have radiative lifetimes in the µs range [98] seems more reasonable. As the energy splitting is roughly half the thermal energy at room temperature, also the static absorption connected with such a gap state is plausible.In this picture, the additional diagonal feature at a frequency of $B\,(4720\,\mathrm{cm}^{-1})$ could also be assigned to another mid-gap state, which is hidden by the flank of the combination band in the FTIR spectrum.

As only spectra for three waiting times are available, no timescales or oscillatory behavior of spectral features can be discussed. Yet, these snapshots represent important regimes during band-gap relaxation. As bi-exciton decay in these systems occurs on 30 ps timescales (also see figure 3.3), the correlation map for a waiting time of 5 ps should have bi-exciton contributions, while bi-excitons should have completely decayed by 100 ps. The complete absence of induced absorption features connected to bi-excitons may be confusing at first, but have been demonstrated to be only observable during the first few $100\,\mathrm{fs}$ in an inhomogeneous ensemble of CdSe quantum dots [55].

Moreover, all intra band relaxation processes should have been long completed by 5 ps (see section 3.4), yet no cross peaks are apparent in this spectrum, meaning that the probed state is already the lowest electronic excitation. Only a small asymmetry in the 100 ps correlation map hints towards the possibility of weak population transfer from state B to state A.

An extended spectral range for the correlation map at 25 ps alongside the correlation map at -100 ps and the extended FTIR spectrum of the sample are shown in figure 3.5. The off diagonal feature in figure 3.5 is exemplarily shown for a waiting time of 25 ps, where it is most prominent. This may be a hint towards direct energy transfer between excitonic states and ligand or solvent modes. The slight red shift of this feature compared to the states A and B could be explained by the bi-exciton shift. In this picture one exciton recombines and transfers its energy to the combination band. Similar Auger-like energy transfer to ligands has already been observed both, theoretically and experimentally for CdSe QDs [109]. This interpretation would be also be consistent with the absence of the cross-peak at a waiting time of 100 ps, where all biexcitons should have long decayed (compare figure 3.3). Yet this has to be treated very cautiously due to the overall quality

---

[1]Extracted from a cut parallel to the excitation axis and re-scaled by dividing by $\sqrt{2}$, accordingly.

[2]Obtained from Gaussian fits of the respective FTIR features a a shared width. Also shown in figure 3.5

of data especially since this feature is only covered by the flank of the fs pulse.

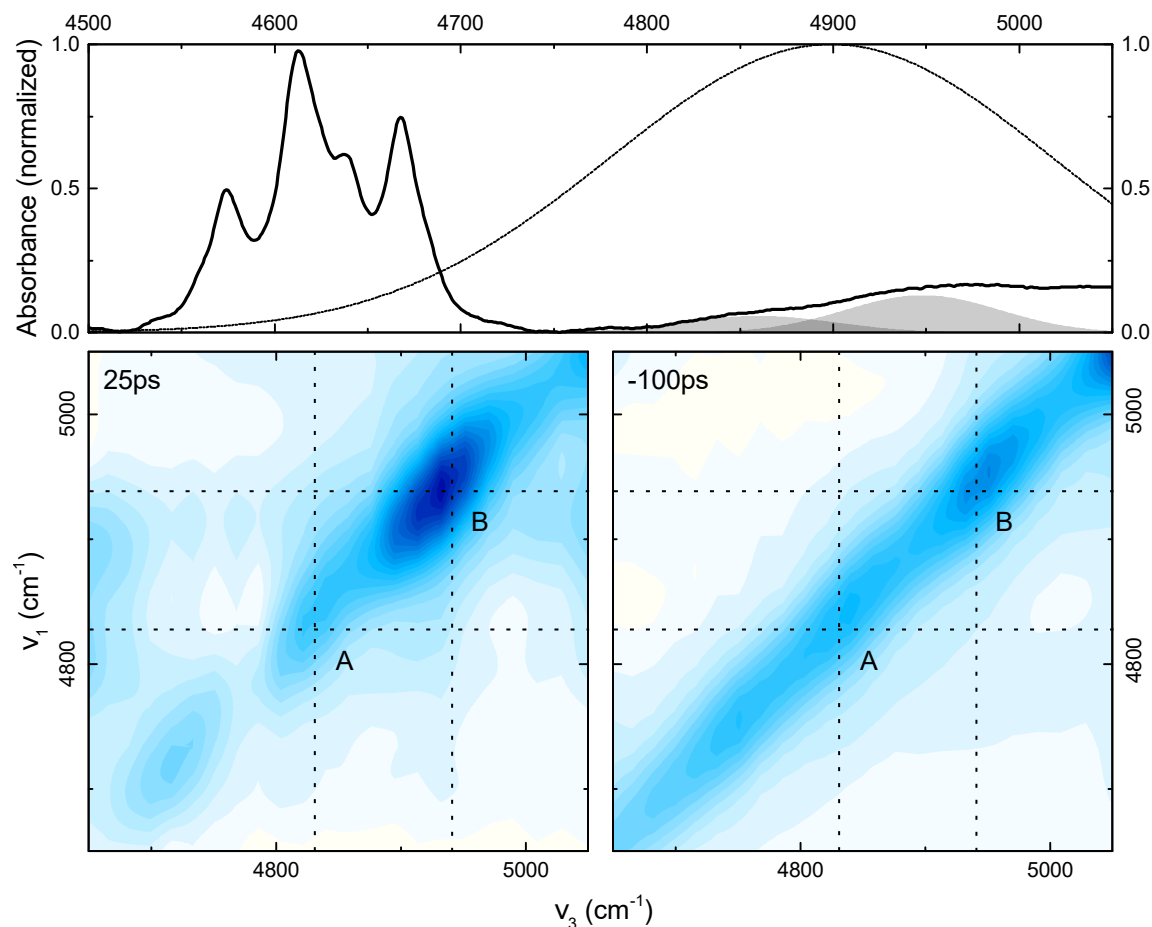In summary, the capability to record 2d spectra for HgTe QD samples was demonstrated.

Figure 3.5: Top FTIR spectrum of thiol capped HgTe QDs dissolved in a mixture of TCE and toluene. Also shown if the spectrum of the fs IR pulse and Gaussian fits for the lowest QD excitation. Extended spectral range for the correlation map at a waiting time of 25 ps shown in figure 3.4 the cross-peak at a detection frequency of 4650 cm^{-1} in resonance with the excitation frequency of the quantum dot states may indicate direct energy transfer from the electronic system to the combination band (left). Estimate for the noise level in the 2D correlation maps shown in figure 3.4, recorded at a waiting time of -100 ps (right).

First results provide additional insight into the nature of two transitions observed in static absorption spectra labeled A,B in figure 3.4. The symmetric off diagonal features indicate a shared conduction band state, while the absence of significant population transfer makes two excitonic states highly improbable. The resulting interpretation is the assignment of a mid-gap state involving sulfur atoms from the ligand to transition A, a hypothesis that can be tested using FTIR spectra at cryogenic temperatures in the future. The population of mid-gap states should vanish for sufficiently low temperatures, and consequently the respective absorption features, which could be tested through cryogenically cooled FTIR spectroscopy.

The capability of performing two-dimensional infrared measurements opens up a vast

range of future experimental capabilities regarding state-resolved intra-band and bi-exciton dynamics. First steps include the completion of the above presented data set in terms of a better sampling of population dynamics and employing a proper chopping scheme, thus eliminating the main source of noise. This will yield timescales for the individual features allowing further interpretation and uncovering potential oscillatory features due to quantum coherences. Especially the further investigation of the hint towards direct energy transfer from the electronic system to ligand modes as indicated in figure 3.5 may provide insight into the underlying mechanism, which is still unclear. Additionally, bi-excitonic shifts may be obtainable from correlation maps at early waiting times, as the respective induced absorption features are expected to only appear on a sub picosecond time-scale in inhomogeneous ensembles [55].

On a longer timescale, spectral extension of pump and probe pulses using coherent white light sources [110] may be implemented to further investigate the dynamics discussed in section 3.4. This would provide the capability of direct observation of state to state transitions, making indirect measurements and effective cooling rates obligatory.

4 Time-resolved spectroscopy of vibrationally labeled proteins

4.1 Introduction

Proteins are the basic building blocks of any biological organism. In the human body, they provide almost any critical biological function including the contraction of muscles, oxygen transportation, enzymatic processes in digestion and the immuno response [111].
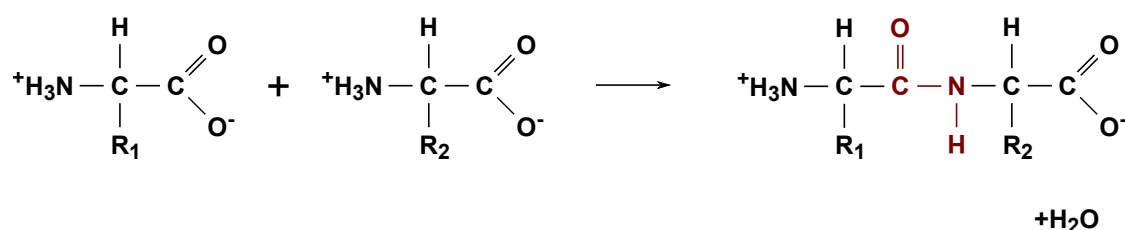

Figure 4.1: Formation of a polypeptide from two amino acids, with their respective side chains R_1 and R_2, adapted from [112]. Highlighted in red is the amide group, which interconnects the two amino acids by a peptide bond.

To understand these functions of proteins on a fundamental level, it is necessary to study their structural dynamics. Each protein is built from a subset of 20 universal amino acids, which are cast together by peptide bonds as shown in figure 4.1. More aminoacids can be added to this polypeptide indefinitely by consecutive peptide bonding, as this reaction merges two amino acids into a single larger amino acid, forming polypetide chains. The sequence of a protein's polypeptide chain is encoded in the DNA and already defines the unique three dimensional structure of the folded protein and hence, its function [112]. Highlighted in red in figure 4.1 is the amide group interconnecting the amino acids building blocks and engages in hydrogen bonds to form the secondary protein structure, such as α-helices and β-sheets. The vibrational excitations of such amide groups provide a useful handle to spectroscopically study protein structure, as they directly probe the inter-atomic potentials at the backbone of the protein. These vibrational bands are known as the amide bands, which are classified as amide A,B at $3100 - 3400\,\mathrm{cm}^{-1}$ attributed to the NH stretching vibration and amide I-VI at $<1700\,\mathrm{cm}^{-1}$ [39]. Especially the amide I

band at $1600-1700\,\mathrm{cm}^{-1}$ has been of interest for structural investigation, due to its strong contribution from the C=O stretching vibration, which exerts a large dipole moment and directly probes the amide oxygen playing a central role in the formation of secondary structure motifs [48, 39]. Yet, overlapping bands obscure spectral signatures due to the sheer size of proteins, often consisting of several thousands of atoms. One possibility to overcome this problem is to introduce a chemical group with a spectrally isolated transition into the protein, so called vibrational dynamic labels (VDLs). Such a VDL then acts as a local observer of electric field, solvent exposure and changes in protein structure. Ideally such a probe can be implemented into any position in the protein, without altering the protein structure or dynamics. As proteins are rarely stable at concentrations in the few mMol/L range, a high dipole moment and a transition frequency outside the water absorption are desired to provide reasonable signal to noise ratios in the proteins native aqueous environment. To this end, several specifically designed slightly mutated forms of proteins with isolated vibrational transitions outside the amide bands and water absorption have been investigated for their suitability. Such mutations range from minuscule changes in protein structure, such as replacing a hydrogen atom with a heavier isotope, resulting in a down shift in frequency due to the increased mass, up to the introduction of non-naturally occurring amino acids to incorporate cyano, thiocyanate or azide groups into the protein. The biochemical synthesis of these mutants is beyond the scope of this thesis and is summarized elsewhere [41]. As there is no ideal VDL, the most suitable label strongly depends on the application [40, 41]. For instance, isotope labeling results in the least perturbation of the native protein structure but also provides a minuscule dipole moment, which makes it unsuitable for nonlinear spectroscopies. The azido group has the largest dipole moment (up to two orders of magnitude larger compared to deuterium labels) of the above mentioned vibrational probes, which motivated its pioneering use for 2D spectroscopy of vibrationally labeled proteins [6]. However, it exerts a Fermi resonance [42] which complicates the interpretation of spectral shifts and accelerates the decay of vibrational excitation to few picoseconds, obstructing its applications as an observer of typically much slower protein dynamics [6]. The spectral signature of the cyano and thiocyanate groups is not obscured by Fermi resonances, but comes at the cost of 2-5 times weaker dipole transitions compared to the azide group making nonlinear spectroscopies extremely challenging, still first successful steps towards their application have been made [113, 114, 115].

4.2 Fermi resonances

Fermi resonances are an important phenomenon in spectroscopy, which is especially true for VDLs based on the azido stretching mode. They are the result of the mixing of two almost degenerate states of which exactly one is a dark state, for example a combination band or overtone in vibrational spectroscopy. This leads to often unexpected and hard to identify [116] asymmetric line-shapes. As such they can complicate the interpretation infrared spectra, which motivates approaches such as their circumvention via isotope
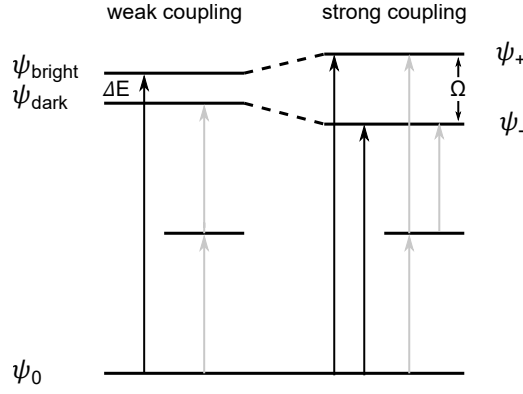
Figure 4.2: Illustration of a Fermi resonance for close energetic vicinity of a dipole allowed transition (depicted as arrows) and an overtone. In the weak coupling regime, only the optically active bright state, Ψ_{bright} absorbs, while direct excitation of the overtone Ψ_{dark} is symmetry forbidden. If those states are coupled by some coupling constant Ω, also see the Hamiltonian in equation 4.1, the states are mixed, leading to dipole allowed transitions into both superposition states Ψ_+ and Ψ_-, resulting in the emergence of a second (often unexpected) peak in the spectrum. The same arguments can be made for the induced absorption feature of the overtone, depicted as grey arrows.

shifting of the energy separation between the unperturbed states [117]. However, there also are approaches to utilize the properties of FRs, such as modifying Fermi resonances by modulation of pressure and temperature to identify underlying physical quantities, namely the unperturbed energy shift and molecular coupling of the transitions involved [118]. There also have been reports that FRs may be utilized as tools in order to spectroscopically access the hydrogen bonding status through the molecular coupling term [119]. Following [47], Fermi resonances are best understood by considering the following Hamiltonian in the basis $\{\Psi_0, \Psi_{dark}, \Psi_{bright}\}$, denoting ground state, the optically inactive dark state and the dipole allowed bright state respectively.

$$\hat{H} = \begin{pmatrix} 0 & 0 & 0 \\ 0 & E_{dark} & \Omega/2 \\ 0 & \Omega/2 & E_{bright} \end{pmatrix} \tag{4.1}$$

Here, Ω describes the (molecular) coupling of dark and bright state. By bringing the Hamiltonian into its diagonal form, its new Eigenenergies, $E_\pm$, are found as

$$E_\pm = \frac{E_{dark} + E_{bright}}{2} \pm \frac{1}{2}\sqrt{\Delta E^2 + \Omega^2}. \tag{4.2}$$

Where, $\Delta E = E_{bright} - E_{dark}$, is the energy difference of the uncoupled states. The Eigenstates of the coupled system are superpositions of the uncoupled states. This causes the initially dark state to obtain a optically active contribution to its wavefunction, thus appearing in the absorption spectrum, leading to an asymmetric line-shape. This can be explored looking at extremes for the ratio between the coupling strength and energy separation of the states, $\frac{\Omega}{\Delta E}$. For weak coupling and /or large energy separation, $\frac{\Omega}{\Delta E} << 1$,

the states are essentially uncoupled and the Eigenfunctions, $\Psi_\pm$ remain largely unchanged: $\Psi_+ \approx \Psi_{bright}$, $\Psi_- \approx \Psi_{dark}$, meaning only the bright state remains optically active. For almost degenerate states and / or large molecular couplings, $\frac{\Omega}{\Delta E} >> 1$ the Eigenfunctions are equal superpositions of bright and dark state,:

$$\Psi_\pm = \frac{1}{\sqrt{2}} \left(\Psi_{bright} \pm \Psi_{dark} \right). \tag{4.3}$$

This also means, both states $\Psi_\pm$ carry the same dipole moment for transitions from or to the ground state, Ψ_0. This means, for coupling strengths on the order of the energy separation, the mixing of the states grows with rising coupling strength, or declining energy separation. With stronger mixing of the states, the dipole moment from the bright state also increasingly transitions to the dark state, typically leading asymmetric line-shapes. This also makes the spectra of Fermi resonances, especially the relative intensity of the transitions, very sensitive to changes in energy separation and the coupling of the bright and dark state.

4.3 Quantum beats in pump probe spectroscopy

If two states can be simultaneously excited within the spectrum of the pump pulse, as often the case for, but not limited to Fermi resonances, the set of Feynman diagrams for induced absorption and stimulated emission need to be extended as shown in figure 4.3. Coherences between these two states, named 1 and 1' in figure 4.3, then lead to an
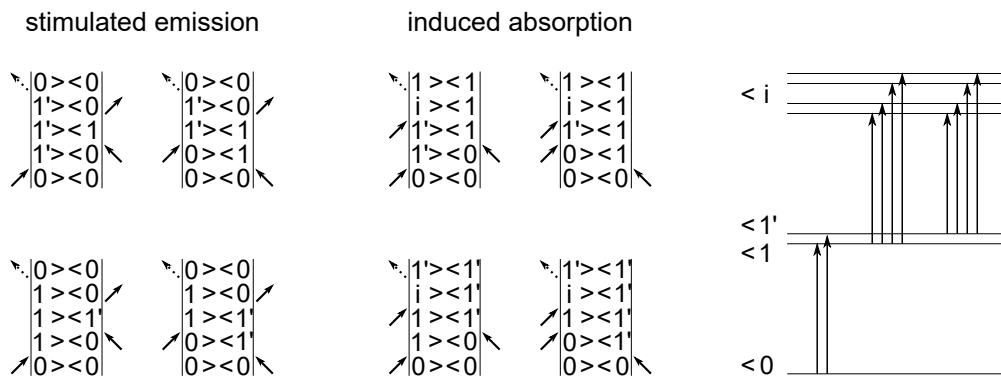

Figure 4.3: Additional Feynman diagrams for densely packed levels in pump probe experiments. Coherences of states that can be simultaneously excited within the bandwidth of the pump pulse lead to an additional oscillatory feature during the population time.

oscillatory behavior during the population time ,τ_2. Following equation 2.15 , the optical

response for induced absorption then reads

$$\Delta A(\omega, \tau_2) \propto (-1) \cdot \mu_{10}\mu_{1'0}|\mu_{i1}|^2 \frac{\Gamma_{|i\rangle\langle 1|}}{(\omega - \omega_{|i\rangle\langle 1|})^2 + \Gamma_{|i\rangle\langle 1|}^2} \cdot \cos\left(\frac{i}{\hbar} \cdot (\epsilon_{1'} - \epsilon_1)\tau_2\right) e^{-\frac{\tau_2}{\Gamma_{|1'\rangle\langle 1|}}}$$

(4.4)

Here, the index i denotes implicit summation over all overtones. The response functions tied to the remaining Feynman diagrams will be modulated by a damped cosine term oscillating at a beating frequency corresponding to the energy separation of the $\omega_{beat} = i/\hbar \cdot (\epsilon_{1'} - \epsilon_1)$ accordingly.

In other words, the induced absorption and stimulated emission features are periodically modulated by this quantum beat, where the frequency corresponds to the energy difference of the states 1 and 1' and the damping term is the dephasing time of the coherence. This beating mode can also be interpreted as a time-domain Raman mode of the excited state and can easily be mistaken as bi-exponential decay of the population state in the limit of long oscillation periods and rapid dephasing times.

4.4 Results: vibrational relaxation and induced absorption of AzF in Calmodulin complexes

The calcium-sensitive (Ca^{2+}) second messenger protein Calmodulin translates Ca^{2+} signals into cellular processes by inhibiting or activating secondary proteins and amino acids [120]. Upon binding Ca^{2+} at its four binding sites it undergoes conformational change, making it more hydrophobic and consequently, more prone to binding to its target proteins [121]. Among other functions, it plays a major role in muscle contraction and regulates numerous enzymes [121]. Its relatively high stability and heat resistance [121] make it an ideal system to study fundamental processes in proteins and for the development of novel methods, such as the use of different vibrational dynamic labels (VDLs) in FTIR studies discerning different conformation [122, 7].

The following manuscript concludes the results of measurements on several complexes of Calmodulin mutants labeled with p-azido-phenylalanine (AzF). The conformation specificity of the spectral signature of AzF had previously been demonstrated for the time-resolved observation in photo active proteins [8]. Yet, the goal of the time resolved measurements here is not to follow protein dynamics, but to grasp a better understanding of the interaction of the VDL with its immediate surroundings. To this end, the vibrational relaxation of the azido stretching vibration at $2120\,\mathrm{cm}^{-1}$ is investigated in different conformational states, which had already been characterized by FTIR studies [7]. This unveils the conformation specific induced absorption spectrum, providing access to higher excitations of the inter-atomic potential of the VDL. Additionally, the vibrational relaxation dynamics are interpreted as overdamped quantum beats, which allows for a more rigorous interpretation of the complex FTIR signature in different protein confor-

mations, which are governed by a Fermi resonance. Further theoretical and structural examination of the system are required to obtain underlying physical quantities such as coupling strength, Ω, or the unperturbed energy separation, ΔE, as introduced in section 4.2. Nonetheless, correlating the linear spectrum and vibrational decay dynamics by using the duality between time-resolved quantum beats and the static FTIR spectrum greatly increases the extent to which the spectral signature of the VDL can be interpreted and understood. This analysis indicates that the differences in the spectral signature of the bright transition alone may be minuscule compared to the changes of the overall line-shape in-between different protein complexes. This suggests that the Fermi resonance may increase the sensitivity of AzF with respect to changes in its surroundings. Through this, VDLs exhibiting Fermi resonances might even be advantageous for FTIR applications despite often being regarded as an undesired complication of the linear spectrum.

Article

Population Dynamics of Stretching Excitations of p-Azido-phenylalanine Incorporated in Calmodulin−Peptide Complexes

Matthias Ruppert,[∥] Anne Creon,[∥] Henning Tidow,* and Nils Huse*

Read Online

ACCESS | Metrics & More | Article Recommendations | ● Supporting Information

ABSTRACT: We genetically incorporated the unnatural amino acid p-azido-phenylalanine (AzF) into the ubiquitous Ca^{2+} sensor protein calmodulin (CaM) in complex with different peptides to explore the response of the azido stretching line shape to varying binding motifs with femtosecond infrared spectroscopy. The dynamic response of the azido stretching mode varies in different CaM−peptide complexes. We model these dynamics as coherent excitations of Fermi resonances and extract a lifetime of the azido stretching vibration of about 1 ps. The resulting model parameters are commensurate with the linear infrared absorption lineshapes which suggests that the conformation-sensitive vibrational lineshape could be composed of Fermi resonances that differ between the protein−peptide complexes.
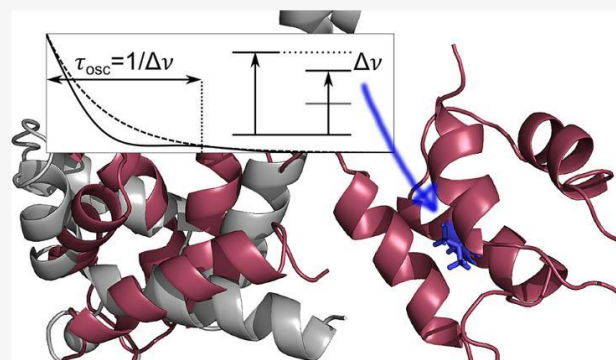
INTRODUCTION

Accessing structural fluctuations and configurational changes of proteins in ambient solution is a hallmark of NMR spectroscopy. In an analogous fashion, time-resolved vibrational spectroscopy accesses ambient protein dynamics in solution on time scales not accessible by (and hence complementary to) NMR spectroscopy. Unnatural or isotopically substituted amino acids provide the necessary spectral specificity via chemical groups with distinct vibrational frequencies. The site-specific incorporation of these amino acids spatially maps their highly localized vibrations within a protein to the respective absorption bands. Such unnatural amino acids (UAAs) have been established as vibrational dynamic labels (VDLs)[1−5] with transition frequencies within the infrared spectral water window but outside the fingerprint region of proteins. They act as ultrafast (<1 ps) sensors of local fluctuations and structural dynamics invoked by light, temperature jumps, local electric fields, pH changes, or chemical bonding[2,6−12] to follow processes such as vibrational energy transfer[13−15] or configurational evolution.[11,16]

Vibrational resonances with single-transition lineshapes facilitate spectral interpretation of frequency shifts, line broadening, and spectral inhomogeneity. Commonly used infrared-active VDLs that fulfill these spectral requirements usually contain groups such as −SCN, −CN, and −N_3 (coupled to aliphatic residues) with advantages and disadvantages of the different VDLs recently reviewed by Kim and co-workers as well as Adhikary and co-workers.[17,18] Generally, the particular application determines the choice of VDL with regard to desirable properties, such as oscillator strength, vibrational lifetime, line shape analysis, and (bio)chemical

incorporation strategy. For instance, SCN-based UAAs excel at vibrational lifetimes but have up to 10-fold weaker transition moments compared to azido-based UAAs.[18] The comparatively large oscillator strength of the azido stretching vibration of azido-phenylalanine (AzF) comes at the price of relatively short vibrational lifetimes[2] and the presence of absorption lineshapes composed of a main transition and combination/overtones which arise from so-called Fermi resonances.[19] Unnatural amino acids with chemical groups that exhibit Fermi resonances exhibit spectral bands which are often not as readily interpretable by standard computational codes.[19] However, Fermi resonances are strongly dependent on intramolecular mode coupling and as such could prove very useful as sensitive probes of local equilibrium and nonequilibrium structural dynamics in proteins.[20]

We have recently reported a combined crystallographic and spectroscopic study of calmodulin in complexes with different peptides which provided a structural basis for the linear spectroscopy of the azido stretching band of protein-incorporated AzF.[21] The incorporation of AzF aims at sensing conformational differences for the chosen CaM−peptide complexes by vibrational spectroscopy of the azido group. The ubiquitous and highly conserved protein calmodulin
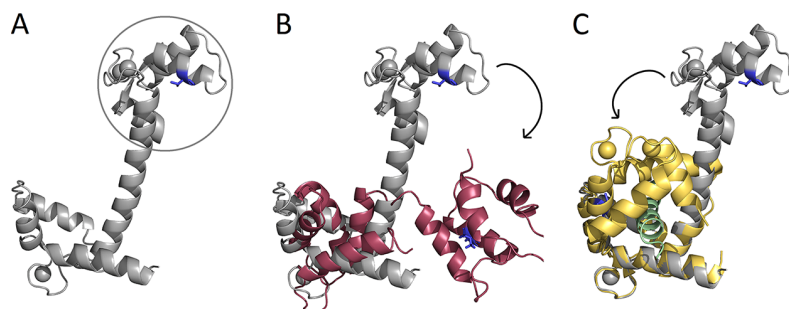
Figure 1. Structures of CaM from (A) crystallography[27] (gray) and (B) NMR spectroscopy[26] (red). (C) Crystal structure of CaM (yellow) in the complex with peptide P1 (green). The crystal structure of CaM in panel A has been superimposed with the structures in panel B and C for comparison. Clearly, only the crystal structure suggests an α-helix as a rigid connection between the two globular domains. Ambient solution-phase structures reveal two globular domains connected by a floppy backbone, facilitating peptide binding by the two globular domains that embrace the peptide. Val 108, which has been exchanged to AzF in this study, is shown in blue in all panels.

(CaM) acts as a Ca^{2+} sensor that translates the Ca^{2+} signal into a cellular response.[22] Calmodulin adopts a bilobed structure containing two globular Ca^{2+}-binding domains (each containing two EF-hands) connected by a flexible linker (Figure 1). Upon Ca^{2+} binding, Ca^{2+}/CaM recognizes and binds different target proteins with high affinity. Binding to its target protein usually results in a large conformational change with both CaM domains wrapping around a target helix[22−25] as illustrated in Figure 1C.

Several structures of CaM−peptide complexes have already been determined by X-ray crystallography[1] and NMR,[26] but these methods, while powerful in themselves, have limitations such as the need for crystal formation in protein crystallography or inherently limited time-resolution of NMR spectroscopy set by the carrier frequency of about 1 GHz. The structure of strongly fluctuating moieties or regions may not be accessible by these methods because short-lived conformations are averaged out over the period of the carrier frequencies.

CaM binding to target proteins is mimicked by use of selected CaM-binding peptides that possess different binding modes with different spacings between the hydrophobic anchor residues.[25] Peptide P1 is derived from smooth muscle myosin light chain kinase with a 1-14 spacing of the hydrophobic anchor residues and peptide P2 is derived from calmodulin-dependent protein chain kinase IIα and shows a 1-10 spacing in the CaM−peptide complex structure. Peptide P4 is from the TRPM2 Ca^{2+}-channel and was chosen as previously uncharacterized test case with an expected 1-8-14-18 spacing of the hydrophobic anchor residues.

AzF incorporation into CaM leads to pronounced spectral reshaping of the azido stretching band with additional spectral changes upon formation of different protein−peptide complexes.[21] However, linear spectra are not unambiguous in their spectral composition due to the possibility of structural heterogeneity and the presence of Fermi resonances. To further exploit the capabilities of the AzF sensor, we explore the dynamic response of the azido stretching vibration for free and protein-incorporated AzF (CaM and CaM in complex with three peptides) with femtosecond infrared spectroscopy. We model the dynamic evolution of the vibrationally excited AzF sensor by coherent oscillations that we attribute to Fermi resonances. Our approach provides a quantitative description of the vibrational dynamics, and we thereby suggest a link of the population dynamics to the AzF absorption line shapes that we consider the most physically sound description.

METHODS

Materials. All chemicals were of analytical grade and obtained from Roth (Karlsruhe, Germany) or Sigma-Aldrich (St. Louis, MO, U.S.A.), unless otherwise stated. AzF was purchased from Bachem (Switzerland). Peptides were purchased from GL Biochem (Shanghai, China). Peptide identity was confirmed by LC-MS.

Expression and Purification of CaM108AzF Complexes. We incorporated the unnatural amino acid via a modified version of the procedure reported by Young et al.[28] which employs Amber stop codon suppression technology to genetically incorporate unnatural amino acids in defined positions.[29] Different UAAs have been incorporated as biophysical probes in this way, providing control about the exact labeling position.[3,7,30−35] An amber stop codon was introduced into the CaM sequence at position 108 via QuikChange site-directed mutagenesis. The CaM sequence was cloned into a modified pET28a vector. It contains a C3 precision side, a C-terminal His$_6$ tag and a kanamycin resistance. The modified pET28aCaMC3His plasmid and the plasmid pEVOL-AzF (a gift by Peter Schultz: Addgene plasmid #31186) were cotransformed via electroporation into the *E. coli* strain BL21 Gold. The plasmid pEVOL-AzF encodes for the evolved tRNA and tRNA-synthetase from *Methanococcus jannaschii* that is specific for AzF. The plasmid contains a chloramphenicol resistance and an arabinose promoter. The overexpression was performed at 37 °C in terrific broth media, supplemented with 25 μg/mL kanamycin and 34 μg/mL chloramphenicol. At OD_{600} = 1, 1 mM p-azido-phenylalanine, 1 mM tryptophan, 1 mM tyrosine, and 0.02% arabinose were added. The expression was additionally induced by 1 mM IPTG after 45 min. The cells were harvested after 4 h and frozen at −20 °C.

For protein purification, the cell pellet was resuspended in TrisHCl-NaCl-$CaCl_2$ (25/150/5 mM) buffer, pH 7.4, and 1 μg/mL DNase I and 1 mM $MgCl_2$ were added. The cells were lysed using an Avestin EmulsionFlex-C3 high-pressure homogenizer. The cell lysate was cleared by centrifugation and the supernatant was purified via IMAC. A Ni-NTA column was equilibrated with TrisHCl−NaCl−$CaCl_2$ (25/150/5 mM) buffer, pH 7.4. For the wash 15 mM imidazole and for the elution 250 mM imidazole were added to the equilibration buffer. The elution fractions were dialyzed overnight at 4 °C. The purification was evaluated by SDS-PAGE (15%). The protein was concentrated using an Amicon Ultra-4, 10 kDa MWCO concentrator. A 1.1 molar excess of peptide was added

45

to the protein solution for the complex formation. Peptide identities and sequences can be found in Table 1.

Table 1. Used Peptides with Identities and Sequences[a]

Peptide	PDB code	Sequence
P1	1QS7	R R K W Q K T G H A V R A I G R L S S S
P2	1CDM	L K K F N A R R K L K G A I L T T M L A T R N F S
P4	no PDB structure	R I V E W T K K I Q D I V R R R Q L L T V F R E G K

[a]Anchor residues are highlighted in red.

An additional purification step via SEC (Superdex 75 10/300GL) was performed and evaluated by SDS-PAGE. The protein sample concentrations used in the experiments can be found in Table 2.

Table 2. Sample Concentrations

protein (+ peptide complex)	concentration
CaMAzF	11 mM ($\pm$2 mM)
CaMAzF+P1	15 mM ($\pm$0.2 mM)
CaMAzF+P2	8 mM ($\pm$2 mM)
CaMAzF+P4	7 mM ($\pm$0.2 mM)
free AzF	20 mM ($\pm$0.1 mM)

Pump–Probe Spectroscopy. A Ti/Sa regenerative amplifier (Spectra Physics Spitfire Ace: 800 nm, 3 kHz, 90 fs) was used to pump a home-built optical parametric amplifier[36] at a pulse energy of 150 μJ. This yielded 1.6 μJ, 115 fs (fwhm) pulses at 2090 cm^{-1} (4.78 μm) with a spectral width of 300 cm^{-1} (fwhm). The probe and reference beams were generated from the Fresnel reflex of a CaF$_2$ wedge where the reference beam was used to normalize pulse-to-pulse intensity fluctuations in the pump–probe signal. Pump, probe, and reference beams were focused down to a spot size of 120 μm (fwhm) at the sample position. The sample was circulated in a closed-cycle liquid circuit containing a flow cell (Harrick Scientific) with two 1 mm thick IR grade CaF$_2$ windows held 25 μm apart by halfmoon-shaped PTFE spacers forming a 2 mm wide channel. PFA tubing (1 mm ID) and Tygon tubing inserts were used as reservoir and sample circulation was effected with a peristaltic pump (LKB BROMMA, 2232 Microperpex S) to avoid sample degradation.

Transient absorption spectra were recorded using an imaging spectrometer (Horiba Triax 180) and a 2 × 32 MCT Pixel array (Infrared Systems). Reference measurements of aqueous buffer without protein sample were performed

immediately before or after sample measurements using the same sample cell and liquid circuit.

Data Processing. By subtraction of reference data obtained from buffer solution without protein sample, the response of the sample could be isolated (c.f. Figure 2). This procedure worked for two reasons: (i) Stable setup conditions ensured cross-phase modulation and long-lived transient absorbance changes of the solvent to be quantitively comparable between buffer and protein-buffer solutions. (ii) Absorption of the protein's azide group was weak (<3%) compared to the solvent absorption so that cross-phase modulation and solvent heating signals were essentially unaltered.

To improve statistics of the transient dynamics, a heuristic line-shape model consisting of a superposition of a Gaussian with positive amplitude and a skewed Gaussian with negative amplitude was used to spectrally model the data. The amplitude of this line shape was then used to track the decay dynamics of the UAA at an improved signal-to-noise ratio when compared to the time trace of a single detector element. First, a global fit for all data points ranging from 100 to 500 fs was used to determine the best approximation to the line shape. All parameters, except for a signal amplitude and baseline correction, were then fixed and the fit was repeated for all data points at positive time delays. This procedure restricted spectral changes to an amplitude change as a function of time delay but we found very good agreement between the data and this restricted spectral model (c.f. Supporting Information), which indicates minimal spectral reshaping within the vibrational lifetime and thereby justifies our approach.

■ RESULTS AND DISCUSSION

We compared different crystal structures of CaM in complex with various peptides at the Protein Data Bank (PDB) and decided on the incorporation of the unnatural amino acid AzF at position Val108 because the orientation and therefore the influence of the surrounding environment of the amino acid at this position is conformation-dependent.

Figure 1A shows the crystallographic holo structure of CaM/Ca^{2+} (PDB: 1CLL). The rigid linker helix between the two globular domains is likely due to the crystal structure stabilizing the protein structure in this particular conformation. Different analyses show a pronounced flexibility in the linker region.[26] The NMR structure (PDB: 1DMO) reports 30 possible conformations of CaM in its apo structure, emphasizing that the linker part of the protein backbone is highly flexible. One of the NMR structures of CaM is depicted in Figure 1B as dark red, overlaid with the crystal structure of CaM from Figure 1A for better comparison. The crystal
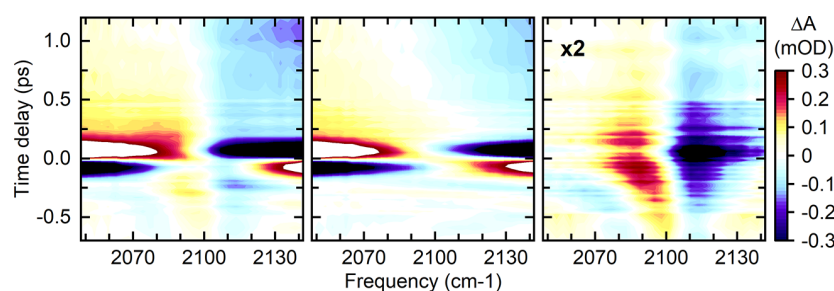

Figure 2. Transient absorption changes of azido stretching vibration of AzF108 in CaM in aqueous buffer before (left) and after (right) solvent signal (center) subtraction. Cross-phase modulation reveals negligible chirp and a time-resolution of ≤150 fs.

46

structure of CaM in the complex with a peptide (PDB: 1QS7) is shown in Figure 1C with the two globular CaM domains (yellow) embracing the bound peptide (green). Clearly, a linker helix is absent, which is further evidence that the linker assumes a rigid helical conformation only in the presence of crystal contacts.

Transient Spectra of AzF. We first discuss the transient spectra of the azido stretching vibration of AzF when dissolved in aqueous buffer as well as incorporated in CaM and three different CaM–peptide complexes. Labeling of the samples is consistent with our previous study[21] (note that the sample CaM+P3 of our previous study was not stable enough for this study). The left column of Figure 3 shows the differential
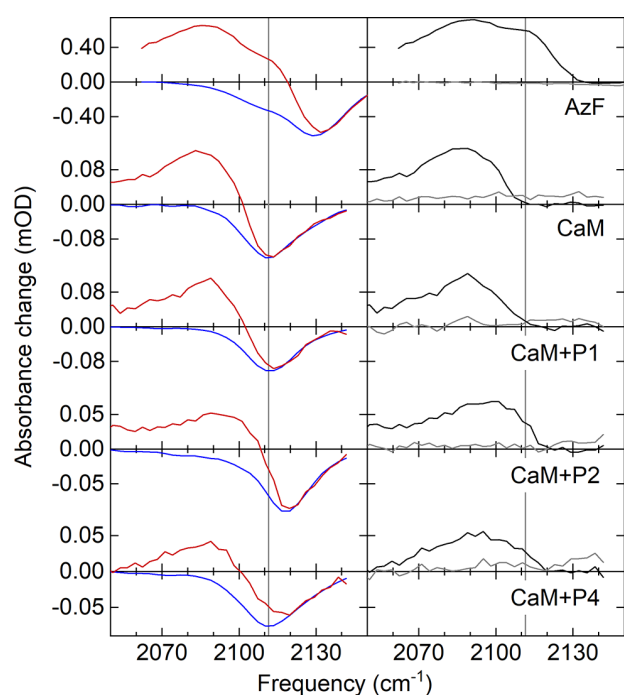

Figure 3. Left: Transient spectra of the azido stretching vibration at a pump−probe delay of 300 fs (red) and scaled negative FTIR spectra of the respective species (blue). Right: Extracted induced absorption spectra at 300 fs delay (black) and transient spectra at a pump−probe delay of 15 ps (gray).

absorption spectra (red) of all five samples at a time-delay of 300 fs. All spectra have been corrected for dynamic solvent contributions by subtracting the pure solvent response. Solvent contributions, which we attribute to the transient signal of the water combination-band grow in with increasing time delay (see Supporting Information). Subsequently, systematic errors due to background correction also increase at longer time delays. Thus, the transient spectra at 15 ps, where the signal of the UAA has decayed entirely, can be regarded as upper limits for systematic errors due to background correction. These are also shown as gray lines in the right column of Figure 3.

Inverted linear absorption spectra (blue) of the respective complexes have also been plotted in the left column of Figure 3. We scaled these spectra to the spectral region above the minimum of the transient absorbance change to estimate the bleach and stimulated emission signals of the underlying $0 \rightarrow 1$ transitions. The difference of pump−probe (red) and inverted static (blue) spectra can then be regarded as an estimate of the excited state absorption spectrum (black) as plotted in the

right column of Figure 3 of each sample. Our extraction of the induced absorption spectra might have over- or under-estimated the excited absorption lineshapes as our choice of scaling the linear absorption in the subtraction process is reasonable but somewhat arbitrary.

When comparing the differential absorption spectra (red) of the five samples, it is apparent that the pump−probe spectra of the protein samples are similar while free AzF exhibits a spectrum that is shifted to lower frequency (top left panel). The same spectral behavior can be consistently observed for the $0 \rightarrow 1$ transitions (blue) and hence, for the extracted $1 \rightarrow 2$ transitions (black)- The latter appears to be broader than the static spectrum for all samples. In addition to increased amplification of frequency fluctuations of $1 \rightarrow 2$ transitions in anharmonic oscillators, coupling and subsequent splitting of the energetically higher-lying states could contribute to the broader $1 \rightarrow 2$ absorption spectra, as was often observed in systems with Fermi resonances such as acetaniline.[37] The vertical gray line on the left side of Figure 3 indicates the absorption maximum of the azido stretching vibration in CaM. The complex CaM+P4 shows no apparent shift compared to free CaM, while binding of peptide P1 induces a slight blue-shift and complexation of P2 produces a blue-shift by ~6 cm^{-1}. The absorption maximum of free AzF is shifted to higher frequency by ~17 cm^{-1}. The blue-shift of the ν_{N3} band in the CaM+P2 complex could be mistaken as AzF in this complex being more solvent exposed (via an anomalous shift due to hydrogen bonding to solvent molecules[38−41]) but our previous study clarified that hydrogen bonding to carbonyl groups of neighboring residues is the probable cause for this shift.

The zero crossings of the differential absorption spectra and the onset of the extracted excited state absorption show the same spectral shifts as the linear spectra. This finding suggests a similar anharmonicity (~25 cm^{-1}) of the azido stretching vibration in all five samples. CaM+P4 might be an exception but this sample also yielded the smallest signal-to-noise ratio. Overall, we conclude that the anharmonicity of the azido stretching vibration is not substantially modified by complex-ation of peptides. AzF in aqueous buffer shows the broadest azido stretching spectrum of all samples for both the ground-state and the excited state transitions. We attribute this observation to two broadening mechanisms, (i) solvent fluctuations, that is, mainly water with its broad distribution of frequencies, and (ii) the particular distribution of Fermi resonances,[19] which is markedly different from the incorpo-rated UAA.[21] Spectral shape evolution cannot be observed within our signal-to-noise ratio.

Population Dynamics of Free Aqueous AzF. Next, we discuss the temporal evolution of the azido stretching excitation. The top left panel of Figure 4 shows the decay dynamics of the isolated UAA in aqueous solution. These population dynamics feature a rapid initial decay within the first hundreds of femtoseconds, followed by a slower component in the picosecond range. Intuitively, the temporal evolution appears to be a biexponential decay. However, residual analysis of a biexponential fit reveals systematic deviation between model and experimental data (see Figure S9). We therefore propose an alternative picture based on a recent two-dimensional infrared (2DIR) spectroscopy study of free AzF[19] in aqueous and isopropanol solution, which reported coupled transitions within the AzF azido stretching band due to Fermi resonances. A Fermi resonance couples a dipole-allowed bright transition and a dipole-forbidden dark
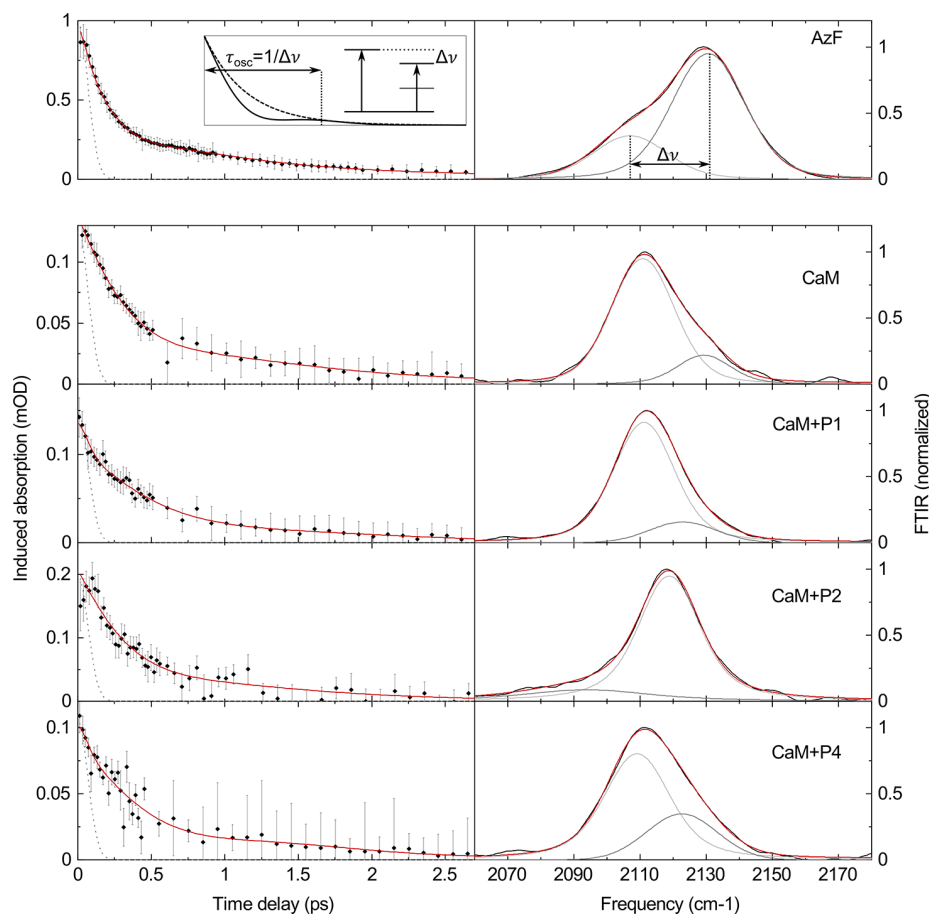
47

Figure 4. Left: Temporal evolution of the amplitude of the azido stretching response in the different conformers (black). A fit consisting of an exponential and a damped cosine function was used to model the data (red) Also included in the model is a Gaussian instrument response function centered at *t* = 0 with a fwhm of 160 fs (gray, dotted line). This is to account for possible nonresonant contributions during pulse overlap. The instrument response is shown as a gray dashed line. Right: Linear spectra of the respective conformers (black) and fits of two Voigt profiles (gray) and their sum (red).

Table 3. Fit Parameters of the Decay Model Shown in the Left-Hand Side of Figure 4^a

	τ_{pop} (fs)	τ_{coh} (fs)	τ_{osc} (fs)	$1/\tau_{osc}$ (cm^{-1})	$\Delta\nu_{12}$ (cm^{-1})	A_{gauss} (mOD)	A_{osc} (mOD)	A_{pop} (mOD)
AzF	844 ± 29	215 ± 21	1393 ± 75	23.9 ± 1.3	23.6 ± 3.0	0.08 ± 0.05	0.44 ± 0.07	0.44 ± 0.02
CaM	1007 ± 130	304 ± 69	1988 ± 480	16.8 ± 4.1	18.4 ± 1.6	0.00 ± 0.01	0.06 ± 0.03	0.07 ± 0.01
CaM+P1	941 ± 230	532 ± 250	2518 ± 1200	13.2 ± 6.4	11.7 ± 6.2	0.03 ± 0.01	0.03 ± 0.02	0.08 ± 0.03
CaM+P2	865 ± 330	299 ± 200	2072 ± 1700	16.1 ± 13.3	24.9 ± 11.1	0.00 ± 0.05	0.10 ± 0.15	0.11 ± 0.06
CaM+P4	906 ± 290	534 ± 510	1867 ± 980	17.9 ± 9.4	13.5 ± 3.6	0.02 ± 0.01	0.03 ± 0.04	0.06 ± 0.02

$^a\tau_{pop}$, τ_{coh}, and τ_{osc} are the population time, the coherence time, and oscillation period of the damped cosine contribution. $\Delta\nu_{12}$ is the spacing between the two Voigt profiles fit to the linear spectra on the right of Figure 4. A_{gauss}, A_{osc}, and A_{pop} are the amplitudes of the Gaussian component, the oscillatory feature, and the population decay.

combination/overtone which are close in frequency. The dark mode gains oscillator strength in this coupling scheme. Indeed, the asymmetric line shape of the linear spectrum of aqueous AzF can be well described by a superposition of two Voigt profiles, as shown on the top right panel of Figure 4. The coherent excitation of these two transitions leads to a low-frequency quantum beat that manisfests in a periodic modulation of the pump–probe response at the difference frequency of the coupled transitions (as observed in several other systems exhibiting Fermi resonances).[12,19,20,42−44]

We have illustrated this mode coupling in the inset of Figure 4 (top panels). Taking one apparent Fermi resonance into account, we employ the following model for the population decay of free aqueous AzF

$$S(t) = A_{gauss} \cdot e^{-4\ln(2)\left(\frac{t}{fwhm}\right)^2} + A_{osc} \cdot \cos\left(2\pi\frac{t}{\tau_{osc}}\right) \cdot e^{-t/\tau_{coh}} + A_{pop} \cdot e^{-t/\tau_{pop}}$$

where the singal is a sum of a damped harmonic oscillation and an exponential decay. Additional signals due to nonresonant effects during temporal overlap of pump and probe pulses are accounted for by a Gaussian centered at 0 fs with a fwhm of 160 fs as extracted from the solvent response (c.f. Supporting Information). The cosine term reflects the quantum beat due to the coherent excitations of the two transitions that are in

48

Fermi resonance. The oscillation period corresponds to the inverse of the transitions' frequency spacing $\Delta\nu_{12} = 1/\tau_{ose}$.

The fit to the population decay of free aqueous AzF is shown in the top left panel of Figure 4, and the parameters are summarized in Table 3. This model assigns a population lifetime of about 0.8 ps to the azido stretching excitation in free aqueous AzF while the rapid signal decay on sub-500 fs time scales is due to the loss of coherence of a strongly overdamped quantum beat. This time-domain picture is fully consistent with the respective linear absorption spectrum of free aqueous AzF in the top tight panel of Figure 4. The frequency spacing $\Delta\nu_{12}$ between the two fit Voigt profiles matches the inverse quantum beat period very well, $\Delta\nu_{12} = 1/\tau_{osc}$, as can be seen in Table 3.

In the Fermi resonance model, free aqueous AzF exhibits a quantum beat coherence time of only 219 fs. This time constant is three times shorter than the one reported for free AzF in isopropanol,[19] a value that reflects the much broader line shape of the ν_{N3}-band of free AzF in aqueous solution, which in turn is linked to the particular density of states of water to which the azido stretching excitation is coupled. A Gaussian dephasing model might be more suitable to describe aqueous AzF (see Figure S9). However, a clear distinction between exponential and Gaussian dephasing requires sub-10 μOD noise levels, which were unobtainable for the less stable protein (complexes). The exponetial decay model proved to be more robust for all samples. Both quantum beat models yield similar oscillation frequencies and coherence times for free aqueous AzF (see Table S4). A distinction between both models is therefore irrelevant in the following discussion.

Population Dynamics of Protein-Incorporated AzF. The linear spectra of the azido stretching band, ν_{N3}, of AzF incorporated into CaM differ from free aqueous AzF, but they also appear to be composed of a least two transitions. This begs the question whether Fermi resonances underlie the azido stretching line shape when AzF is incorporated into the protein. Fitting a biexponential decay to the ν_{N3} response yields two time constants that differ more than 5-fold (c.f. Table S1), which seems rather unphysical for a bimodal population decay due to a two subensembles with structural motifs as we do not observe significant spectral shifts of the pump−probe spectra over time. The latter fact also renders anharmonic mode coupling highly unlikely to be the origin of the biexponential ν_{N3} response. Such a mechanism would entail a ultrafast monoexponential population decay followed by an altered ground-state spectrum due to anharmonic couplig of the azido stretching band to other AzF modes that are being populated during intramoelcuar vibrational energy redistribution (IVR). We therefore consider the Fermi resonance model physically well justified, albeit, we cannot provide unambiguous proof of the Fermi resonance model due to limited the signal-to-noise ratio of the protein data.

All five sample responses are accurately described by the Fermi resonance model, and as for free aqueous AzF, we find good agreement between the time and frequency domains for all protein samples: Within the margin of error, the inverse beat period $1/\tau_{osc}$ equals the spectral difference $\Delta\nu_{12}$ (right two columns of Table 3) which is independently obtained from a fit of two Voigt profiles to the azido stretching lineshapes on the righthand side of Figure 4. The model suggests an azido stretching lifetime $\tau_{pop} \lesssim 1$ ps (second column of Table 3) that is substantially longer than the initial signal decay and varies little among the five samples. In this

model, samples are differentiated by coherence times and frequencies of the quantum beats. For instance, the CaM ν_{N3} response exhibits a more distinct initial decay compared to the long-lived population decay CaM+P1. This translates to a larger oscillation amplitude A_{osc} relative to the population amplitude A_{pop} (cf. Table 3, last two columns). Generally, the ν_{N3} response of the protein samples differs from free AzF. Most pronounced is the longer oscillation period $\tau_{osc} \approx 2$ ps in the protein samples compared to free AzF which reflects the smaller frequency spacing between the two coupled transitions in the protein spectra of AzF (Figure 4, right column). Among the protein samples, AzF in CaM exhibits a response most reminiscent of free AzF but with a distinctly different ν_{N3} spectral band. Given the rather open CaM structure with two globular domains losely connected, fluctuations and solvent accessibility around AzF could account for this oberservation.

The short coherence times compared to the oscillation periods of the quantum beats result in strongly overdamped model oscillations and correspondingly larger uncertainties of the oscillation periods. The quantum beat oscillations would correspond to an actual low-frequency wavepacket although quantum beats due to Fermi resonances result from a coherent excitation of high-frequency modes. Short coherence times are not unusual for such vibrations with sub-THz frequency in a condensed-phase environment. The fit results in Table 3 therefore constitute physcially reasonable model parameters.

We have already placed the population dynamics of azido stretching excitation in context with the analysis of linear infrared spectra of AzF in the five samples[21] (Figure 4, see SI for a complete parameter list). The stronger transitions should have predominantly asymmetric N_3 stretching character while we would designate the weaker transition as the combination/overtone that is in Fermi resonance with the N_3 stretching excitation. This weaker transition is less pronounced in the protein samples than in free aqueous AzF. Within this line shape decomposition, CaM and CaM+P1 exhibit identical parameters for the main ν_{N3} transition and can only be distinguished due the second weaker transistion which we ascribe to a Fermi resonance. This difference is also reflected in the transient ν_{N3} response of these two samples. Fermi resonances are very sensitive to coupling constants and relative frequency spacing of the coupled modes, and even insignificant line shifts can result in significant changes of relative oscillator strength between the transitions. This propety of Fermi resonances might be useful in some applications of VDLs.

■ CONCLUSIONS

Our femtosecond infrared study suggests a Fermi resonance model for protein-incorporated AzF to distinguish CaM in different binding motives. We find that the decay dynamics of the azido stretching excitations of free AzF and incorporated into CaM (also in complex with the three particular peptides) can be well described by coherent superpositions of at least two transitions that we ascribe to Fermi resonances of the UAA's asymmetric N_3 stretching mode. Within this model, we extract a lifetime of ∼1 ps for the azido stretching excitation in all samples. The Fermi resonance model introduces an exponentially damped quantum beat between the two dominant transitions which is unique to each of the five studied samples and remarkably consistent with the linear spectra of the azido stretching mode of AzF. It would of course be interesting to link atomically resolved structures from X-ray crystallography to anharmonic mode coupling models and

49

QM/MM simulations and aim at a quantitative description of Fermi resonances to relate protein structures to spectral responses. We also aim for crystallographic structures of all studied CaM−peptide to provide a structural basis for additional CaMAzF-peptide complexes with atomic resolution.

ASSOCIATED CONTENT

Supporting Information

The Supporting Information is available free of charge at https://pubs.acs.org/doi/10.1021/acs.jpcb.1c06775.

Additional information, figures, and tables (PDF)

AUTHOR INFORMATION

Corresponding Authors

Henning Tidow − *Hamburg Advanced Research Centre for Bioorganic Chemistry, Institute for Biochemistry and Molecular Biology, Department of Chemistry, University of Hamburg, D-20146 Hamburg, Germany; The Hamburg Centre for Ultrafast Imaging, University of Hamburg, D-22761 Hamburg, Germany;* orcid.org/0000-0002-4702-9332; Email: tidow@chemie.uni-hamburg.de

Nils Huse − *Hamburg Advanced Research Centre for Bioorganic Chemistry, Institute for Nanostructure and Solid-State Physics, Department of Physics, and Center for Free-Electron Laser Science, University of Hamburg, D-22761 Hamburg, Germany; The Hamburg Centre for Ultrafast Imaging, University of Hamburg, D-22761 Hamburg, Germany;* orcid.org/0000-0002-3281-7600; Email: nils.huse@uni-hamburg.de

Authors

Matthias Ruppert − *Hamburg Advanced Research Centre for Bioorganic Chemistry, Institute for Nanostructure and Solid-State Physics, Department of Physics, and Center for Free-Electron Laser Science, University of Hamburg, D-22761 Hamburg, Germany;* orcid.org/0000-0001-8100-8087

Anne Creon − *Hamburg Advanced Research Centre for Bioorganic Chemistry, Institute for Nanostructure and Solid-State Physics, Department of Physics, and Center for Free-Electron Laser Science, University of Hamburg, D-22761 Hamburg, Germany; Hamburg Advanced Research Centre for Bioorganic Chemistry, Institute for Biochemistry and Molecular Biology, Department of Chemistry, University of Hamburg, D-20146 Hamburg, Germany*

Complete contact information is available at:
https://pubs.acs.org/10.1021/acs.jpcb.1c06775

Author Contributions

||M.R. and A.C. have contributed equally to this work.

Notes

The authors declare no competing financial interest.

ACKNOWLEDGMENTS

REFERENCES

(1) Dippel, A. B.; et al. Probing the effectiveness of spectroscopic reporter unnatural amino acids: A structural study. *Acta Crystallogr. Sect. D Struct. Biol.* **2016**, *72*, 121−130.

(2) Thielges, M. C.; et al. Two-dimensional IR spectroscopy of protein dynamics using two vibrational labels: A site-specific genetically encoded unnatural amino acid and an active site ligand. *J. Phys. Chem. B* **2011**, *115*, 11294−11304.

(3) Ye, S.; et al. Tracking G-protein-coupled receptor activation using genetically encoded infrared probes. *Nature* **2010**, *464*, 1386−1389.

(4) Baiz, C. R.; et al. Vibrational Spectroscopic Map, Vibrational Spectroscopy, and Intermolecular Interaction. *Chem. Rev.* **2020**, *120*, 7152−7218.

(5) Błasiak, B.; Londergan, C. H.; Webb, L. J.; Cho, M. Vibrational Probes: From Small Molecule Solvatochromism Theory and Experiments to Applications in Complex Systems. *Acc. Chem. Res.* **2017**, *50*, 968−976.

(6) Van Wilderen, L. J. G. W.; et al. Vibrational dynamics and solvatochromism of the label SCN in various solvents and hemoglobin by time dependent IR and 2D-IR spectroscopy. *Phys. Chem. Chem. Phys.* **2014**, *16*, 19643−19653.

(7) Waegele, M. M.; Culik, R. M.; Gai, F. Site-specific spectroscopic reporters of the local electric field, hydration, structure, and dynamics of biomolecules. *J. Phys. Chem. Lett.* **2011**, *2*, 2598−2609.

(8) Zimmermann, J.; Thielges, M. C.; Seo, Y. J.; Dawson, P. E.; Romesberg, F. E. Cyano groups as probes of protein microenvironments and dynamics. *Angew. Chem., Int. Ed.* **2011**, *50*, 8333−8337.

(9) Fafarman, A. T.; Sigala, P. A.; Schwans, J. P.; Fenn, T. D.; Herschlag, D.; Boxer, S. G. Quantitative, directional measurement of electric field heterogeneity in the active site of ketosteroid isomerase. *Proc. Natl. Acad. Sci. U. S. A.* **2012**, *109*, 109.

(10) Fafarman, A. T.; Boxer, S. G. Nitrile Bonds as Infrared Probes of Electrostatics in Ribonuclease S. *J. Phys. Chem. B* **2010**, *114*, 13536−13544.

(11) Schmidt-Engler, J. M.; Zangl, R.; Guldan, P.; Morgner, N.; Bredenbeck, J. Exploring the 2D-IR repertoire of the -SCN label to study site-resolved dynamics and solvation in the calcium sensor protein calmodulin. *Phys. Chem. Chem. Phys.* **2020**, *22*, 5463−5475.

(12) Park, J. Y.; Mondal, S.; Kwon, H.-J.; Sahu, P. K.; Han, H.; Kwak, K.; Cho, M. Effect of isotope substitution on the Fermi resonance and vibrational lifetime of unnatural amino acids modified with IR probe: A 2D-IR and pump-probe study of 4-azido-L-phenyl alanine. *J. Chem. Phys.* **2020**, *153*, 153.

(13) Baumann, T.; et al. Site-Resolved Observation of Vibrational Energy Transfer Using a Genetically Encoded Ultrafast Heater. *Angew. Chem., Int. Ed.* **2019**, *58*, 2899−2903.

(14) Müller-Werkmeister, H. M.; Li, Y. L.; Lerch, E. B. W.; Bigourd, D.; Bredenbeck, J. Ultrafast hopping from band to band: Assigning infrared spectra based on vibrational energy transfer. *Angew. Chem., Int. Ed.* **2013**, *52*, 6214−6217.

(15) Leitner, D. M. Energy flow in proteins. *Annu. Rev. Phys. Chem.* **2008**, *59*, 233−259.

(16) Basom, E. J.; Maj, M.; Cho, M.; Thielges, M. C. Site-Specific Characterization of Cytochrome P450cam Conformations by Infrared Spectroscopy. *Anal. Chem.* **2016**, *88*, 6598−6606.

(17) Kim, H.; Cho, M. Infrared probes for studying the structure and dynamics of biomolecules. *Chem. Rev.* **2013**, *113*, 5817−5847.

(18) Adhikary, R.; Zimmermann, J.; Romesberg, F. E. Transparent Window Vibrational Probes for the Characterization of Proteins with High Structural and Temporal Resolution. *Chem. Rev.* **2017**, *117*, 1927−1969.

(19) Zhang, J.; et al. Identifying and Modulating Accidental Fermi Resonance: 2D IR and DFT Study of 4-Azido-l-phenylalanine. *J. Phys. Chem. B* **2018**, *122*, 8122−8133.

(20) Rodgers, J. M.; et al. Fermi resonance as a means to determine the hydrogen-bonding status of two infrared probes. *Phys. Chem. Chem. Phys.* **2017**, *19*, 16144−16150.

(21) Creon, A.; Josts, I.; Niebling, S.; Huse, N.; Tidow, H. Conformation-specific detection of calmodulin binding using the unnatural amino acid p-azido-phenylalanine (AzF) as an IR-sensor. *Struct. Dyn.* **2018**, *5*, 064701.

(22) Crivici, A.; Ikura, M. Molecular and structural basis of target recognition by calmodulin. *Annu. Rev. Biophys. Biomol. Struct.* **1995**, *24*, 85−116.

(23) Vetter, S. W.; Leclerc, E. Novel aspects of calmodulin target recognition and activation. *Eur. J. Biochem.* **2003**, *270*, 404−414.

(24) Yap, K. L.; Ames, J. B.; Swindells, M. B.; Ikura, M. Diversity of conformational states and changes within the EF-hand protein superfamily. *Proteins: Struct., Funct., Genet.* **1999**, *37*, 499−507.

(25) Tidow, H.; Nissen, P. Structural diversity of calmodulin binding to its target sites. *FEBS J.* **2013**, *280*, 5551−5565.

(26) Zhang, M.; Tanaka, T.; Ikura, M. Calcium-induced conformational transition revealed by the solution structure of apo calmodulin. *Nat. Struct. Mol. Biol.* **1995**, *2*, 758−767.

(27) Chattopadhyaya, R.; Meador, W. E.; Means, A. R.; Quiocho, F. A. Calmodulin structure refined at 1.7 Å resolution. *J. Mol. Biol.* **1992**, *228*, 1177−1192.

(28) Young, T. S.; Ahmad, I.; Yin, J. A.; Schultz, P. G. An Enhanced System for Unnatural Amino Acid Mutagenesis in E. coli. *J. Mol. Biol.* **2010**, *395*, 361−374.

(29) Wang, L.; Xie, J.; Schultz, P. G. Expanding the genetic code. *Annu. Rev. Biophys. Biomol. Struct.* **2006**, *35*, 225−249.

(30) Castanheiro, T.; Suffert, J.; Donnard, M.; Gulea, M. Recent advances in the chemistry of organic thiocyanates. *Chem. Soc. Rev.* **2016**, *45*, 494−505.

(31) Johnson, M. N. R.; Londergan, C. H.; Charkoudian, L. K. Probing the Phosphopantetheine Arm Conformations of Acyl Carrier Proteins Using Vibrational Spectroscopy. *J. Am. Chem. Soc.* **2014**, *136*, 11240−11243.

(32) Kim, C. H.; Axup, J. Y.; Schultz, P. G. Protein conjugation with genetically encoded unnatural amino acids. *Curr. Opin. Chem. Biol.* **2013**, *17*, 412−419.

(33) Liu, C. C.; Schultz, P. G. Adding New Chemistries to the Genetic Code. *Annu. Rev. Biochem.* **2010**, *79*, 413−444.

(34) Schultz, K. C.; et al. A genetically encoded infrared probe. *J. Am. Chem. Soc.* **2006**, *128*, 13984−13985.

(35) Ye, S.; Huber, T.; Vogel, R.; Sakmar, T. P. FTIR analysis of GPCR activation using azido probes. *Nat. Chem. Biol.* **2009**, *5*, 397−399.

(36) Kaindl, R. A.; et al. Generation, shaping, and characterization of intense femtosecond pulses tunable from 3 to 20 *μ*m. *J. Opt. Soc. Am. B* **2000**, *17*, 2086.

(37) Edler, J.; Hamm, P. Two-dimensional vibrational spectroscopy of the amide I band of crystalline acetanilide: Fermi resonance, conformational substates, or vibrational self-trapping? *J. Chem. Phys.* **2003**, *119*, 2709−2715.

(38) Chaban, G. M. Anharmonic vibrational spectroscopy of nitriles and their complexes with water. *J. Phys. Chem. A* **2004**, *108*, 4551−4556.

(39) Owrutsky, J. C.; Pomfret, M. B.; Barton, D. J.; Kidwell, D. A. Fourier transform infrared spectroscopy of azide and cyanate ion pairs in AOT reverse micelles. *J. Chem. Phys.* **2008**, *129*, 024513.

(40) Hobza, P.; Havlas, Z. Blue-Shifting Hydrogen Bonds. *Chem. Rev.* **2000**, *100*, 4253.

(41) Hussain, A.; Huse, N.; Vendrell, O. Sensitivity of core-level spectroscopy to electrostatic environments of nitrile groups: An ab initio study. *Struct. Dyn.* **2017**, *4*, 054102.

(42) Kwon, Y. A.; Lee, C.; Park, S. Effect of ion−molecule interaction on fermi-resonance in acetonitrile studied by ultrafast vibrational spectroscopy. *Chem. Phys.* **2014**, *445*, 38−45.

(43) Gündoğdu, K.; Bandaria, J.; Nydegger, M.; Rock, W.; Cheatum, C. M. Relaxation and anharmonic couplings of the O-H stretching

vibration of asymmetric strongly hydrogen-bonded complexes. *J. Chem. Phys.* **2007**, *127*, 044501.

(44) Park, J. Y.; et al. Two-dimensional IR spectroscopy reveals a hidden Fermi resonance band in the azido stretch spectrum of *β*-azidoalanine. *Phys. Chem. Chem. Phys.* **2020**, *22*, 19223‾19229.

51

5 Conclusion and outlook

In this work, low frequency excitations and their interactions with other degrees of freedom have been investigated in MIR HgTe quantum dots and p-azido phenylalanine (AzF) in different conformations of the protein Calmodulin using nonlinear infrared spectroscopic methods. Through this, it was possible to uncover and describe the ultrafast intraband dynamics in HgTe quantum dots, which are crucial for the further development of infrared devices based on tailored, i.e. hetero-structured quantum dots and the understanding of physics in reduced dimensions. Furthermore, two-dimensional infrared spectroscopy was demonstrated to lift the spectral inhomogeneity due to size distribution in MIR HgTe quantum dots, which will allow a detailed description of the interaction between low-frequency modes on a fine-structure level in future experiments. The measurements on the azido stretching vibration in AzF revealed a uniform relaxation behavior for all investigated protein peptide complexes. The differences of the relaxation of the azido stretching vibration in between different conformation manifest as changes in a sub 500 femtosecond feature, which was assigned as quantum beat originating from coherent superposition of two states in Fermi resonance. The correlation of this quantum beat and the linear spectra of the vibrational dynamic label (VDL) AzF allowed for the disentanglement of the linear spectrum and, by this a better understanding of the interaction of the VDL and its surroundings. A more detailed summary of these results as well as their consequences and resulting future capabilities is given in the following section.

Intraband dynamics in MIR HgTe quantum dots

Timescales for intraband cooling in MIR HgTe quantum dots were obtained by observing the population at the band-gap as a function of time after non-resonant photo-excitation for different photon energies.This revealed rapid exciton relaxation to the band-gap within less than 2.5 ps, even in the multi-exciton generation (MEG) regime at photon energies of 3.1 eV, which is close to the work function of bulk HgTe. No evidence of bottlenecks of any sort was found for intraband cooling. On the contrary, a uniform rate of $0.36\,\mathrm{eV\cdot ps^{-1}}$ was found for the energy dissipation from the electronic system into an unidentified bath. This rate is identical to the energy dissipation rate for the $2S_h \rightarrow 1S_h$ transition in the valence band. This implies, that cooling of electronic excitations is either independent from the density of states, or, more likely, dominated by hole cooling in the valence band. This was interpreted in the framework of Auger cooling, where electrons in the conduction band relax by transferring energy to holes via electron-hole scattering processes, as discussed in

section 3.2. This assumption was further supported by much slower relaxation times that had been found in similar systems, where Auger scattering between electrons and holes had been suppressed [16, 17, 123]. These findings, including the energy loss rate, are over-all consistent with observations of similar processes in CdSe quantum dots [21, 23]. This indication of Auger cooling suggests that intraband cooling in HgTe quantum dots could be drastically slowed down by decoupling electrons and holes by using hetero-structured core-shell quantum dots, like demonstrated in CdSe/ZnS/ZnSe quantum dots [16]. The consequences of which could be enormous for solar energy harnessing, as it may allow for efficient extraction of hot carriers, which is especially appealing for narrow gap materials, such as HgTe. Interestingly, the energy dissipation rate also remains unchanged if several electron holes pairs are excited within a single quantum dot. This means that either a single electron or hole can dissipate heat at a given time, or more likely, a fundamental bottleneck for energy dissipation into the bath limits intraband cooling, which could also explain the constant energy dissipation rate. This cannot be understood using present models and will have to be addressed using future experiments and theoretical calculations. Future fundamental approaches towards understanding the intraband cooling mechanism in HgTe quantum dots could address the influence of ligands and particle size. Here, it would be interesting if and how much the cooling dynamics are affected by Ligand exchange and if a universal trend in observed timescales can be found for the scaling of particle size. Here, a speed up for smaller processes would be expected for Auger processes as a result of relaxed momentum conservation and enhanced Coulomb interaction due to stronger carrier confinement. Of course, also infrared pump THz probe spectroscopy would offer many opportunities for future mechanistic insights by providing direct observation of state to state transition rates.

2D spectroscopy of HgTe quantum dots

Two-dimensional infrared spectroscopy was experimentally implemented based on an existing design by Nils Huse and Amul Shinde and used to investigate the lowest excitonic state in HgTe quantum dots. Preliminary results for the respective correlation maps have been presented and carefully interpreted. They show significant static inhomogeneous broadening in the sample, which is attributed to the size distribution of the particles, which was be lifted through 2D spectroscopy. Two diagonal features were found close to the band-gap that can also be observed in the FTIR spectrum. From cross-peak analysis they appear to share a common state in the valence band. Yet, the absence of energy transfer even after a waiting time of $100\,\mathrm{ps}$ makes the assignment of the energetically lower transition as a mid-gap state more likely, since excitonic states should rapidly decay to the band-gap, as discussed in the sections 3.2 and 3.4. These 2d correlation maps also indicate the presence of another gap-state at $4730\,\mathrm{cm}^{-1}$, which is not accessible in the FTIR spectrum, due to an overlapping strong solvent or ligand combination band. Additionally, indications for direct observation for energy transfer from the electronic system to said combination band were found. This first measurement of 2d correlation maps in HgTe Qds set the basis for future, more systematic measurements. A complete

sampling of the waiting time will give rise to the time scales of the individual peaks and uncover potentially hidden oscillatory features originating from coherences in the system. In context of the intraband relaxation measurements presented above, 2D spectroscopy presents a direct improvement over conventional pump-probe spectroscopy, as it allows to directly observe the energy transfer between any pair of excitonic states as off-diagonal features. This removes the ambiguity of intermediate steps in the relaxation process from the measurement, providing a better grasp of the relaxation mechanisms at play. Additionally, the role of ligands in (intraband) carrier relaxation could be unveiled by the investigation of off-diagonal features between excitons and ligand modes. This would be especially interesting for MIR quantum dots, where the band gap, or intraband transitions can easily brought in resonance with ligand modes e.g. the C-H stretching vibration of the dodecanethiol ligands at around $2900\,cm^{-1}$. Furthermore, the lifted inhomogeneous broadening might allow to directly measure the bi-exciton binding energy and bi-exciton recombination, allowing to test theoretical models.

AzF as a vibrational dynamic label for protein spectroscopy

Aside the work on HgTe nanoparticles, the dynamic response of the azido stretching mode of the vibrational label p-azidophenylalanine was investigated using MIR pump-probe spectroscopy. Here, the Ca^{2+} sensitive second messenger protein Calmodulin and Calmodulin-peptide complexes in aqueous solution were used as a model system to study the interaction between the VDL and its surroundings. AzF had already been thoroughly studied using isopropanol as a solvent [42]. Here, the vibrational relaxation showed distinct oscillatory features due to a coherent superposition of two states in Fermi resonance. In aqueous buffer solution, the same effect could be observed, although the feature was significantly less pronounced due to much shorter coherence times when compared to AzF in isopropanol. This feature could therefore easily be mistaken for a bi-exponential relaxation. Azido stretching vibration relaxation times were found around 1 ps independent of the conformational state of the protein in the Calmodulin complex samples. This suggests chemically similar environments in all conformations, which also reflects in very similar linear spectra that had been found for these complexes [7]. The main difference in between the complexes manifests in a sub 500 femtosecond feature that was interpreted as a strongly overdamped quantum beat as found in aqueous AzF. This was further supported by good agreement between quantum beat frequency and FTIR spectra. This duality between beat frequency and linear spectra clarified that the complex line-shape of AzF in Calmodulin complexes does not originate from a bi-modal distribution of chemical environments.

The rapid vibrational relaxation restricts the time window for observation of changes in the surroundings of AzF to roughly 1 picosecond, which is too short for most, if not all relevant protein motions and therefore limits the use of AzF as a VDL for future use in two-dimensional spectroscopy. However, the uniform behavior of the vibrational relaxation and the dephasing times of the quantum beat clarified that minuscule changes in the immediate surroundings of the vibrational label may still result in traceable differences

in the linear spectrum. This was be explained by considering the larger parameter-space that becomes accessible through the Fermi resonance, due to its high sensitivity to shifts in energy and molecular couplings. In combination with future advances in the theoretical description of AzF, this might motivate niche applications for FTIR spectroscopy and photo-active proteins, where the accessible time window is not limited by the vibrational lifetime [8].

Bibliography

[1] Pratul K. Agarwal. Enzymes: An integrated view of structure, dynamics and function. *Microbial Cell Factories*, 5:1–12, 2006.

[2] William Shockley and Hans J. Queisser. Detailed balance limit of efficiency of p-n junction solar cells. *Journal of Applied Physics*, 32(3):510–519, 1961.

[3] N. Orlowski, J. Augustin, and Z. Gołacki. Direct evidence for the inverted band structure of HgTe. *Physical Review B - Condensed Matter and Materials Physics*, 61(8):R5058–R5061, 2000.

[4] Sean E. Keuleyan, Philippe Guyot-sionnest, Christophe Delerue, and Guy Allan. Mercury telluride colloidal quantum dots: Electronic structure, size-dependent spectra, and photocurrent detection up to 12 μm. *ACS Nano*, 8(8):8676–8682, 2014.

[5] Nicolas Goubet, Amardeep Jagtap, Clément Livache, Bertille Martinez, Hervé Portalès, Xiang Zhen Xu, Ricardo P.S.M. Lobo, Benoit Dubertret, and Emmanuel Lhuillier. Terahertz HgTe Nanocrystals: Beyond Confinement. *Journal of the American Chemical Society*, 140(15):5033–5036, 2018.

[6] Megan C. Thielges, Jun Y. Axup, Daryl Wong, Hyun Soo Lee, Jean K. Chung, Peter G. Schultz, and Michael D. Fayer. Two-dimensional IR spectroscopy of protein dynamics using two vibrational labels: A site-specific genetically encoded unnatural amino acid and an active site ligand. *Journal of Physical Chemistry B*, 115(38):11294–11304, 2011.

[7] Anne Creon, Inokentijs Josts, Stephan Niebling, Nils Huse, and Henning Tidow. Conformation-specific detection of calmodulin binding using the unnatural amino acid p-azido-phenylalanine (AzF) as an IR-sensor. *Structural Dynamics*, 5(6), 2018.

[8] Christopher R. Hall, Jinnette Tolentino Collado, James N. Iuliano, Agnieszka A. Gil, Katrin Adamczyk, Andras Lukacs, Gregory M. Greetham, Igor Sazanovich, Peter J. Tonge, and Stephen R. Meech. Site-Specific Protein Dynamics Probed by Ultrafast Infrared Spectroscopy of a Noncanonical Amino Acid. *Journal of Physical Chemistry B*, 123(45):9592–9597, 2019.

[9] Robert T. Ross and Arthur J. Nozik. Efficiency of hot-carrier solar energy converters. *Journal of Applied Physics*, 53(5):3813–3818, 1982.

[10] Mingjie Li, Saikat Bhaumik, Teck Wee Goh, Muduli Subas Kumar, Natalia Yantara, Michael Grätzel, Subodh Mhaisalkar, Nripan Mathews, and Tze Chien Sum. Slow cooling and highly efficient extraction of hot carriers in colloidal perovskite nanocrystals. *Nature Communications*, 8(May):3–12, 2017.

[11] Mingjie Li, Jianhui Fu, Qiang Xu, and Tze Chien Sum. Slow Hot-Carrier Cooling in Halide Perovskites: Prospects for Hot-Carrier Solar Cells. *Advanced Materials*, 31(47):1–17, 2019.

[12] B. Rethfeld, A. Kaiser, M. Vicanek, and G. Simon. Ultrafast dynamics of nonequilibrium electrons in metals under femtosecond laser irradiation. *Physical Review B - Condensed Matter and Materials Physics*, 65(21):2143031–21430311, 2002.

[13] Sungwoo Kim, Taehoon Kim, Sang Hyuk Im, Sang Il Seok, Kang Wook Kim, Sungjee Kim, and Sang Wook Kim. Bandgap engineered monodisperse and stable mercury telluride quantum dots and their application for near-infrared photodetection. *Journal of Materials Chemistry*, 21(39):15232–15236, 2011.

[14] L. E. Brus. Electron-electron and electron-hole interactions in small semiconductor crystallites: The size dependence of the lowest excited electronic state. *The Journal of Chemical Physics*, 80(9):4403–4409, 1984.

[15] Christopher Melnychuk and Philippe Guyot-Sionnest. Multicarrier dynamics in quantum dots. *Chemical Reviews*, 121(4):2325–2372, 2021.

[16] Anshu Pandey and Philippe Guyot-Sionnest. Slow Electron Cooling in Colloidal. *Science*, 322(November):929–32, 2008.

[17] Christopher Melnychuk and Philippe Guyot-Sionnest. Auger Suppression in n-Type HgSe Colloidal Quantum Dots. *ACS Nano*, 13(9):10512–10519, 2019.

[18] U. Bockelmann and G. Bastard. Phonon scattering and energy relaxation in two-, one-, and zero-dimensional electron gases. *Physical Review B*, 42(14):8947–8951, 1990.

[19] T. Inoshita and H. Sakaki. Electron relaxation in a quantum dot: Significance of multiphonon processes. *Physical Review B*, 46(11):7260–7263, 1992.

[20] Victor I. Klimov and Duncan W. McBranch. Femtosecond 1P-to-1S electron relaxation in strongly confined semiconductor nanocrystals. *Physical Review Letters*, 80(18):4028–4031, 1998.

[21] V. I. Klimov, Ch Schwarz, X. Yang, and D. W. McBranch. Electron and hole relaxation pathways in II-VI semiconductor nanocrystals. *Materials Research Society Symposium - Proceedings*, 536(19):211–216, 1999.

[22] E. Hendry, M. Koeberg, F. Wang, H. Zhang, C. De Mello Donegá, D. Vanmaekel-

bergh, and M. Bonn. Direct observation of electron-to-hole energy transfer in CdSe quantum dots. *Physical Review Letters*, 96(5):1–4, 2006.

[23] Patanjali Kambhampati. Hot exciton relaxation dynamics in semiconductor quantum dots: Radiationless transitions on the nanoscale. *Journal of Physical Chemistry C*, 115(45):22089–22109, 2011.

[24] David J Norris, Alexander L Efros, and Steven C Erwin. Doped nanocrystals. *Science*, 319(March):1776–1779, 2008.

[25] Richard D. Schaller, Jeffrey M. Pietryga, Serguei V. Goupalov, Melissa A. Petruska, Sergei A. Ivanov, and Victor I. Klimov. Breaking the phonon bottleneck in semiconductor nanocrystals via multiphonon emission induced by intrinsic nonadiabatic interactions. *Physical Review Letters*, 95(19):1–4, 2005.

[26] Ryan R. Cooney, Samuel L. Sewall, Kevin E.H. Anderson, Eva A. Dias, and Patanjali Kambhampati. Breaking the phonon bottleneck for holes in semiconductor Quantum dots. *Physical Review Letters*, 98(17):1–4, 2007.

[27] Frank C.M. Spoor, Lucas T. Kunneman, Wiel H. Evers, Nicolas Renaud, Ferdinand C. Grozema, Arjan J. Houtepen, and Laurens D.A. Siebbeles. Hole cooling is much faster than electron cooling in pbse quantum dots. *ACS Nano*, 10(1):695–703, 2016.

[28] Frank C.M. Spoor, Stanko Tomić, Arjan J. Houtepen, and Laurens D.A. Siebbeles. Broadband Cooling Spectra of Hot Electrons and Holes in PbSe Quantum Dots. *ACS Nano*, 11(6):6286–6294, 2017.

[29] Audrey Chu, Charlie Gréboval, Nicolas Goubet, Bertille Martinez, Clément Livache, Junling Qu, Prachi Rastogi, Francesco Andrea Bresciani, Yoann Prado, Stephan Suffit, Sandrine Ithurria, Grégory Vincent, and Emmanuel Lhuillier. Near Unity Absorption in Nanocrystal Based Short Wave Infrared Photodetectors Using Guided Mode Resonators. *ACS Photonics*, 6(10):2553–2561, 2019.

[30] Junling Qu, Prachi Rastogi, Charlie Gréboval, Delphine Lagarde, Audrey Chu, Corentin Dabard, Adrien Khalili, Hervé Cruguel, Cédric Robert, Xiang Zhen Xu, Sandrine Ithurria, Mathieu G. Silly, Simon Ferré, Xavier Marie, and Emmanuel Lhuillier. Electroluminescence from HgTe Nanocrystals and Its Use for Active Imaging. *Nano Letters*, 20(8):6185–6190, 2020.

[31] Matthew M. Ackerman, Menglu Chen, and Philippe Guyot-Sionnest. HgTe colloidal quantum dot photodiodes for extended short-wave infrared detection. *Applied Physics Letters*, 116(8), 2020.

[32] Sang Soo Chee, Charlie Gréboval, Debora Vale Magalhaes, Julien Ramade, Audrey Chu, Junling Qu, Prachi Rastogi, Adrien Khalili, Tung Huu Dang, Corentin

Dabard, Yoann Prado, Gilles Patriarche, Julien Chaste, Michael Rosticher, Sara Bals, Christophe Delerue, and Emmanuel Lhuillier. Correlating Structure and Detection Properties in HgTe Nanocrystal Films. *Nano Letters*, 21(10):4145–4151, 2021.

[33] Christopher Melnychuk and Philippe Guyot-Sionnest. Slow Auger Relaxation in HgTe Colloidal Quantum Dots. *Journal of Physical Chemistry Letters*, 9(9):2208–2211, 2018.

[34] Clément Livache, Nicolas Goubet, Bertille Martinez, Amardeep Jagtap, Junling Qu, Sandrine Ithurria, Mathieu G. Silly, Benoit Dubertret, and Emmanuel Lhuillier. Band Edge Dynamics and Multiexciton Generation in Narrow Band Gap HgTe Nanocrystals. *ACS Applied Materials and Interfaces*, 10(14):11880–11887, 2018.

[35] H. Kandori, Y. Shichida, and T. Yoshizawa. Review: Photoisomerization in rhodopsin. *Biokhimiya*, 66(11):1483–1498, 2001.

[36] John Jumper, Richard Evans, Alexander Pritzel, Tim Green, Michael Figurnov, Olaf Ronneberger, Kathryn Tunyasuvunakool, Russ Bates, Augustin Žídek, Anna Potapenko, Alex Bridgland, Clemens Meyer, Simon A.A. Kohl, Andrew J. Ballard, Andrew Cowie, Bernardino Romera-Paredes, Stanislav Nikolov, Rishub Jain, Jonas Adler, Trevor Back, Stig Petersen, David Reiman, Ellen Clancy, Michal Zielinski, Martin Steinegger, Michalina Pacholska, Tamas Berghammer, Sebastian Bodenstein, David Silver, Oriol Vinyals, Andrew W. Senior, Koray Kavukcuoglu, Pushmeet Kohli, and Demis Hassabis. Highly accurate protein structure prediction with AlphaFold. *Nature*, 596(7873):583–589, 2021.

[37] M. J. Osborne, J. Schnell, S. J. Benkovic, H. J. Dyson, and P. E. Wright. Backbone dynamics in dihydrofolate reductase complexes: Role of loop flexibility in the catalytic mechanism. *Biochemistry*, 40(33):9846–9859, 2001.

[38] P. W. Fenimore, H. Frauenfelder, B. H. McMahon, and F. G. Parak. Slaving: Solvent fluctuations dominate protein dynamics and functions. *Proceedings of the National Academy of Sciences of the United States of America*, 99(25):16047–16051, 2002.

[39] Andreas Barth and Christian Zscherp. What vibrations tell us about proteins. *Quarterly Reviews of Biophysics*, 35(4):369–430, 2002.

[40] Heejae Kim and Minhaeng Cho. Infrared probes for studying the structure and dynamics of biomolecules. *Chemical Reviews*, 113(8):5817–5847, 2013.

[41] Ramkrishna Adhikary, Jörg Zimmermann, and Floyd E. Romesberg. Transparent Window Vibrational Probes for the Characterization of Proteins with High Structural and Temporal Resolution. *Chemical Reviews*, 117(3):1927–1969, 2017.

[42] Jia Zhang, Li Wang, Jin Zhang, Jiangrui Zhu, Xin Pan, Zhifeng Cui, Jiangyun Wang, Weihai Fang, and Yunliang Li. Identifying and Modulating Accidental Fermi Resonance: 2D IR and DFT Study of 4-Azido-l-phenylalanine. *Journal of Physical Chemistry B*, 122(34):8122–8133, 2018.

[43] Donna Strickland and Gerard Mourou. Compression of amplified chirped optical pulses. *Optics Communications*, 56(3):219–221, 1985.

[44] T. Wilhelm, J. Piel, and E. Riedle. Sub-20-fs pulses tunable across the visible from a blue-pumped single-pass noncollinear parametric converter. *Optics Letters*, 22(19):1494, 1997.

[45] Robert A. Kaindl, Matthias Wurm, Klaus Reimann, Peter Hamm, Andrew M. Weiner, and Michael Woerner. Generation, shaping, and characterization of intense femtosecond pulses tunable from 3 to 20 μm. *Journal of the Optical Society of America B*, 17(12):2086, 2000.

[46] Shaul Mukamel. *Principles of Nonlinear Optical Spectroscopy*. Oxford University Press, 1995.

[47] Peter Hamm and Martin Zanni. *Concepts and Methods of 2D Infrared Spectroscopy*. Cambridge University Press, 2011.

[48] Peter Hamm, Manho Lim, and Robin M. Hochstrasser. Structure of the amide I band of peptides measured by femtosecond nonlinear-infrared spectroscopy. *Journal of Physical Chemistry B*, 102(31):6123–6138, 1998.

[49] Tobias Brixner, Tomáš Mančal, Igor V. Stiopkin, and Graham R. Fleming. Phase-stabilized two-dimensional electronic spectroscopy. *Journal of Chemical Physics*, 121(9):4221–4236, 2004.

[50] Ulrike Selig, Florian Langhojer, Frank Dimler, Tatjana Löhrig, Christoph Schwarz, Björn Gieseking, and Tobias Brixner. Inherently phase-stable coherent two-dimensional spectroscopy using only conventional optics. *Optics Letters*, 33(23):2851, 2008.

[51] Jens Bredenbeck, Jan Helbing, Christoph Kolano, and Peter Hamm. Ultrafast 2D-IR spectroscopy of transient species. *ChemPhysChem*, 8(12):1747–1756, 2007.

[52] Luuk J.G.W. Van Wilderen, Andreas T. Messmer, and Jens Bredenbeck. Mixed IR/Vis two-dimensional spectroscopy: Chemical exchange beyond the vibrational lifetime and sub-ensemble selective photochemistry. *Angewandte Chemie - International Edition*, 53(10):2667–2672, 2014.

[53] Sean Garrett-Roe and Peter Hamm. Purely absorptive three-dimensional infrared spectroscopy. *Journal of Chemical Physics*, 130(16), 2009.

[54] Sean Garrett-Roe, Fivos Perakis, Francesco Rao, and Peter Hamm. Three-dimensional infrared spectroscopy of isotope-substituted liquid water reveals heterogeneous dynamics. *Journal of Physical Chemistry B*, 115(21):6976–6984, 2011.

[55] Hélène Seiler, Samuel Palato, Colin Sonnichsen, Harry Baker, and Patanjali Kambhampati. Seeing Multiexcitons through Sample Inhomogeneity: Band-Edge Biexciton Structure in CdSe Nanocrystals Revealed by Two-Dimensional Electronic Spectroscopy. *Nano Letters*, 18(5):2999–3006, 2018.

[56] Jens Bredenbeck, Jan Helbing, Karin Nienhaus, G. Ulrich Nienhaus, and Peter Hamm. Protein ligand migration mapped by nonequilibrium 2D-IR exchange spectroscopy. *Proceedings of the National Academy of Sciences of the United States of America*, 104(36), 2006.

[57] M. L. Cowan, B. D. Bruner, N. Huse, J. R. Dwyer, B. Chugh, E. T.J. Nibbering, T. Elsaesser, and R. J.D. Miller. Ultrafast memory loss and energy redistribution in the hydrogen bond network of liquid H2O. *Nature*, 434(7030):199–202, 2005.

[58] K. I. Kang, A. D. Kepner, S. V. Gaponenko, S. W. Koch, Y. Z. Hu, and N. Peyghambarian. Confinement-enhanced biexciton binding energy in semiconductor quantum dots. *Physical Review B*, 48(20):15449–15452, 1993.

[59] G. Moody, R. Singh, H. Li, I. A. Akimov, M. Bayer, D. Reuter, A. D. Wieck, and S. T. Cundiff. Correlation and dephasing effects on the non-radiative coherence between bright excitons in an InAs QD ensemble measured with 2D spectroscopy. *Solid State Communications*, 163:65–69, 2013.

[60] N. Demirdöven, M. Khalil, and A. Tokmakoff. Correlated Vibrational Dynamics Revealed by Two-Dimensional Infrared Spectroscopy. *Physical Review Letters*, 89(23):1–4, 2002.

[61] Jan Helbing and Peter Hamm. Compact implementation of Fourier transform two-dimensional IR spectroscopy without phase ambiguity. *Journal of the Optical Society of America B*, 28(1):171, 2011.

[62] C. B. Murray, D. J. Norris, and M. G. Bawendi. Synthesis and Characterization of Nearly Monodisperse CdE (E = S, Se, Te) Semiconductor Nanocrystallites. *Journal of the American Chemical Society*, 115(19):8706–8715, 1993.

[63] A.J. Nozik. Quantum Dot Solar Cells. *Physica E*, 14:115–120, 2002.

[64] Prashant V. Kamat. Quantum dot solar cells. Semiconductor nanocrystals as light harvesters. *Journal of Physical Chemistry C*, 112(48):18737–18753, 2008.

[65] Benoit Dubertret, Paris Skourides, David J. Norris, Vincent Noireaux, Ali H. Brivanlou, and Albert Libchaber. In vivo imaging of quantum dots encapsulated in phospholipid micelles. *Science*, 298(5599):1759–1762, 2002.

[66] Igor L. Medintz, H. Tetsuo Uyeda, Ellen R. Goldman, and Hedi Mattoussi. Quantum dot bioconjugates for imaging, labelling and sensing. *Nature Materials*, 4(6):435–446, 2005.

[67] V. I. Klimov, A. A. Mikhailovsky, S. Xu, A. Malko, J. A. Hollingsworth, C. A. Leatherdale, H. J. Eisler, and M. G. Bawendi. Optical gain and stimulated emission in nanocrystal quantum dots. *Science*, 290(5490):314–317, 2000.

[68] Jaehoon Lim, Young Shin Park, and Victor I. Klimov. Optical gain in colloidal quantum dots achieved with direct-current electrical pumping. *Nature Materials*, 17(1):42–48, 2018.

[69] R. D. Schaller and V. I. Klimov. High efficiency carrier multiplication in PbSe nanocrystals: Implications for solar energy conversion. *Physical Review Letters*, 92(18):1–4, 2004.

[70] Mingjie Li, Raihana Begum, Jianhui Fu, Qiang Xu, Teck Ming Koh, Sjoerd A. Veldhuis, Michael Grätzel, Nripan Mathews, Subodh Mhaisalkar, and Tze Chien Sum. Low threshold and efficient multiple exciton generation in halide perovskite nanocrystals. *Nature Communications*, 9(1):3–9, 2018.

[71] S. I. Pokutnii. Exciton binding energy in semiconductor quantum dots. *Semiconductors*, 44(4):488–493, 2010.

[72] M. Dyakonov, T. Amand, R. Harley, M. Bayer, J. Huebner, J. Cibert, W. Ivchenko, E.L.Jantsch, M. Johnson, S. Ganichev, and V. Kalevich. *Spin Physics in Semiconductors*. Springer, 2008.

[73] M. Nirmal, D. J. Norris, M. Kuno, M. G. Bawendi, Al L. Efros, and M. Rosen. Observation of the "dark exciton" in CdSe quantum dots. *Physical Review Letters*, 75(20):3728–3731, 1995.

[74] A.R. Beattie and P.T. Landsberg. Auger Effect in Semiconductors. *Proc. Royal Soc. London A*, 246(1256):16–29, 1959.

[75] Francesco Bertazzi, Michele Goano, and Enrico Bellotti. Auger lifetime in narrow gap semiconductors. *2010 14th International Workshop on Computational Electronics, IWCE 2010*, pages 179–182, 2010.

[76] Lin Wang Wang, Marco Califano, Alex Zunger, and Alberto Franceschetti. Pseudopotential Theory of Auger Processes in CdSe Quantum Dots. *Physical Review Letters*, 91(5):1–4, 2003.

[77] V. I. Klimov, A. A. Mikhailovsky, D. W. McBranch, C. A. Leatherdale, and M. G. Bawendi. Quantization of multiparticle Auger rates in semiconductor quantum dots. *Science*, 287(5455):1011–1014, 2000.

[78] V. I. Klimov, J. A. McGuire, R. D. Schaller, and V. I. Rupasov. Scaling of multiexciton lifetimes in semiconductor nanocrystals. *Physical Review B - Condensed Matter and Materials Physics*, 77(19):1–12, 2008.

[79] Benjamin T. Diroll, Peijun Guo, and Richard D. Schaller. Heat Transfer at Hybrid Interfaces: Interfacial Ligand-to-Nanocrystal Heating Monitored with Infrared Pump, Electronic Probe Spectroscopy. *Nano Letters*, 18(12):7863–7869, 2018.

[80] Timothy G. Mack, Lakshay Jethi, Mark Andrews, and Patanjali Kambhampati. Direct Observation of Vibronic Coupling between Excitonic States of CdSe Nanocrystals and Their Passivating Ligands. *Journal of Physical Chemistry C*, 123(8):5084–5091, 2019.

[81] Philippe Guyot-Sionnest, Brian Wehrenberg, and Dong Yu. Intraband relaxation in CdSe nanocrystals and the strong influence of the surface ligands. *Journal of Chemical Physics*, 123(7), 2005.

[82] A. Franceschetti, J. M. An, and A. Zunger. Impact ionization can explain carrier multiplication in PbSe quantum dots. *Nano Letters*, 6(10):2191–2195, 2006.

[83] Matthew C. Beard, Aaron G. Midgett, Mark C. Hanna, Joseph M. Luther, Barbara K. Hughes, and Arthur J. Nozik. Comparing multiple exciton generation in quantum dots to impact ionization in bulk semiconductors: Implications for enhancement of solar energy conversion. *Nano Letters*, 10(8):3019–3027, 2010.

[84] John T. Stewart, Lazaro A. Padilha, M. Mumtaz Qazilbash, Jeffrey M. Pietryga, Aaron G. Midgett, Joseph M. Luther, Matthew C. Beard, Arthur J. Nozik, and Victor I. Klimov. Comparison of carrier multiplication yields in PbS and PbSe nanocrystals: The role of competing energy-loss processes. *Nano Letters*, 12(2):622–628, 2012.

[85] John T. Stewart, Lazaro A. Padilha, Wan Ki Bae, Weon Kyu Koh, Jeffrey M. Pietryga, and Victor I. Klimov. Carrier multiplication in quantum dots within the framework of two competing energy relaxation mechanisms. *Journal of Physical Chemistry Letters*, 4(12):2061–2068, 2013.

[86] T. C. Harman, W. H. Kleiner, A. J. Strauss, G. B. Wright, J. G. Mavroides, J. M. Honig, and D. H. Dickey. Band structure of HgTe and HgTe-CdTe alloys. *Solid State Communications*, 2(10):305–308, 1964.

[87] G. A. Antypas. Liquid-Phase Epitaxy of Inx Ga1-xAs. *Journal of The Electrochemical Society*, 117(11):1393, 1970.

[88] Emmanuel Lhuillier, Sean Keuleyan, Heng Liu, and Philippe Guyot-Sionnest. Colloidal HgTe material for low-cost detection into the MWIR. *Journal of Electronic Materials*, 41(10):2725–2729, 2012.

[89] Andrey Rogach, Stephen Kershaw, Mike Burt, Mike Harrison, Andreas Kornowski, Alexander Eychmüller, and Horst Weller. Colloidally prepared HgTe nanocrystals with strong room-temperature infrared luminescence. *Advanced Materials*, 11(7):552–555, 1999.

[90] Sean Keuleyan, Emmanuel Lhuillier, and Philippe Guyot-Sionnest. Synthesis of colloidal HgTe quantum dots for narrow mid-IR emission and detection. *Journal of the American Chemical Society*, 133(41):16422–16424, 2011.

[91] Sean Keuleyan, Emmanuel Lhuillier, Vuk Brajuskovic, and Philippe Guyot-Sionnest. Mid-infrared HgTe colloidal quantum dot photodetectors. *Nature Photonics*, 5(8):489–493, 2011.

[92] Matthew M. Ackerman, Xin Tang, and Philippe Guyot-Sionnest. Fast and Sensitive Colloidal Quantum Dot Mid-Wave Infrared Photodetectors. *ACS Nano*, 12(7):7264–7271, 2018.

[93] Bingqing Zhu, Mengyu Chen, Qiang Zhu, Guodong Zhou, Nema M. Abdelazim, Wen Zhou, Stephen V. Kershaw, Andrey L. Rogach, Ni Zhao, and Hon Ki Tsang. Integrated Plasmonic Infrared Photodetector Based on Colloidal HgTe Quantum Dots. *Advanced Materials Technologies*, 4(10):1–8, 2019.

[94] Yifan Dong, Mengyu Chen, Wai Kin Yiu, Qiang Zhu, Guodong Zhou, Stephen V. Kershaw, Ning Ke, Ching Ping Wong, Andrey L. Rogach, and Ni Zhao. Solution Processed Hybrid Polymer: HgTe Quantum Dot Phototransistor with High Sensitivity and Fast Infrared Response up to 2400 nm at Room Temperature. *Advanced Science*, 7(12):1–9, 2020.

[95] Menglu Chen, Xinzheng Lan, Xin Tang, Yuanyuan Wang, Margaret H. Hudson, Dmitri V. Talapin, and Philippe Guyot-Sionnest. High Carrier Mobility in HgTe Quantum Dot Solids Improves Mid-IR Photodetectors. *ACS Photonics*, 6(9):2358–2365, 2019.

[96] Amardeep Jagtap, Nicolas Goubet, Clément Livache, Audrey Chu, Bertille Martinez, Charlie Gréboval, Junling Qu, Erwan Dandeu, Loïc Becerra, Nadine Witkowski, Sandrine Ithurria, Fabrice Mathevet, Mathieu G. Silly, Benoit Dubertret, and Emmanuel Lhuillier. Short Wave Infrared Devices Based on HgTe Nanocrystals with Air Stable Performances. *Journal of Physical Chemistry C*, 122(26):14979–14985, 2018.

[97] Xin Tang, Matthew M. Ackerman, Guohua Shen, and Philippe Guyot-Sionnest. Towards Infrared Electronic Eyes: Flexible Colloidal Quantum Dot Photovoltaic Detectors Enhanced by Resonant Cavity. *Small*, 15(12):1–7, 2019.

[98] Pieter Geiregat, Arjan J. Houtepen, Laxmi Kishore Sagar, Ivan Infante, Felipe Zapata, Valeriia Grigel, Guy Allan, Christophe Delerue, Dries Van Thourhout,

and Zeger Hens. Continuous-wave infrared optical gain and amplified spontaneous emission at ultralow threshold by colloidal HgTe quantum dots. *Nature Materials*, 17(1):35–41, 2018.

[99] E. Lhuillier, S. Keuleyan, H. Liu, and P. Guyot-Sionnest. Mid-IR colloidal nanocrystals. *Chemistry of Materials*, 25(8):1272–1282, 2013.

[100] Guy Allan and Christophe Delerue. Tight-binding calculations of the optical properties of HgTe nanocrystals. *Physical Review B - Condensed Matter and Materials Physics*, 86(16):1–6, 2012.

[101] Margaret H. Hudson, Menglu Chen, Vladislav Kamysbayev, Eric M. Janke, Xinzheng Lan, Guy Allan, Christophe Delerue, Byeongdu Lee, Philippe Guyot-Sionnest, and Dmitri V. Talapin. Conduction Band Fine Structure in Colloidal HgTe Quantum Dots. *ACS Nano*, 12(9):9397–9404, 2018.

[102] Ali Al-Otaify, Stephen V. Kershaw, Shuchi Gupta, Andrey L. Rogach, Guy Allan, Christophe Delerue, and David J. Binks. Multiple exciton generation and ultrafast exciton dynamics in HgTe colloidal quantum dots. *Physical Chemistry Chemical Physics*, 15(39):16864–16873, 2013.

[103] Stephen V. Kershaw and Andrey L. Rogach. Carrier multiplication mechanisms and competing processes in colloidal semiconductor nanostructures. *Materials*, 10(9), 2017.

[104] Chao Ding, Feng Liu, Yaohong Zhang, Daisuke Hirotani, Xing Rin, Shuzi Hayase, Takashi Minemoto, Taizo Masuda, Ruixiang Wang, and Qing Shen. Photoexcited hot and cold electron and hole dynamics at FAPbI3 perovskite quantum dots/metal oxide heterojunctions used for stable perovskite quantum dot solar cells. *Nano Energy*, 67(October 2019):104267, 2020.

[105] V. I. Klimov, Ch J. Schwarz, D. W. Mc Branch, C. A. Leatherdale, and M. G. Bawendi. Ultrafast dynamics of inter- and intraband transitions in semiconductor nanocrystals: Implications for quantum-dot lasers. *Physical Review B - Condensed Matter and Materials Physics*, 60(4):R2177–R2180, 1999.

[106] Ryan R. Cooney, Samuel L. Sewall, Eva A. Dias, D. M. Sagar, Kevin E.H. Anderson, and Patanjali Kambhampati. Unified picture of electron and hole relaxation pathways in semiconductor quantum dots. *Physical Review B - Condensed Matter and Materials Physics*, 75(24):1–14, 2007.

[107] H. Seiler, S. Palato, and P. Kambhampati. Investigating exciton structure and dynamics in colloidal CdSe quantum dots with two-dimensional electronic spectroscopy. *Journal of Chemical Physics*, 149(7), 2018.

[108] Guohua Shen, Menglu Chen, and Philippe Guyot-Sionnest. Synthesis of Nonaggre-

gating HgTe Colloidal Quantum Dots and the Emergence of Air-Stable n-Doping. *Journal of Physical Chemistry Letters*, 8(10):2224–2228, 2017.

[109] Zhi Wang, Mona Rafipoor, Pablo Garcia Risueño, Jan Philip Merkl, Peng Han, Holger Lange, and Gabriel Bester. Phonon-Assisted Auger Process Enables Ultrafast Charge Transfer in CdSe Quantum Dot/Organic Molecule. *Journal of Physical Chemistry C*, 123(28):17127–17135, 2019.

[110] Poul B. Petersen and Andrei Tokmakoff. Source for ultrafast continuum infrared and terahertz radiation. *Optics Letters*, 35(12):1962, 2010.

[111] D.M. Vasudevan, S. Sreekumari, and K. Vaidyanathan. *Textbook of Biochemistry for Medical Students*. Jaypee Brothers Medical Publishers (P) Ltd, 6 edition, 2011.

[112] Lubert Stryer. *Biochemistry*. W.H. Freeman and Co, 3 edition, 1988.

[113] Luuk J.G.W. Van Wilderen, Daniela Kern-Michler, Henrike M. Müller-Werkmeister, and Jens Bredenbeck. Vibrational dynamics and solvatochromism of the label SCN in various solvents and hemoglobin by time dependent IR and 2D-IR spectroscopy. *Physical Chemistry Chemical Physics*, 16(36):19643–19653, 2014.

[114] Larissa Blankenburg, Lea Schroeder, Florian Habenstein, Bartosz Błasiak, Tilman Kottke, and Jens Bredenbeck. Following local light-induced structure changes and dynamics of the photoreceptor PYP with the thiocyanate IR label. *Physical Chemistry Chemical Physics*, 21(12):6622–6634, 2019.

[115] Julian M. Schmidt-Engler, Rene Zangl, Patrick Guldan, Nina Morgner, and Jens Bredenbeck. Exploring the 2D-IR repertoire of the -SCN label to study site-resolved dynamics and solvation in the calcium sensor protein calmodulin. *Physical Chemistry Chemical Physics*, 22(10):5463–5475, 2020.

[116] J. Edler and P. Hamm. Two-dimensional vibrational spectroscopy of the amide I band of crystalline acetanilide: Fermi resonance, conformational substates, or vibrational self-trapping? *Journal of Chemical Physics*, 119(5):2709–2715, 2003.

[117] Jacob S. Lipkin, Rui Song, Edward E. Fenlon, and Scott H. Brewer. Modulating accidental fermi resonance: What a difference a neutron makes. *Journal of Physical Chemistry Letters*, 2(14):1672–1676, 2011.

[118] K. D. Bier and H. J. Jodl. Tuning of the Fermi resonance of CO2 and CS2 by temperature, pressure, and matrix material. *The Journal of Chemical Physics*, 86(8):4406–4410, 1987.

[119] Jeffrey M. Rodgers, Rachel M. Abaskharon, Bei Ding, Jianxin Chen, Wenkai Zhang, and Feng Gai. Fermi resonance as a means to determine the hydrogen-bonding status of two infrared probes. *Physical Chemistry Chemical Physics*, 19(24):16144–16150, 2017.

[120] Henning Tidow and Poul Nissen. Structural diversity of calmodulin binding to its target sites. *FEBS Journal*, 280(21):5551–5565, 2013.

[121] Frits C Stevens. Calmodulin: an introduction. *Can. J. Biochem. Cell Biol.*, 61(5):906–910, 1982.

[122] Kristen L. Kelly, Shannon R. Dalton, Rebecca B. Wai, Kanika Ramchandani, Rosalind J. Xu, Sara Linse, and Casey H. Londergan. Conformational Ensembles of Calmodulin Revealed by Nonperturbing Site-Specific Vibrational Probe Groups. *Journal of Physical Chemistry A*, 122(11):2947–2955, 2018.

[123] Thibault Apretna, Sylvain Massabeau, Charlie Gréboval, Nicolas Goubet, Jérôme Tignon, Sukhdeep Dhillon, Francesca Carosella, Robson Ferreira, Emmanuel Lhuillier, and Juliette Mangeney. Few picosecond dynamics of intraband transitions in THz HgTe nanocrystals. *Nanophotonics*, 10(10):2753–2763, 2021.

6 Acknowledgments

7 Appendix

7.1 Supporting information: Intraband dynamics of mid-infrared HgTe Quantum dots

Reprinted from *Nanoscale*, 2022, 14, 4123.

SUPPORTING INFORMATION

Intraband dynamics of mid-infrared HgTe Quantum dots

Matthias Ruppert[1], Hanh Bui[2,3,†], Laxmi Kishore Sagar[4,5,†], Pieter Geiregat[4,5], Zeger Hens[4,5], Gabriel Bester[2,3], and Nils Huse[1,3*]

[1]Institute for Nanostructure and Solid-State Physics, Department of Physics, University of Hamburg and Center for Free-Electron Laser Science, Luruper Chaussee 149, 22761 Hamburg, Germany

[2]Physical Chemistry and Physics departments, University of Hamburg, Luruper Chaussee 149, 22761 Hamburg, Germany

[3]The Hamburg Centre for Ultrafast Imaging, University of Hamburg, Luruper Chaussee, 149, 22761 Hamburg, Germany

[4]Physics and Chemistry of Nanostructures, Department of Chemistry, Ghent University, Krijgslaan 281 - S3 B-9000 Gent, Belgium

[5]Center for Nano and Biophotonics, Ghent University, Technologiepark Zwijnaarde 15 B-9052 Gent, Belgium

[†]Current addresses:
HB: Faculty of Fundamental Science, Phenikaa University, Yen Nghia, Ha-Dong District, Hanoi, 10000, Viet Nam
LKS: Department of Electrical and Computer Engineering, University of Toronto, 10 King's College Road, Toronto, Ontario M5S 3G4, Canada

*Corresponding author: nils.huse@uni-hamburg.de

Modelling of band edge dynamics

To include exciton cooling in the band-gap dynamics upon non-resonant excitation, we employ a rate equation model as depicted in figure 1. Excitation by the laser is treated as instantaneous, which creates a highly excited electron hole pair $|e_i,h_i\rangle$. This exciton then relaxes to lowest excitonic state $|e_0,h_0\rangle$ with a cooling time τ_c. The exciton recombination time is denoted as τ_e. Since the exciton cooling times are much shorter than the recombination time (also see figure 2) we neglect direct recombination of the initial state $|e_i,h_i\rangle$. The populations of the initial state, N_i, and ground state, N_0, are then described by the resulting differential equation:

$$\frac{dN_i}{d_t} = -\frac{N_i}{\tau_c} \qquad (1)$$

$$\frac{dN_0}{d_t} = -\frac{N_0}{\tau_e} - \frac{dN_i}{d_t} \qquad (2)$$

It has the following solution for the band-gap state population upon non-resonant excitation:

$$N_0(t) = \Theta(t) \cdot \frac{N_i(0) \cdot \tau_e}{\tau_c - \tau_e} \cdot \left[\exp\left(-\frac{t}{\tau_c}\right) - \exp\left(-\frac{t}{\tau_e}\right) \right] \cdot \qquad (3)$$

This equation still holds for resonant excitation, in the limit of vanishing cooling time. To incorporate bi-exciton dynamics into this model, we mimic the commonly used bi-exponential model[1,2] by using two instances of the above equation, one representing the single exciton decay, the other one the bi-exciton recombination, where the exciton lifetime, τ_e is replaced by the bi-exciton recombination time, τ_b, arriving at:

$$N_{0(t)} = \Theta(t) \cdot \left[\frac{N_{i,e}(0)\tau_e}{\tau_c - \tau_e} \cdot \left(\exp\left(-\frac{t}{\tau_c}\right) - \exp\left(-\frac{t}{\tau_e}\right) \right) + \frac{N_{i,b}(0)\tau_b}{\tau_c - \tau_b} \cdot \left(\exp\left(-\frac{t}{\tau_c}\right) - \exp\left(-\frac{t}{\tau_b}\right) \right) \right]. \qquad (4)$$

Here, $N_{i,e}(0)$ and $N_{i,b}(0)$ denote the number of excited electron hole pairs in particles with a single exciton only and particles with two excitons, respectively.

Calculation of the mean excitation number from the band-gap dynamics

We first consider a population conserving rate-equation model for Auger decay of bi-excitons and recombination of excitons:

$$\frac{dN_B(t)}{dt} = -\frac{N_B(t)}{\tau_B} \qquad (5)$$

$$\frac{dN_E(t)}{dt} = -\frac{N_E(t)}{\tau_E} - \frac{dN_B(t)}{dt} \ . \tag{6}$$

Here, τ_B and τ_E are the Auger decay time for bi-excitons and the recombination time of excitons, N_B and N_E denote the numbers of excited bi-excitons and excitons, respectively. It was assumed that all bi-excitons decay into excitons via direct recombination, i.e. there is no direct recombination for bi-excitons, which is a reasonable approximation given the more than 20-fold difference in lifetimes. The solution to equations 5+6 is:

$$N_B(t) = N_B \cdot e^{-\frac{t}{\tau_B}} \tag{7}$$

$$N_E(t) = \left(N_E + \frac{\tau_E}{\tau_E - \tau_B} N_B\right) e^{-\frac{t}{\tau_E}} - \frac{\tau_E}{\tau_E - \tau_B} N_B \cdot e^{-\frac{t}{\tau_B}}. \tag{8}$$

From equations 7+8 the bleach signal, $S(t)$, is constructed as:

$$S(t) \propto N_E(t) + 2 \cdot N_B(t) \tag{9}$$

$$\propto \left(N_E + \frac{\tau_E}{\tau_E - \tau_B} N_B\right) e^{-\frac{t}{\tau_E}} + \left(2 - \frac{\tau_E}{\tau_E - \tau_B}\right) N_B \cdot e^{-\frac{t}{\tau_B}}. \tag{10}$$

This retrieves the commonly used bi-exponential model for multi-excitonic decays. The factor of 2 accounts for the fact, that the bi-excitonic state results in approximately twice the bleach signal as a singly excited quantum dot. For low excitations densities, we assume Poissonian statistics for the probability, P(N), to find N excitations in a single particle:

$$P(N) = \frac{\langle N \rangle^N}{N!} \cdot e^{-\langle N \rangle}. \tag{11}$$

.

Comparing the probabilities for double and single excitations in equation 11, the mean exciton number per particle, $<N>$, is found as

$$\langle N \rangle = 2 \cdot \frac{P(2)}{P(1)} = 2 \cdot \frac{N_B}{N_E}. \tag{12}$$

The parameters N_B and N_E can be extracted from a bi-exponentail fit of the band-gap dynamics in conjunction with equation 10.

In the limit $\tau_B \ll \tau_E$ the temporal evolution of the bleach signal (equation 10) could also be simplified to

$$S(t) \propto (N_E + N_B)e^{-\frac{t}{\tau_E}} + N_B \cdot e^{-\frac{t}{\tau_B}}. \tag{13}$$

For the exciton and bi-exciton lifetimes presented in this work, this would lead to an overestimation for N_B of approximately 5%. In the regime of a bi-exponential model for the band-gap dynamics,

$$S(t) = A_{fast} \cdot e^{-\frac{t}{\tau_{fast}}} + A_{slow} \cdot e^{-\frac{t}{\tau_{slow}}}, \tag{14}$$

the exciton numbers can be estimated as $N_{biexc} = A_{fast}$ and $N_{exc} = A_{slow} - A_{fast}$, leaving

$$< N > = 2 \cdot \frac{N_B}{N_E} \tag{15}$$

$$= 2 \cdot \frac{A_{fast}}{A_{slow} - A_{fast}}. \tag{16}$$

Extracting the exciton and bi-exciton numbers from a bi-exponential fit is only valid as long, as there are no tri-excitons present, as they are not accounted for in the model. We estimate, that this treatment is valid, as long as there are at least tenfold more bi-excitons than tri-excitons. From equation 11 one can derive:

$$\frac{P(3)}{P(2)} = \frac{\langle N \rangle}{3} \leq 0.1 \tag{17}$$

$$\Rightarrow \langle N \rangle \leq 0.3 \tag{18}$$

An overview of extracted mean exciton numbers for low fluences can be found in the inset of figure S1.

Excitation density dependence of the transient signal

In the MEG range, Poisson statics can no longer be employed. We therefore employ an Einstein coefficient-based approach to be able to compare excitations densities below and above the MEG onset. We neglect carrier relaxation during our 100 fs pump pulse. The carrier dynamics can then be described by excitation by photon absorption and de-excitation by stimulated emission. Using the Einstein-coefficient for absorption, A, the number of excited electron hole pairs, N, can be described as:

$$dN = A \cdot N_{gs} \cdot dP - A \cdot N \cdot dP \tag{19}$$

$$= A \cdot (N_{tot} - 2N) \cdot dP. \tag{20}$$

Here, N_{gs} denotes the number of unexcited electron hole pairs, P is the excitation power. N_{tot} is the number of electron hole pairs in the system that are in resonance with the pump. This inhomogeneous differential equation is solved by:

$$N(P) = 0.5 \cdot N_{tot} \cdot (1 - e^{-2AP}). \tag{21}$$

This relationship gives a good representation for our data as shown in figure S1. Here, F_0 denotes the fluence, at which 50% of the saturation value is reached. For excitations below the MEG onset

also the mean exciton numbers extracted from the band gap dynamics as described above are shown in the inset. The linear relation between the mean exciton number, $\langle N \rangle$, and the normalized fluence is commensurate with the two-fold degenerate LUMO state in the se particles and further justifies the Einstein coefficient-based approach.
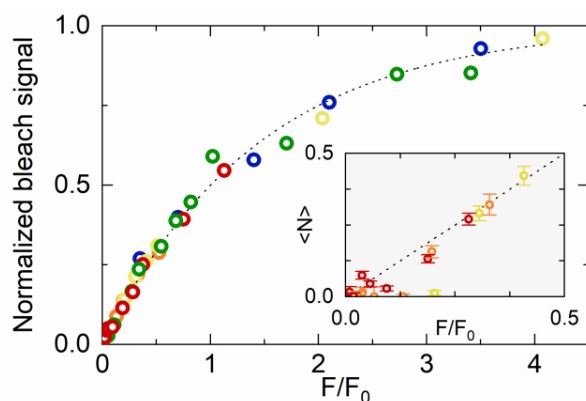

Figure S1: Normalized bleach signal as a function of pump fluence. All data points have been fit to a model based on Einstein coefficients for absorption and stimulated emission (dotted line). The value F_0 denotes the fluence, where 50% of the saturation value is reached, which is also the threshold for a linear relationship between fluence and bleach signal. Different pump wavelengths are color-coded as 2.4 µm (red), 2.0 µm (orange), 1.2 µm (yellow), 800 nm (green) and 400 nm (blue). The inset shows the mean exciton number per quantum dot as retrieved from Poissonian statistics using the same normalized fluence.

References

1. Melnychuk, C. & Guyot-Sionnest, P. Slow Auger Relaxation in HgTe Colloidal Quantum Dots. *J. Phys. Chem. Lett.* **9**, 2208–2211 (2018).

2. Melnychuk, C. & Guyot-Sionnest, P. Multicarrier dynamics in quantum dots. *Chem. Rev.* **121**, 2325–2372 (2021).

7.2 Supporting information: Population dynamics of stretching excitations of p-azido-phenylalanine incorporated in calmodulin-peptide complexes

Reprinted from *J. Phys. Chem. B*, 2022, 126, 368-375.

SUPPORTING INFORMATION

Population dynamics of stretching excitations of p-azido-phenylalanine incorporated in calmodulin-peptide complexes

Matthias Ruppert,[1*] Anne Creon,[1,2*] Henning Tidow,[2,3+] and Nils Huse[1,3+]

[1]Hamburg Advanced Research Centre for Bioorganic Chemistry, Institute for Nanostructure and Solid-State Physics, Department of Physics and Center for Free-Electron Laser Science, University of Hamburg, Luruper Chaussee 149, D-22761 Hamburg, Germany

[2]Hamburg Advanced Research Centre for Bioorganic Chemistry, Institute for Biochemistry and Molecular Biology, Department of Chemistry, University of Hamburg, Martin-Luther-King-Platz 6, D-20146 Hamburg, Germany

[3]The Hamburg Centre for Ultrafast Imaging, University of Hamburg, Luruper Chaussee, 149, D-22761 Hamburg, Germany

[*]These authors have contributed equally to this work.

[+]Corresponding authors: tidow@chemie.uni-hamburg.de, nils.huse@uni-hamburg.de

1
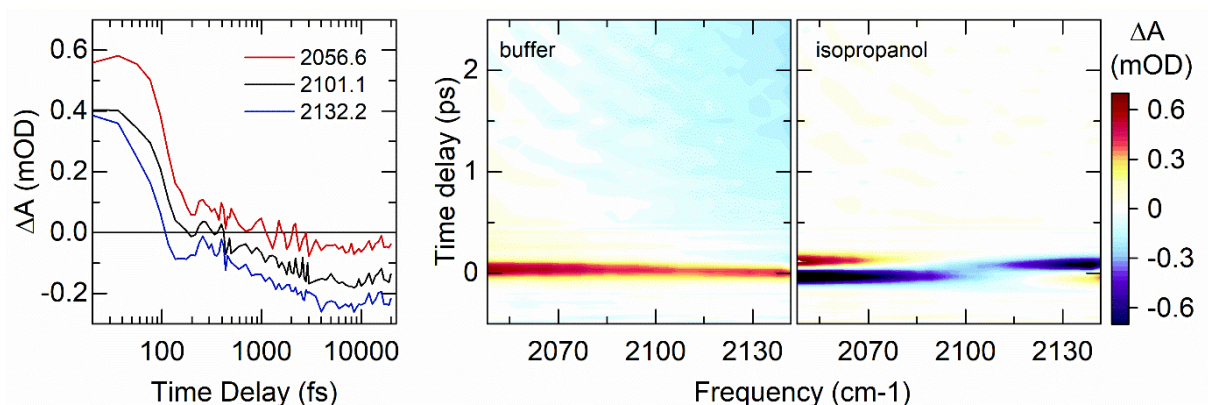
Transient background signals

Figure S1: Transient background contributions. Left, middle panel: transient signal of the aqueous buffer solution. Right panel: Non-resonant response of the sample cell, measured using isopropanol.

Figure S1 shows the main contributions of the background that was subtracted from our data: the transient signal of the aqueous buffer (left, middle panel) and the non-resonant cross-phase modulation (CPM) signal in the CaF_2 windows of the sample cell (right panel). This CPM signal of our sample cell was measured using isopropanol, which is fully transparent within our pulse spectrum. To obtain the isolated buffer response, the non-resonant contributions from the CaF_2 windows have been subtracted in the data shown here. There is no appreciable remainder of the cross-phase modulation signal, even though there is a difference in absorbance of 250 mOD between the buffer solution and isopropanol. We thus deduct that the data shown in the article is not distorted by an imperfect CPM subtraction procedure, as the differences between buffer solution and the different samples are less than 10 mOD leading to even smaller modulations in CPM amplitudes due to sample absorption.

The transient signal of the buffer solution features two main components: a large positive feature which decays on the order of our instrument response, as can be seen by comparison to the CPM signal. The long-lived negative component increases in magnitude with higher wavenumbers and longer time delays. Therefore, the transient signal at very large time delays can be regarded as an upper limit for errors from subtraction of the transient buffer signal. This upper limit is shown in figure 3 in the article.

2

Line shape analysis of time-resolved differential spectral data

$$S(x) = y0 + A * \left[\exp\left(\frac{-4\ln(2) * (x - x_1)^2}{FWHM_1^2} \right) - R * \exp\left(\frac{-4\ln(2) * (x - x_2)^2}{\left(2 * \frac{FWHM_2}{1 + \exp(s * (x - x_2))} \right)^2} \right) \right]$$

We used the heuristic line-shape above to model the differential absorption spectrum for positive time-delays. Induced absorption (IA) and ground state bleach (GSB) signals are modeled by a sum of a Gaussian centered at x_1 and $FWHM_1$ and a skewed Gaussian[1] centered at x_2, with $FWHM_2$ containing the asymmetry parameter s. R describes approximately the ratio between IA and GSB. A global fit was used to fit all spectra with shared parameters except for signal amplitude, *A*, and offset, y_0. The amplitudes obtained from the global fit do not suffer from offset fluctuations. This data analysis enhances the signal-to-noise ratio of the population dynamics. We quantify our error for the extracted amplitude, *A*, with the residual sum of squares, *RSS*, for each line shape fit: $\delta A = \sqrt{RSS/32}$, with 32 as the pixel number per line of our dual-line detector. We have used the resulting error bars, shown in Fig. 4, as weights in the consecutive fit of the quantum beat model to the population dynamics. Exemplary fits to the experimental data are shown in Figures S2 - S6.
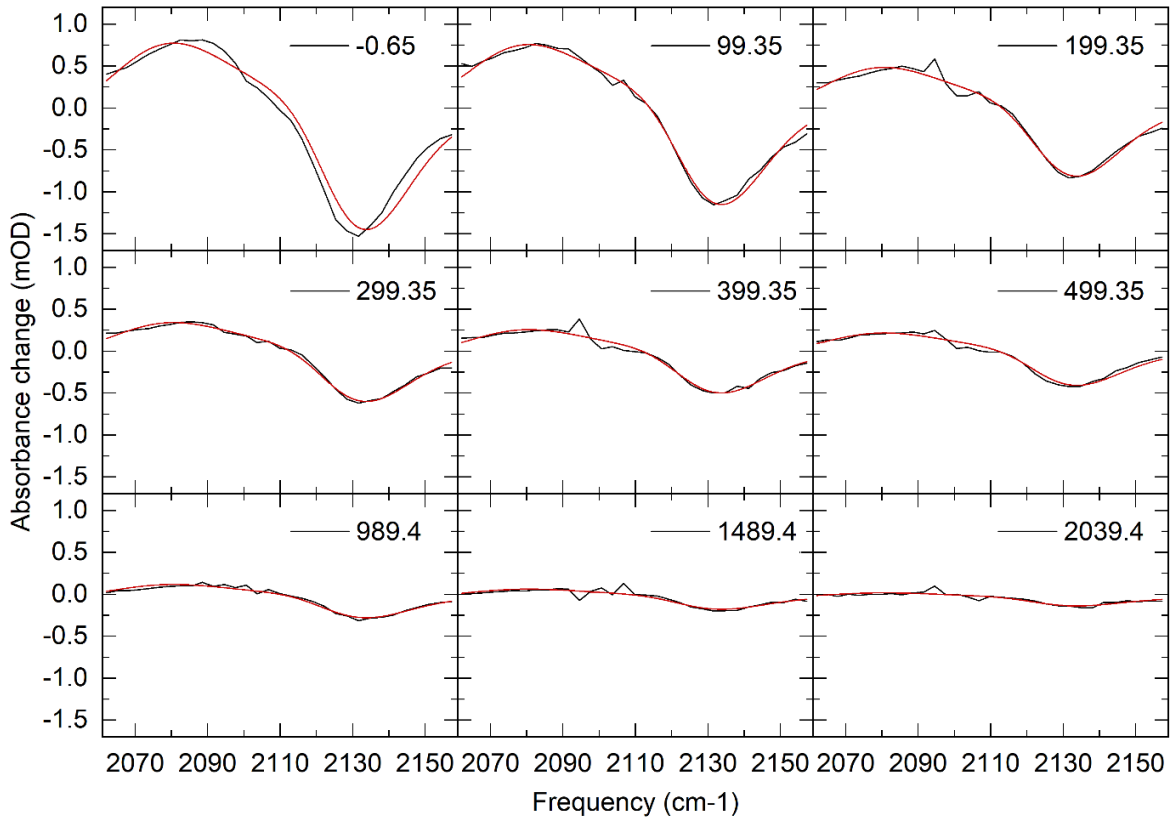

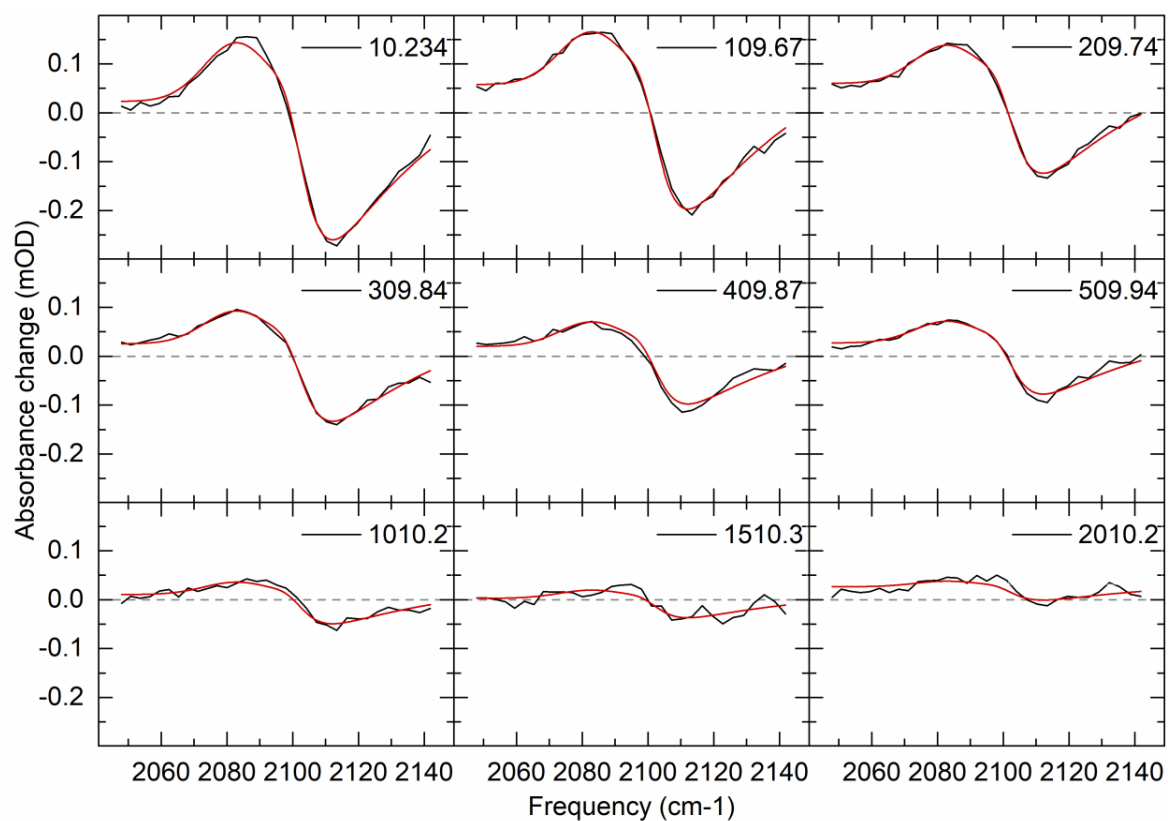**Figure S2:** Transient spectra of AzF for different time steps in fs (black) and global line-fit (red).

3

Figure S3: Transient spectra of CaM for different time steps in fs (black) and global line-fit (red).
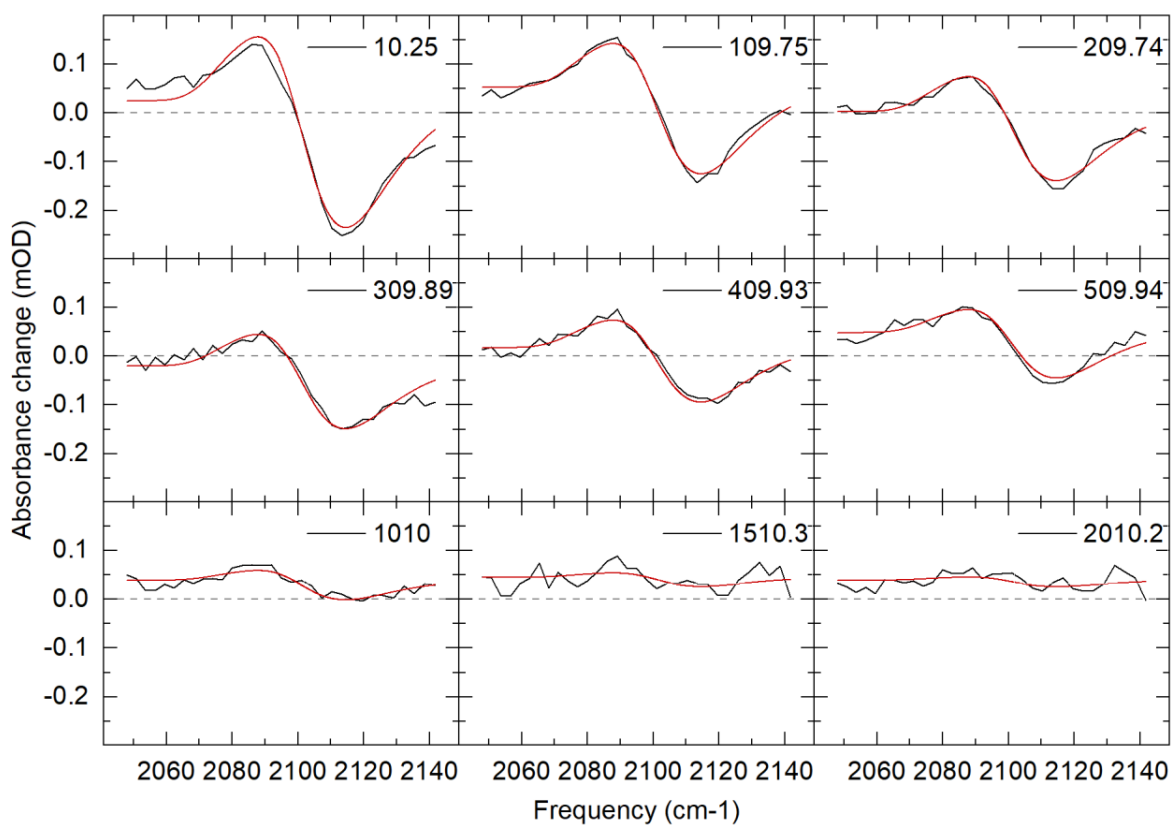

Figure S4: Transient spectra of CaM+P1 for different time steps in fs (black) and global line-fit (red).
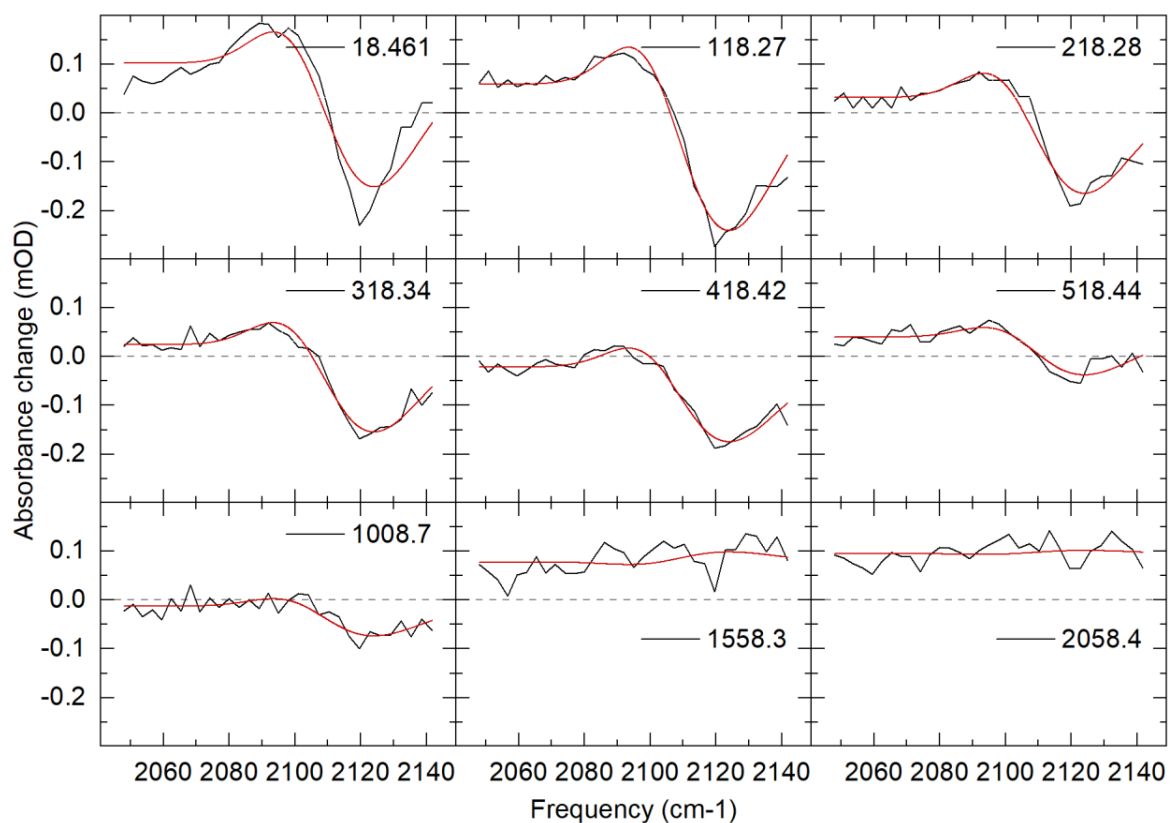
4

Figure S5: Transient spectra of CaM+P2 for different time steps in fs (black) and global line-fit (red).

Figure S6: Transient spectra of CaM+P4 for different time steps in fs (black) and global line-fit (red).
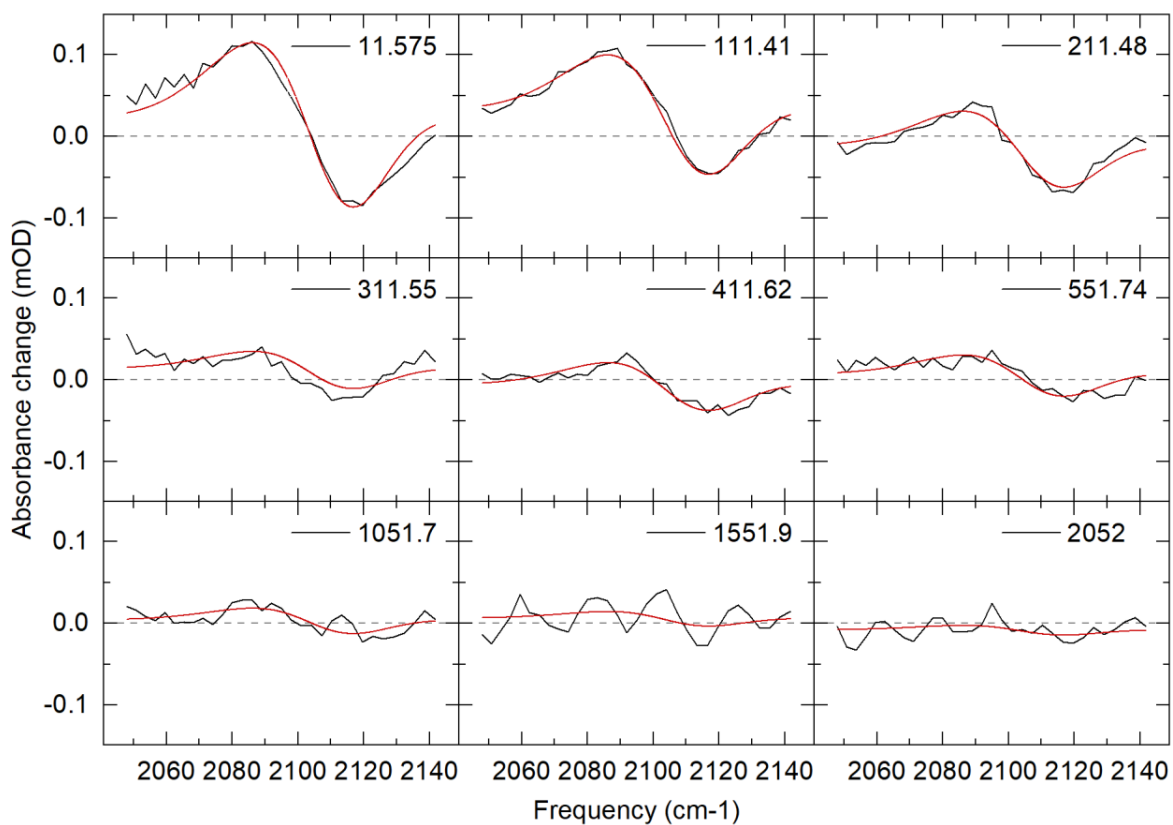
5

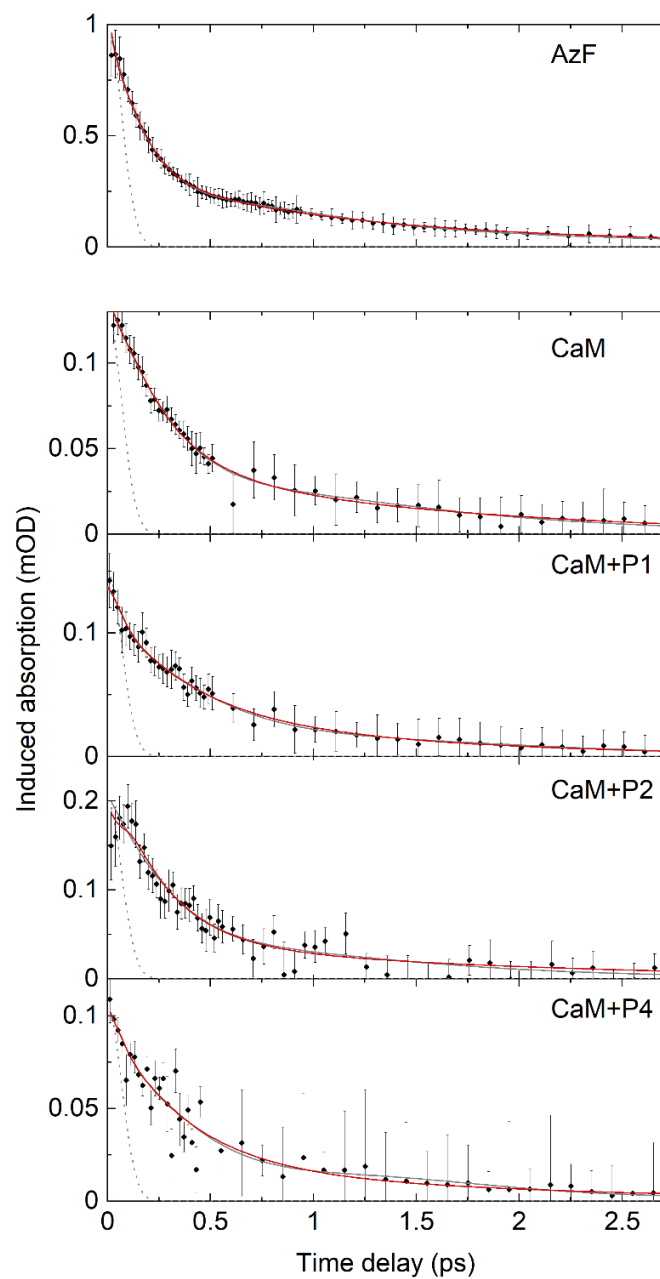**Figure S7:** Bi-exponential fit as alternative approach to model the population dynamics (red). Also shown are the instrument response (dashed grey) and the quantum beat model (solid grey). See figure 4 for comparison. Similar to the quantum beat modulation model, a Gaussian with the width of the instrument response was added to the model to account for non-resonant signal contributions during pulse overlap.

6

Bi exponential modelling of population dynamics

Table S1: Fit results of a biexponential sum to the amplitude of the pump-probe data in figures S1 – S6. A_1, A_2, A_{gauss}, represent the amplitudes of the two exponential functions and the non-resonant Gaussian contribution. τ_1 and τ_2 are the respective time constants.

	A_1	τ_1 / fs	A_2	τ_2 / fs	A_{gauss} /mOD
AzF	0.96	123	0.33	1068	-0.20
	±0.09	±8	±0.01	±36	±0.07
CaM	0.11	240	0.04	1554	-0.01
	±0.01	±30	±0.01	±280	±0.01
CaM+P1	0.09	411	0.03	1825	0.02
	±0.02	±98	±0.02	±913	±0.01
CaM+P2	0.21	248	0.05	2004	-0.05
	±0.02	±60	±0.02	±1080	±0.03
CaM+P4	0.08	380	0.02	2767	0.01
	±0.01	±108	±0.01	±2412	±0.01

Fit of FTIR spectra

All FTIR spectra have been fit using the sum of two Voigt profiles. The built in Voigt profile of OriginPro 2016 was used. According to Origin's documentation, it is implemented as:

$$f(x) = A \frac{2 \ln(2) * w_L}{\pi^{3/2} \cdot w_G^2} * \int_{-\infty}^{\infty} \frac{\exp(-t^2)}{\left(\sqrt{\ln(2)} * \frac{w_L}{w_G}\right)^2 + \left(\sqrt{4 \ln(2)} * \frac{x - x_c}{w_G} - t\right)^2} dt$$

with A is the relative amplitude, w_L the width of the Lorentzian, w_G the width of the Gaussian and x_c the peak position. In Table S3, the additional subscripts indicate peaks 1 and 2 in the superposition model.

7

Table S2: Fit results of FTIR data as described above. All widths correspond to full width at half maximum. w_1 and w_2 are the width of the entire Voigt profile.

|	x_{c1} (cm^{-1})	A_1	w_{G1} (cm^{-1})	w_{L1} (cm^{-1})	w_1 (cm^{-1})	x_{c2} (cm^{-1})	A_2	w_{G2} (cm^{-1})	w_{L2} (cm^{-1})	w_2 (cm^{-1})
AzF	2107.0 ±1.6	10.2 ±1.4	22.9 ±0.9	6.2 ±1.2	27.3 ±1.5	2130.6 ±0.6	29.2 ±1.6	22.9 ±1.4	6.1 ±1.3	27.2 ±1.9
CaM	2110.9 ±0.4	24.8 ±0.9	19.7 ±0.3	5.0 ±0.5	23.2 ±0.6	2129.3 ±1.3	5.0 ±1.1	15.9 ±1.4	5.6 ±3.9	20.0 ±4.1
CaM+P1	2111.2 ±1.1	24.5 ±2.6	17.2 ±0.4	7.9 ±0.6	23.2 ±0.7	2122.9 ±5.1	3.9 ±2.7	23.7 ±9.2	0.0 ±8.8	23.7 ±12.7
CaM+P2	2093.9 ±10.8	5.8 ±2.8	21.7 ±21.3	35.5 ±15.2	54.3 ±26.1	2118.8 ±0.4	27.7 ±2.9	14.9 ±0.6	11.8 ±1.9	24.4 ±2.0
CaM+P4	2109.1 ±0.8	24.4 ±3.5	16.9 ±0.6	11.1 ±0.8	25.6 ±1.0	2122.6 ±2.8	9.3 ±3.6	25.1 ±0.1	0.0 ±0.4	25.1 ±0.4

Linear Spectrum of CaM+P2
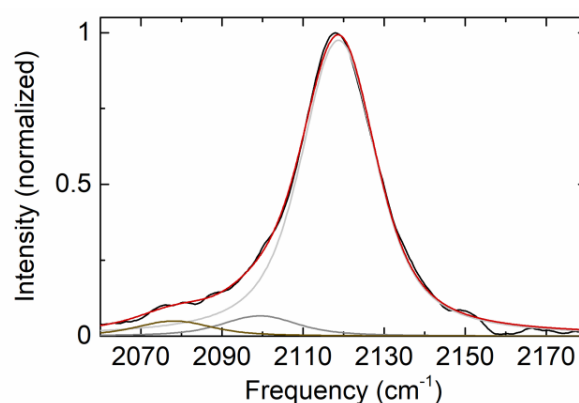
Figure S8: Decomposition of the linear spectrum of the CaM+P2 peptide complex (black) into three Voigt profiles (grey scales) the sum of the profiles is shown in red.

Figure S8 shows an alternative approach to decomposition of the linear spectrum of the CaM+P2 complex using three Voigt profiles, instead of two Voigt profiles, as shown in the article. The widths of the profiles are shared between all peaks as to minimize the number of parameters. The resulting fit parameters are summarized in Table S2. There are two reasons that suggest modeling this linear spectrum with an additional peak: (i) For the two-peak model, a transition at 2093.9 cm^{-1} exhibits a width that is considerably larger than the widths modeled in the other

8

investigated samples (see Table S2). This difference in linewidths may reflect weak coupling but line shapes with several Fermi resonances have been well described by a single line shapes function for all transitions[2], supporting a single line shape model. (ii) The quantum beat frequency and the frequency difference of the modeled transitions in the linear spectrum (while in the uncertainty of our measurement) deviate somewhat while agreement with the other samples is excellent. A three-peak model with a shared line shape describes the linear spectrum just as well while providing an improved match between the quantum beat frequency (16.1 ± 13.3 cm^{-1}) and the frequency difference of peaks 1 and 2 in Table S3 (19.5 ± 7.1 cm^{-1}). Both aspects may indicate that a three-transitions model might be more suitable for the CaM+P2 spectrum. Our accuracy for the quantum beat frequency does not allow for a clear model distinction and we decided to use the same model for the linear spectrum of all samples for better comparability. Generally, the analysis of pump probe transients and linear spectra underscores their duality in regard to Fermi resonances and this duality could be exploited to analyze line shapes and identify the nature of individual transitions in linear spectra (i.e. Fermi resonances vs. superpositions of line shapes from different sub-ensembles).

Table S3: Fit results of the linear FTIR spectrum of CaM+P2. All widths correspond to full width at half maximum. w is the width of the entire Voigt profile.

w_G (cm^{-1})	w_L (cm^{-1})	w (cm^{-1})	A_1	x_{c1} (cm^{-1})	A_2	x_{c2} (cm^{-1})	A_3	x_{c3} (cm^{-1})	$\Delta\nu_{12}$ (cm^{-1})	$\Delta\nu_{13}$ (cm^{-1})
13.5 ±0.6	13.5 ±1.1	24.8 ±1.3	29.3 ±1.6	2118.8 ±0.4	2.0 ±1.2	2099.3 ±6.7	1.5 ±0.2	2078.2 ±2.1	19.5 ±7.1	40.6 ±2.5

9

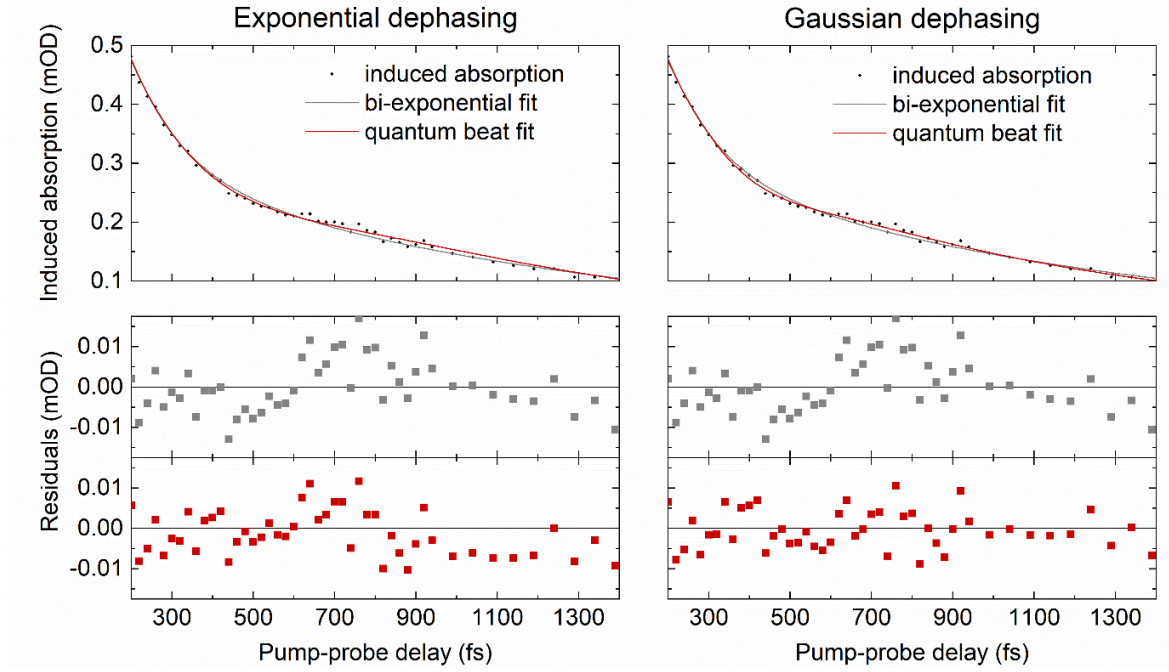**Residual analysis of the quantum beat model**

Figure S9: Bi-exponential and quantum beat fit as shown in figure S7 (top panels) along with residuals (bottom panels). **Left.** Exponentially damped quantum beat. **Right.** Gaussian damping of quantum beat.

Figure S9 shows a comparison between the bi-exponential decay model, and the quantum beat model, as shown in figure S7 (top). The bi-exponential model clearly overestimates the signal at a delay of 400-500 fs, while it underestimates the signal between 600 fs and 900 fs. The employed quantum beat model is a clear improvement, which also reflects in the residuals. Still, the exponentially damped quantum beat overestimates the signal between 900 fs and 1300 fs. Due to the stochastic nature of the dephasing process of the quantum coherence between the transitions in Fermi resonance, we would expect the decay of the beat signal to be predominantly of Gaussian shape because the dephasing time is much shorter than the lifetime of the transitions. Therefore, the decay dynamics of the azido stretching vibration would best be modelled as:

$$S(t) = \mathrm{A_{gauss}} \cdot e^{-4\,ln(2)\left(\frac{t}{FWHM}\right)^2} + \mathrm{A_{osc}} \cdot \cos\left(2\pi\frac{t}{\tau_{osc}}\right) \cdot e^{-\frac{t^2}{2\tau_{coh}^2}} + \mathrm{A_{pop}} \cdot e^{-\frac{t}{\tau_{pop}}}.$$

10

The resulting fit is shown on the righthand side of figure S9, again in comparison to the bi-exponential model. This fit clearly illustrates the overdamped modulation of the signal. Employing the Gaussian dephasing, the residuals are symmetrically spread and the deviations are less than 10 μOD. This suggests, that the dephasing of the quantum beat in AzF might in fact be governed by its inhomogeneous surroundings, unfortunately the required accuracy for such an analysis is unobtainable for the protein samples. The according fit results, which are also fully commensurate with the FTIR peak assignment (Fig4), are displayed in table S4.

Table S4. Fit parameters of the quantum beat model with Gaussian damping. τ_{pop}, τ_{coh} and τ_{osc} are the population time, the coherence time and oscillation period of the damped cosine contribution. $\Delta\nu_{12}$ is the spacing of the two Voigt profiles fit to the linear spectra on the right of Fig. 4. A_{gauss}, A_{osc} and A_{pop} are the amplitudes of the non-resonant Gaussian component, the oscillatory feature and the population decay.

	τ_{pop} (fs)	τ_{coh} (fs)	τ_{osc} (fs)	$1/\tau_{osc}$ (cm^{-1})	$\Delta\nu_{12}$ (cm^{-1})	A_{gauss} (mOD)	A_{osc} (mOD)	A_{pop} (mOD)
AzF	790 ±26	245 ±12	1516 ±74	22.0 ±1.1	23.6 ±3.0	0.34 ±0.05	0.2 ±0.02	0.41 ±0.01

Phase relation between induced absorption (IA) and stimulated emission (SE) in the quantum beat model in aqueous AzF

The phase relation between the induced absorption and stimulated emission features in aqueous AzF was investigated using the quantum beat model with Gaussian dephasing as introduced above. As opposed to using a fixed phase and a variable oscillation period for the fit model, the oscillation period was fixed to 1400 fs, while allowing variation of the phase. This oscillation period was chosen in accordance to the frequency spacing between the Voigt profiles in the linear response of free AzF (Figure 4). The resulting fit curves are shown in Figure S10 and the parameters are shown in table S5. No significant phase shift between these features can be observed within our experimental resolution. The stable phase relation induced absorption and stimulated emission and

11

the good agreement of fit parameters between tables S4 and S5 further supports our approach of

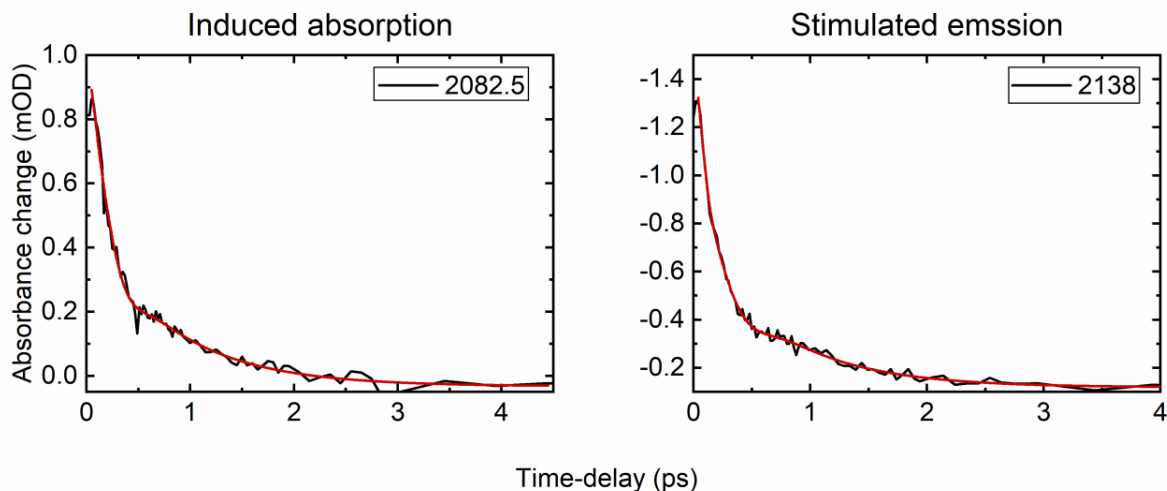extracting the dynamics from the amplitude of a line shape fit.

Figure S10: Time traces for induced absorption (at 2082.5 cm^{-1}) and stimulated emission (at 2138 cm^{-1}) in free aqueous AzF (black). Also shown are fits (red) using the quantum beat model with Gaussian dephasing as introduced above.

Table S5. Fit parameters of the quantum beat model with Gaussian dephasing introduced above. τ_{pop} and τ_{coh} are the population and coherence time damped cosine contribution. ϕ is the relative phase difference to a pure cosine oscillation. A_{gauss}, A_{osc} and A_{pop} are the amplitudes of the non-resonant Gaussian component, the oscillatory feature and the population decay. The oscillation period was fixed to 1400 fs.

	τ_{pop} (fs)	τ_{coh} (fs)	ϕ (°)	A_{gauss} (mOD)	A_{osc} (mOD)	A_{pop} (mOD)
IA	803 ±140	247 ±40	1 ±15	0.14 ±0.06	0.36 ±0.09	0.51 ±0.08
SE/GSB	724 ±99	322 ±50	5 ±16	-0.42 ±0.05	-0.27 ±0.09	-0.62 ±0.10

References

1. A. L. Stancik, and E. B. A Brauns, Simple asymmetric lineshape for fitting infrared absorption spectra, *Vib. Spectrosc.* **47**, 66–69 (2008).

2. T. Elsaesser, N. Huse, J. Dreyer, J. R. Dwyer, K. Heyne, E. T.J. Nibbering, Ultrafast vibrational dynamics and anharmonic couplings of hydrogen-bonded dimers in solution, *Chem. Phys.* **341**, 175–188 (2007)

12

7.3 Eidestattliche Versicherung

Hiermit versichere ich an Eides statt, die vorliegende Dissertationsschrift selbst verfasst und keine anderen als die angegebenen Hilfsmittel und Quellen benutzt zu haben.

Die eingereichte schriftliche Fassung entspricht der auf dem elektronischen Speichermedium.

Die Dissertation wurde in der vorgelegten oder einer ähnlichen Form nicht schon einmal in einem früheren Promotionsverfahren angenommen oder als ungenügend beurteilt.

Hamburg, den 12.4.2022